



3D modelling of movements in electric machines using edge finite elements

Anirudh Chauhan

► To cite this version:

Anirudh Chauhan. 3D modelling of movements in electric machines using edge finite elements. Electric power. Université Grenoble Alpes [2020-..], 2021. English. NNT : 2021GRALT033 . tel-03346179

HAL Id: tel-03346179

<https://theses.hal.science/tel-03346179>

Submitted on 16 Sep 2021

HAL is a multi-disciplinary open access archive for the deposit and dissemination of scientific research documents, whether they are published or not. The documents may come from teaching and research institutions in France or abroad, or from public or private research centers.

L'archive ouverte pluridisciplinaire **HAL**, est destinée au dépôt et à la diffusion de documents scientifiques de niveau recherche, publiés ou non, émanant des établissements d'enseignement et de recherche français ou étrangers, des laboratoires publics ou privés.

THÈSE

Pour obtenir le grade de

DOCTEUR DE L'UNIVERSITE GRENOBLE ALPES

Spécialité : **Génie Electrique**

Arrêté ministériel : 25 mai 2016

Présentée par

Anirudh CHAUHAN

Thèse dirigée par **Yves MARECHAL** et
co-encadrée par **Brahim RAMDANE** et **Pauline FERROUILLAT**

préparée au sein du **Laboratoire de Génie Electrique de
Grenoble (G2Elab)**
dans l'**École Doctorale Electronique, Electrotechnique,
Automatique & Traitement du signal (EEATS)**

3D modeling of movements in electrical machines using edge finite elements

Thèse soutenue publiquement le **10 Mai 2021**,
devant le jury composé de :

M. Zhuoxiang REN

Professeur à Sorbonne Université (Président)

Mme. Francesca RAPETTI

Maître de conférence HDR à l'Université Cote d'Azur (Rapporteur)

M. Yvonnick LE MENACH

Professeur à l'Université de Lille (Rapporteur)

M. Gérard MEUNIER

Directeur de recherche CNRS à Grenoble (Membre)

M. Yves MARECHAL

Professeur à l'Université Grenoble Alpes (Directeur de thèse)

M. Brahim RAMDANE

Maître de conférence à l'Université Grenoble Alpes (Co-encadrant de thèse)

Mme. Pauline FERROUILLAT

Docteur-Ingénieur à Altair (Co-encadrant de thèse)



To my Parents & Didi

Acknowledgements

Firstly, I would like to express my sincere gratitude to my supervisors **Prof. Yves Marechal**, **M. Gerard Meunier** (Directeur de recherche CNRS), **Prof. Brahim Ramdane** (Maître de Conférence) for the continuous support of my PhD study and related research, for their patience, motivation, and immense knowledge. Their guidance helped me throughout the time of my thesis.

I would like to thank **Mme. Pauline Ferrouillat** (R&D engineer - Altair) for the continuous support of my PhD study and also for helping me to get familiarize with Altair developing environment during the initial time of my thesis.

Besides my supervisors, I also like to thank **M. Christophe Guerin** (Senior R&D engineer - Altair) for his support during the crucial part of my PhD study and interesting discussions related to my research.

I also like to thank **M. Farid Zidat** (Senior Application engineer - Altair) for helping me with setting commercial test cases for my PhD study. I am also grateful to **M. Guy Jerome** (R&D director - Altair FluxTM) for keeping me motivated during the writing of this thesis.

I thank my colleagues from G2Elab and Altair, with whom I spent a huge amount of time during office hours and beyond. Thanks to all of you for the moments we shared.

I wish to thank the unconditional support of my parents, my grandmother and my sister despite the long distance. Without their support, it would not have been possible to pursue a doctorate in France.

Finally, I would like to gratefully acknowledge the support provided for this work under the framework of CIFRE, financed by the Altair and the French Government.

Contents

Acknowledgements	V
Résumé étendu en française	X
Introduction	1
 I Modeling of low frequency Maxwell equations	 4
1 Problem Description	6
1.1 Maxwell's equations and interface conditions	7
1.1.1 Differential form of Maxwell's equations	7
1.1.2 Constitutive Relations	8
1.1.3 Boundary and Interface Conditions	8
1.2 Magneto-static and magneto-transient problem	9
1.2.1 Magneto-Static problem	9
1.2.2 Magneto-transient Problem	10
1.3 Source computation using magnetic vector potential formulation \mathbf{A}_j .	12
1.4 Summary	13
 2 Numerical Modeling of low frequency Maxwell equations using edge finite element method	 14
2.1 Functional Spaces	15
2.1.1 Lebesgue Spaces	15
2.1.2 Sobolev Spaces	15
2.1.3 Functional spaces for differential operators	15
2.1.4 Tonti Diagram	16
2.2 Finite Element Method	17
2.2.1 Approximation spaces	17
2.2.2 Mapped finite element (Reference element and real element) .	18
2.2.3 Shape functions	18
2.3 Application of finite element for approximating magneto static problem	20
2.3.1 Weak form of magneto-static problem	20
2.3.2 Discretized modeling using finite element method	21
2.4 Application of finite element for approximating magneto-transient problem	21
2.4.1 Weak form of magneto-transient problem	22
2.4.2 Discretized modeling using finite element method	22

2.5	Application of finite element for source computation using magnetic vector potential formulation \mathbf{A}_j under reduced domain	24
2.5.1	Weak form	24
2.5.2	Discretized modeling using finite element method	24
2.6	Summary	25
II Taking movement into account for magnetic vector potential formulation		26
3	State of the art for taking movement into account	28
3.1	Taking movement into account in different frame of reference	29
3.1.1	Eulerian approach	29
3.1.2	Lagrangian approach	30
3.2	Methods based on volume air-gap principle	31
3.2.1	Remeshing	32
3.2.2	Macro element	33
3.2.3	Boundary element method	34
3.2.4	Overlapping finite element	34
3.3	Method based on sliding surface principle	35
3.3.1	Lock step method	36
3.3.2	Lagrange multiplier	37
3.3.3	Mortar method	38
3.3.4	Interpolation	39
3.3.5	Mixed finite element method / Natural element method	40
3.4	Conclusion	40
4	Mortar method	42
4.1	Theory of mortar method	43
4.1.1	Coupling matrices	43
4.1.2	Matrix structure after including coupling matrices	45
4.2	Implementation of mortar method	46
4.2.1	Integrating domain	46
4.2.2	Computation of coupling matrices	47
4.2.3	Inversion of coupling matrix \mathbf{C}	49
4.3	Conclusion	50
5	Interpolation Method	52
5.1	Introduction to interpolation method	53
5.2	Nodal interpolation method	54
5.2.1	Principle	54
5.2.2	Computation of the interpolation coefficient	56
5.3	Edge interpolation method	57
5.3.1	Extending the idea to first order incomplete edge finite element framework	57
5.3.2	Computation of the interpolation coefficient	58
5.4	Performing Linear combination	59
5.5	Conclusion	61

III	Validation and Results	64
6	Magneto-static 3D academic test case	66
6.1	Description of magneto-static 3D academic test case	67
6.1.1	Mesh Scenarios	67
6.1.2	Error Computation	68
6.1.3	Intermediate mortar mesh	68
6.2	Validation and results	69
6.2.1	Isovalues of magnetic flux density	69
6.2.2	Convergence Analysis (Accuracy)	70
6.2.3	Performance	71
6.3	Robustness analysis based on mesh regularity	72
6.4	Validation and results of source terms computed on reduced domain under the application of movement (Non - Meshed coils)	73
6.4.1	Isovalues of magnetic flux density	73
6.4.2	Magnetic Energy	74
6.4.3	Magnetic Flux	75
6.5	Conclusions	75
7	TEAM workshop problem 24	76
7.1	Magneto-static problem	77
7.1.1	Test case description	77
7.1.2	Linear problem	77
7.1.3	Non-linear problem	81
7.1.4	Summary	84
7.2	Source term computed on reduced domain for non-meshed coils under magneto-static and magneto transient scenario	84
7.2.1	Magneto-static problem	84
7.2.2	Magneto transient problem	86
7.2.3	Summary	86
7.3	Conclusion	86
8	Transient FEA of Induction Machine using Edge Interpolation	88
8.1	Description of induction machine	89
8.2	Results	90
8.2.1	Isovalues of magnetic flux density	90
8.2.2	Torque and Magnetic flux	90
8.2.3	Eddy current Losses	92
8.2.4	Computational performance	92
8.3	Conclusion	93
	General Conclusion	94
	Bibliography	96
A	Definitions	101
A.1	Inner product form	101
A.2	Norm of $\mathbf{L}^2(\Omega)$ and $\mathbf{H}(\text{curl}, \Omega)$	101
A.3	\mathbf{H}_j be the $\mathbf{L}^2(\Omega)$ projection of \mathbf{H}_s	101

A.4	\mathbf{A}_j be the $\mathbf{H}(\mathbf{curl}, \Omega)$ projection of \mathbf{H}_s	101
B	A-ϕ nodal interpolation	102
B.1	A- ϕ formulation	102
B.2	Results	102
B.2.1	Sensor	102
B.2.2	TEAM workshop problem 24 (Non linear problem)	104

Résumé étendu en française

Ce chapitre est une résumé étendu de la thèse, en français. Le lecteur intéressé pas plus de détails pourra commencer directement la lecture au chapitre suivante.

Introduction

Ces dernières années, la méthode des éléments finis d'arête est devenue très populaire dans la modélisation de la machine électrique rotative tridimensionnelle en raison de sa capacité à représenter correctement le comportement physique du champ le long de l'interface. Cependant, la modélisation devient complexe lorsqu'une distorsion importante du maillage se produit le long d'une surface de glissement en raison d'un mouvement. Une étape de remaillage est nécessaire, ce qui augmente le coût de calcul. Afin d'éviter le remaillage, des méthodes numériques efficaces ont déjà été développées pour modéliser le mouvement dans la machine électrique tournante tridimensionnelle par la méthode des éléments finis d'arête. Néanmoins, très peu de recherches ont été menées pour comparer ces méthodes. L'objectif principal de cette thèse est de comparer l'interpolation basée sur d'arête et la méthode des éléments avec joints. Pour améliorer la précision de l'interpolation basée sur les arêtes pour le maillage tétraédrique, nous proposons une stratégie améliorée. Les résultats numériques illustrent la précision, la robustesse et la performance des méthodes. Une comparaison détaillée est présentée sur la base des critères mentionnés ci-dessus.

Modélisation numérique de machine électrique tournante

Pour simuler correctement la machine électrique tournante, il faut prendre en compte le mouvement de rotation. Typiquement une machine électrique tournante est divisée en deux domaines : le stator (partie fixe) et le rotor (partie mobile) séparés par un entrefer. L'entrefer prend également en compte le transfert de flux entre deux domaines et aussi la majeure partie de l'énergie concentrée autour de l'entrefer. Ainsi assurer la continuité de la composante tangentielle du champ magnétique (H) et de la composante normale de la densité de flux magnétique (B) le long de l'entrefer est essentiel.

Actuellement, la méthode des éléments finis est largement adoptée pour résoudre numériquement l'équation de Maxwell. Cependant, tout en tenant compte de la rotation, cela conduit à un scénario de maillage non conforme à l'interface, c'est-à-dire un problème de nœuds suspendus voir fig.(1). Maintenant, pour surmonter ce défi, on peut appliquer un remaillage, ce qui est assez coûteux en calcul. Ainsi par

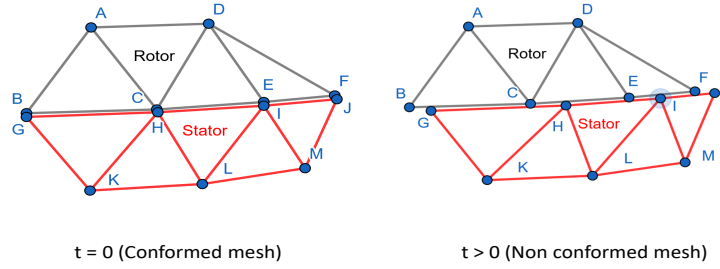


Figure 1 – Le scénario initial de maillage conforme devient non conforme lorsque la partie rotor commence à bouger.

le passé, plusieurs approches ont déjà été proposées pour éviter le remaillage. Les approches sont généralement classées sous deux principes populaires. Le premier principe est l'entrefer de volume et les méthodes qui en découlent sont le macro élément [1], la bande mobile [19] et la technique d'overlapping [30, 31, 32, 62]. Le deuxième principe est la surface de glissement et les méthodes définies en vertu de celle-ci sont l'approche pas à pas cite Preston, le multiplicateur de Lagrange [34], la technique d'interpolation nodale [46] parmi beaucoup d'autres. L'objectif de cette thèse est d'analyser et de comparer des méthodes basées sur le principe de la surface de glissement. Les critères de comparaison seront la précision, les performances et la robustesse dans une région impliquant une grande déformation du maillage.

Méthode basée sur le principe de la surface de glissement sous cadre d'éléments finis d'arête

Sous la méthode du principe de la surface de glissement basée sur l'approche de pénalisation (Méthode des éléments avec joints) [14, 51, 56] a montré qu'un mouvement pouvait être modélisé avec une bonne précision.

Cependant, les opérations d'intersection et le calcul des matrices de couplage sous la méthode des éléments avec joints impliquent une inversion complète de la matrice, des inconnues supplémentaires et la génération d'un nouveau maillage de intégration.

Dans le passé, les chercheurs ont produit de nombreuses approches prometteuses sous interpolation d'arête. Cependant, les méthodes étaient limitées au scénario de maillage régulier [26, 29] et à l'utilisation d'un maillage temporaire pour appliquer la continuité de flux [43]. Le moyen le plus simple d'appliquer une interpolation est basé sur la technique maître-esclave, comme le montre [46] dans un cadre d'éléments finis nodal. [45] a proposé une technique d'interpolation similaire sous cadre d'éléments finis d'arête mais limitée au type de maillage hexaédrique. Récemment [66] a proposé une forme simplifiée de [45] pour le type de maillage tétraédrique (scénario de maillage généralisé) mais montre une faible précision à maillage grossier. Nous appelons cette méthode le type discontinu dans notre thèse. Dans cette thèse, nous proposons une extension de [45] pour le type de maillage tétraédrique pour surmonter le problème de précision montré dans [66] et la méthode est appelée type continu.

Chacune des méthodes mentionnées ci-dessus présente des avantages et des inconvénients, mais très peu de recherches ont été menées pour comparer ces méthodes. Par conséquent, nous proposons une comparaison de deux techniques pour un scé-

nario magnétostatique 3D. La première est la méthode des éléments avec joints [14], et la seconde technique est l'interpolation d'arête [45].

Formules

Pour le cas magnétostatique, les équations de Maxwell et la loi de comportement sont données par :

$$\mathbf{rot} \mathbf{H} = \mathbf{J}_{source} \text{ with } \mathbf{H} \times \mathbf{n} = 0 \text{ on } \Gamma_H, \quad (1)$$

$$\mathbf{div} \mathbf{B} = 0 \text{ with } \mathbf{B} \cdot \mathbf{n} = 0 \text{ on } \Gamma_B. \quad (2)$$

\mathbf{J}_{source} , \mathbf{H} and \mathbf{B} sont respectivement la densité de courant de la source, le champ magnétique et la densité de flux magnétique. La condition à l'interface glissante est donnée comme,

$$(\mathbf{H}_M - \mathbf{H}_F) \times \mathbf{n} = 0 \text{ and } (\mathbf{B}_M - \mathbf{B}_F) \cdot \mathbf{n} = 0. \quad (3)$$

ici \mathbf{n} est l'extérieur normal de Γ . $(\mathbf{H}_M, \mathbf{H}_F)$ et $(\mathbf{B}_M, \mathbf{B}_F)$ sont les \mathbf{H} et \mathbf{B} respectivement à l'interface entre la partie mobile (M) et la partie fixe (F). En utilisant (2), \mathbf{B} peut être approximé comme:

$$\mathbf{B} = \mathbf{curl} \mathbf{A} \text{ with } \mathbf{A} \times \mathbf{n} = 0 \text{ on } \Gamma_B, \quad (4)$$

$$\mathbf{B} = \mu \mathbf{H} \text{ here } \mu = \text{magnetic permeability}. \quad (5)$$

Dans (4) en remplaçant \mathbf{B} par \mathbf{H} en utilisant (5) et en remplaçant dans (1)

$$\mathbf{curl}(\mu^{-1} \mathbf{curl} \mathbf{A}) = \mathbf{J}_{source}. \quad (6)$$

Méthodes

Méthode des éléments avec joints

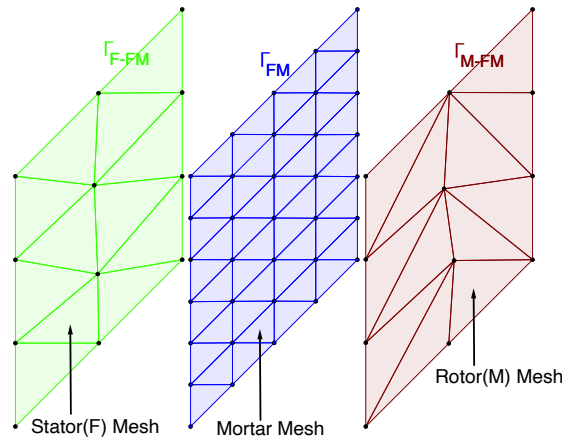


Figure 2 – Représentation de l'interface integration Γ_{FM} formée en intégrant des interfaces Γ_{F-FM} fixes et mobiles Γ_{M-FM} .

Dans la méthode des éléments avec joints [14], [51] la continuité tangentielle de \mathbf{A} est assurée au sens faible en introduisant un multiplicateur de Lagrange \mathbf{A}' , tel que

$$\int_{\Gamma_{FM}} \mathbf{A}' \cdot (\mathbf{n} \times \mathbf{A}^F|_{\Gamma_{F-FM}} - \mathbf{n} \times \mathbf{A}^M|_{\Gamma_{M-FM}}) d\Gamma = 0, \quad (7)$$

ici Γ_{F-FM} et Γ_{M-FM} représentent respectivement l'interface de glissement le long de la partie fixe F et de la partie mobile M. L'union de deux interfaces donne l'interface de intégration Γ_{FM} définie comme :

$$\Gamma_{FM} = \Gamma_{F-FM} + \Gamma_{M-FM}, \quad (8)$$

sur lequel un maillage de intégration est construit. Le maillage de intégration construit est plus fin que le maillage d'interface de la partie mobile et fixe comme le montre la fig.(2) se référer à [14] pour plus de détails. Soit $n_{\Gamma_{F-FM}}$ et $n_{\Gamma_{M-FM}}$ le nombre d'arêtes sur les mailles d'interface de Γ_{F-FM} et Γ_{M-FM} respectivement. En décomposant \mathbf{A} sur des éléments finis d'arête, nous pouvons écrire (7) comme :

$$\sum_{j=1}^{n_{\Gamma_{F-FM}}} A_j^F \int_{\Gamma_{FM}} \mathbf{A}' \cdot (\mathbf{n} \times \mathbf{N}_j^F) d\Gamma = \sum_{i=1}^{n_{\Gamma_{M-FM}}} A_i^M \int_{\Gamma_{FM}} \mathbf{A}' \cdot (\mathbf{n} \times \mathbf{N}_i^M) d\Gamma, \quad (9)$$

(9) peut aussi s'exprimer sous forme de système matriciel, ici C et D sont les matrices de couplage, l'opération $C^{-1}D$ conduit à un système matriciel dense le long de l'interface.

$$C A_{\Gamma_{F-FM}}^F = D A_{\Gamma_{M-FM}}^M \implies A_{\Gamma_{F-FM}}^F = C^{-1} D A_{\Gamma_{M-FM}}^M. \quad (10)$$

L'interpolation basée sur les arêtes

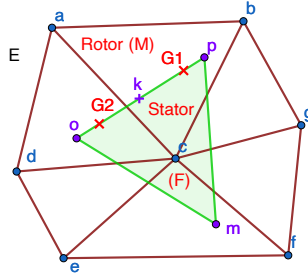


Figure 3 – Représentation de l'élément triangulaire maître-esclave non conformée en interface de glissement.

Une approche généralisée est proposée sous le nom de "type continu", qui peut être appliquée aux maillages tétraédriques conformes. L'approche est une extension de [45], initialement proposée pour les maillages hexaédriques. Par exemple, pour l'arête "e_{op}" voir fig.(3), On obtient :

$$A_{e_{op}}^F = \sum_{e_{ij}=e_{cb}, e_{ba}, e_{ac}, e_{cd}, e_{da}} A_{e_{ij}}^M C_{e_{ij}}, \quad (11)$$

Ici $A_{e_{op}}^F$ est une inconnue basée sur le arête sur le arête pointant du nœud "o" au nœud "p" du fixe partie (F), de même pour $A_{e_{ij}}^M$ sur la partie mobile (M). Le coefficient d'interpolation $C_{e_{ij}}$ peut être interprété comme :

$$C_{e_{ij}} = \int_{l_{e_{op}}} \mathbf{N}_{e_{ij}}^M(\epsilon, \eta) \cdot d\mathbf{l}, \quad (12)$$

$$= \frac{l_{e_{op}}}{2} \int_{-1}^1 \mathbf{N}_{e_{ij}}^M(\lambda) \cdot \mathbf{e}_{op} d\lambda. \quad (13)$$

où ϵ, η représente le système de coordonnées locales 2-D et λ représente e_{op} sur le système de coordonnées 1-D sur lequel $C_{e_{ij}}$ est calculé en utilisant la méthode de quadrature Gaussienne à deux points aux points de Gauss "G1" et "G2" voir fig.(3). $\mathbf{N}_{e_{ij}}^M$ est une fonction de base des arêtes calculée pour les arêtes de la partie mobile (M) sur les points de Gauss, $l_{e_{op}}$ est la longueur d'une arête e_{op} .

Si $C_{e_{ij}}$ est calculé au point "k" d'une arête e_{op} voir fig.(3) en utilisant méthode de quadrature de Gauss à un point. L'approche devient similaire à [66].

Validation et résultats

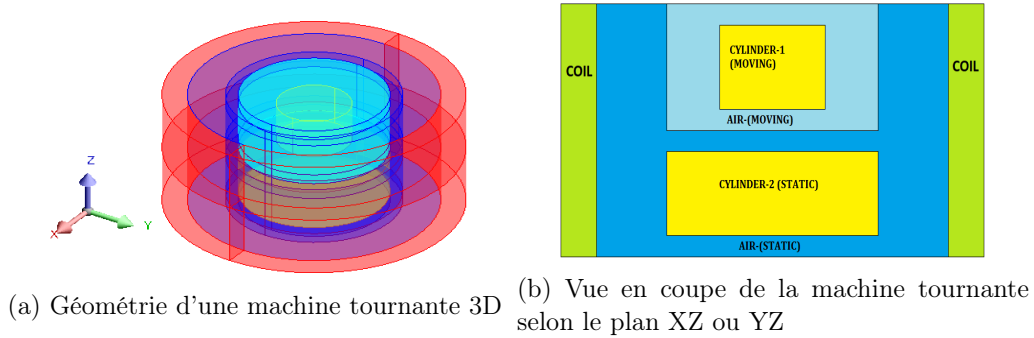


Figure 4 – Représentation détaillée d'une machine tournante 3D

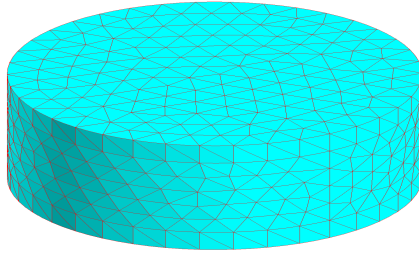
Description du cas de test académique 3D magnétostatique

Nous considérons un cas de test académique symétrique autour de l'axe Z. Comme le montre la fig.(4), le cas de test est construit à l'aide de deux cylindres entourés d'un conducteur de bobine cylindrique. Le cylindre mobile est construit au sommet d'un cylindre statique séparé par un mince entrefer d'épaisseur 1 unité. Le diamètre du cylindre mobile est de 3 unités et celui du cylindre statique est de 6 unités. L'épaisseur du conducteur de la bobine est de 1 unité. La différence de rayon entre le conducteur de la bobine et le cylindre statique est de 2 unités et 3,5 unités avec le cylindre mobile. La hauteur totale du conducteur de la bobine est de 6 unités. Le cas de test est conçu de manière à ce que la valeur de champ calculée reste constante à chaque étape.

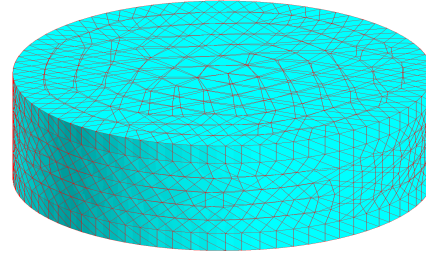
La propriété physique des deux cylindres est isotrope linéaire avec une perméabilité magnétique relative (μ_r) de 2000. Le nombre de tours dans l'enroulement de

la bobine appliqué au conducteur de la bobine est de 350. Le courant de source appliqué dans la bobine est 5 A.

Mesh Scenarios



(a) Maille conformée à $\theta = 0^\circ$



(b) Maille non conformée à $\theta = 5^\circ$

Figure 5 – Vue 3D du maillage conforme et non conforme autour de l'interface de glissement

Table 1 – Sélection de scénarios de maillage.

Scénario de maillage	Degrés de liberté	Maille autour de la surface de glissement
		(Environ. longueur d'une arête)
1	87.000	0,6 mm
2	129.000	0,5 mm
3	204.757	0,4 mm
4	591.710	0,2 mm

Le maillage de surface autour de la surface de glissement sous le maillage conforme et le maillage non conforme sont représentés respectivement sur la fig.(5a) et la fig.(5b). Dans ce partie, nous allons tester la méthode des éléments avec joints et l'interpolation d'arêtes sur quatre scénarios différents de maillage uniforme, comme détaillé dans le tableau.1. La taille d'une arête appartenant à l'élément triangulaire autour de la surface de glissement diminue du scénario de maillage 1 au scénario de maillage 4, comme indiqué dans la troisième colonne du tableau.1.

Isolines de densité de flux magnétique

Afin de valider les approches décrites ici, nous l'avons testé sur le cas de test magnéto-statique voir fig.(4). La fig.(6) montre des flèches de flux magnétique continu se déplaçant du cylindre 1 (en mouvement) au cylindre 2 (statique) à travers l'entrefer. Aucune différence visible ne peut être vue entre le maillage conforme et le maillage non conforme utilisant l'interpolation d'arêtes et la méthode des éléments avec joints voir fig.(6).

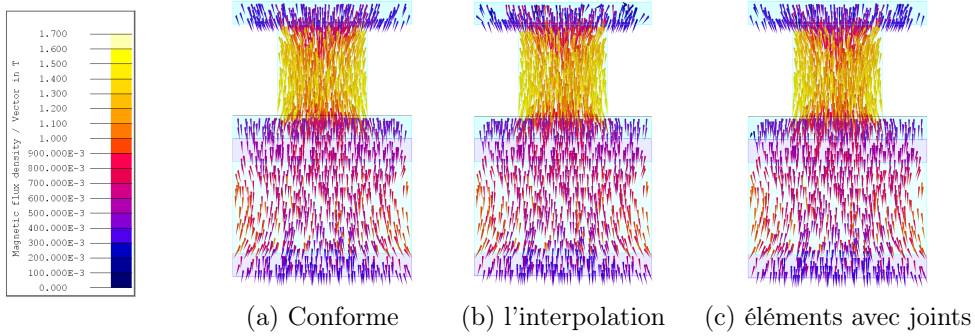


Figure 6 – Représentation des flèches de flux du cylindre-1 (en mouvement) au cylindre-2 (statique) à $\theta = 5^\circ$

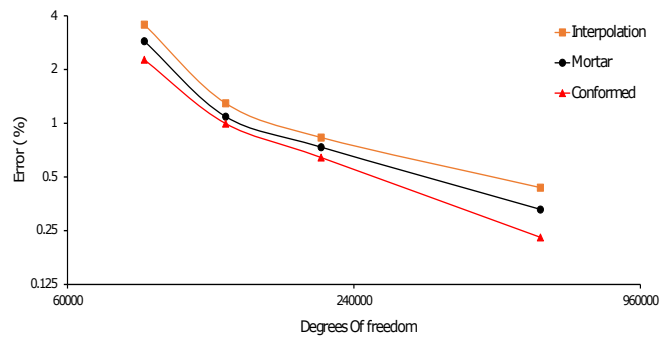


Figure 7 – Analyse de convergence pour l'énergie magnétique.

Analyse de convergence (précision)

Le cas de référence pour l'analyse de convergence est le calcul de l'énergie magnétique sous le maillage conforme pour environ 1,5 million d'inconnues. L'évolution de l'erreur dans le calcul de l'énergie magnétique est représentée sur l'échelle log-log de la fig.(7). La pente de celui-ci représente le taux de convergence. Le même taux de convergence pour la méthode des éléments avec joints et l'interpolation d'arêtes est observé. Cependant, la précision de la méthode des éléments avec joints et l'interpolation d'arêtes.

Performance

Table 2 – Temps de calcul par étape.

Scénario	Maille conformée	Interpolation d'arêtes	éléments avec joints
1	19 s	19 s	41 s
2	23 s	23 s	57 s
3	40 s	44 s	127 s
4	126 s	141 s	2.862 s

Table 3 – Nombre de termes non nuls dans la matrice.

Scénario	Maille conformée	Interpolation d'arêtes	éléments avec joints
1	1.713.786	1.745.178	5.280.970
2	2.011.643	2.049.480	6.437.257
3	2.956.097	3.008.769	9.361.955
4	8.357.734	8.582.596	39.003.229

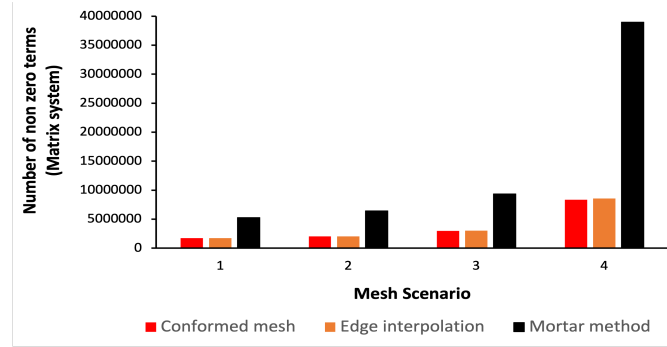


Figure 8 – Nombre de termes non nuls dans un système matriciel à différents scénarios de maillage.

En analysant le tableau.2, il est montré à partir de la simulation que l'interpolation d'arêtes est deux fois plus rapide que la méthode des éléments avec joints dans le scénario-1 et cet écart augmente, car la différence de temps de calcul augmente presque de vingt fois dans le cas du scénario-4. Une autre chose importante qui doit être remarquée dans le tableau.3 et fig.(8) que le nombre de termes non nuls dans le cas de la méthode des éléments avec joints augmente de façon exponentielle contrairement à l'interpolation d'arêtes tout en passer du scénario 1 au scénario 4. La raison de l'augmentation du nombre de termes non nuls est la taille du maillage de intégration. Cette augmentation exponentielle du nombre de termes non nuls dans le cas de la méthode des éléments avec joints conduit également à l'utilisation d'une grande quantité de mémoire de calcul.

Conclusion

Dans cette thèse, nous avons comparé deux approches pour modéliser une machine électrique tournante et les avons comparées en fonction de la précision et des performances. De l'analyse présentée dans les sections précision et performance, les conclusions suivantes peuvent être tirées : -

- Les deux méthodes donnent des résultats précis pour le calcul de l'énergie dans un scénario de maillage fin.
- La précision de la méthode des éléments avec joints s'est avérée un peu plus précise que l'interpolation d'arêtes.
- La méthode des éléments avec joints est plus coûteuse que l'interpolation d'arêtes en termes de temps de calcul et de mémoire de calcul.

Si l'on prend en compte tous les facteurs de simulation, c'est-à-dire la précision et les performances, l'interpolation d'arêtes s'avère plus efficace que la méthode des éléments avec joints.

Introduction

Due to an exponential increase in carbon emissions, a deterioration in air quality, abrupt changes in weather cycle, and global warming are observed recently. These abrupt changes and deterioration of the environment have pushed the society globally to seek alternative low emission (sustainable) transportation system that is energy efficient.

According to [18]-[8], the transportation industry plays a significant contribution to increasing carbon emission in the environment. Therefore, in curtailing the greenhouse gases, the automotive industry is switching to electric vehicles (EV_s) from internal combustion engine-based vehicles (ICE). Today traction motors (electric motors) are widely used as propulsion of a vehicle. To meet new challenges like emission standards and improve traction motors' economy has pushed the automotive industry to develop more-complex and energy-efficient traction motors.

A traction motor is a rotating electrical machine composed of a stator (fixed part), a rotor (moving part) and separated by a thin air-gap. It is an electromechanical converter that converts electrical energy into mechanical energy widely used for a propulsion of a locomotive and electric vehicles.

In recent times, we have seen computer-aided engineering (CAE) tools, based on the finite element method, play an essential role in better understanding the design, improving performance, and reducing design time of traction motors. Today, CAE tools can perform 3D simulation of the examples like axial machines, permanent magnet synchronous machines, induction motors etc. These simulations must consider the circuit coupling, the movement of the rotor and the evaluation of the eddy current losses in the machine.

A finite elements-based solver has been developed to model low-frequency electromagnetic phenomena on a commercial software Altair FluxTM. In the Altair FluxTM software, formulations based on the magnetic scalar potential have been developed with the nodal finite element method and have been used successfully for many years for the modeling of 3D devices [37]. They make it possible to use a single unknown in the air and set up coupling with the electric circuit equations. Besides, the use of nodal finite elements makes it possible to simplify the implementation of the finite element solution between the stator and the rotor of an electrical machine. A significant disadvantage of this method is the need to manage the multiply connectivity problems induced by the magnetic scalar potential. One solution is to introduce artificial cuts in the mesh, which is difficult to implement by the user [48].

In order to avoid introducing artificial cuts in the studied domain, magnetic vector potential formulations are used [7]. This thesis's technical and scientific challenges will be to develop and compare the methods to take movement into account in the rotating electrical machines by using magnetic vector potential formulation with 3D edge finite element.

The thesis is divided into three parts. The first part gives a brief introduction on 3D modeling of low-frequency Maxwell's equations for magnetostatic and magneto transient problem based on \mathbf{A} and \mathbf{A} -V formulations. The technique for source computation, while taking the movement into account in the case of non-meshed coils. A brief recall of functional spaces and finite element method on which the unknowns are approximated.

In the second part, we discuss how we take movement into account. Based on that, a brief review of the methods is provided and classified into two families. Based on literature review and development constraints, two methods are chosen to be developed. The mortar method and edge interpolation are chosen and explained in detail. In the case of edge interpolation, a piece-wise continuous integration approach is proposed to calculate the interpolation coefficient. The new approach helps in the reduction of numerical oscillations during torque and magnetic flux calculations.

In the third part, we analyse the mortar method and the edge interpolation based on performance and accuracy. Firstly, we tested these methods on an academic test cases in terms of magnetic flux, magnetic torque and magnetic flux density. Based on the results, we proposed the convergence rate and computation time of these methods. Finally, we tested edge interpolation in transient FEA of an induction motor and presented the detailed comparison with the magnetic scalar potential formulation of the commercial version. The mortar method and edge interpolation are implemented in a development version of Altair FluxTM.

Part I

Modeling of low frequency Maxwell equations

Chapter 1

Problem Description

Contents

1.1	Maxwell's equations and interface conditions	7
1.1.1	Differential form of Maxwell's equations	7
1.1.2	Constitutive Relations	8
1.1.3	Boundary and Interface Conditions	8
1.2	Magneto-static and magneto-transient problem	9
1.2.1	Magneto-Static problem	9
1.2.2	Magneto-transient Problem	10
1.3	Source computation using magnetic vector potential formulation A_j	12
1.4	Summary	13

The numerical modeling or analysis of electrical machines requires electromagnetic field calculation to derive torque, force, etc.

To derive these quantities, one needs to solve the differential form of Maxwell's equations with proper boundary conditions that mathematically represent the particular electrical machine. Maxwell's equations are the collection of partial differential equations of the magnetic field \mathbf{H} , electric field \mathbf{E} , magnetic flux density \mathbf{B} , electric flux density \mathbf{D} . The source of the field can be the current density \mathbf{J} , voltage, etc. The material properties of the electrical machines are taken into account by the constitutive relation.

Here we only focus on the magneto-static and magneto-transient problems. We will also show how Maxwell's equations could be reduced to one or two partial differential equations using potential.

This chapter gives a summary of Maxwell's equations, interface conditions, and potential formulations. For a more detailed explanation, please see [40].

1.1 Maxwell's equations and interface conditions

1.1.1 Differential form of Maxwell's equations

The Maxwell's equations are the collection of laws and theorem proposed by (Gauss, Ampère, Faraday) that explains and defines the relations between electromagnetic field quantity and source [63]. The following relations in partial differential form define as:

$$\mathbf{curl} \mathbf{H} = \mathbf{J}_e + \mathbf{J}_s + \frac{\partial \mathbf{D}}{\partial t}, \quad \text{Maxwell} - \text{Ampere}, \quad (1.1)$$

$$\mathbf{curl} \mathbf{E} = -\frac{\partial \mathbf{B}}{\partial t}, \quad \text{Maxwell} - \text{Faraday}, \quad (1.2)$$

$$\mathbf{div} \mathbf{B} = 0, \quad \text{Maxwell} - \text{Thomson}, \quad (1.3)$$

$$\mathbf{div} \mathbf{D} = q \quad \text{Maxwell} - \text{Gauss}, \quad (1.4)$$

Here,

- \mathbf{E} electric field intensity in V.m^{-1} ,
- \mathbf{H} the magnetic field intensity in A.m^{-1} ,
- \mathbf{D} the electric flux density in C.m^{-2}
- \mathbf{B} magnetic flux density in T,
- \mathbf{J}_s the electric current density of the coil conductor in A.m^{-2} . It is also the source of electromagnetic field,
- \mathbf{J}_e the electric current density induced in the solid conductor in A.m^{-2} .
- q is the electric charge density in C.

1.1.2 Constitutive Relations

Constitutive relation is a relation between two physical quantities that is specific to the properties of a material.

$$\mathbf{B} = \mu \mathbf{H} \text{ or } \mathbf{H} = \nu \mathbf{B} \text{ (Constitutive equations - Magnetic)} \quad (1.5)$$

$$\mathbf{J}_e = \sigma \mathbf{E} \text{ or } \mathbf{E} = \rho \mathbf{J}_e \text{ (Constitutive equations - Electric)} \quad (1.6)$$

where, ' μ ' is the magnetic permeability in H.m^{-1} , ' ν ' is the magnetic reluctivity in $\text{H}^{-1}.\text{m}$, ' σ ' is the electrical conductivity in $\Omega^{-1}.\text{m}^{-1}$ and ' ρ ' is the electrical resistivity in $\Omega.\text{m}$.

1.1.3 Boundary and Interface Conditions

Let Ω be the domain of interest and Γ be its boundary. It is necessary to define correct boundary conditions on Γ , to obtain a unique solution for the studied problem.

Boundary conditions

Let Γ for magnetic quantities can be decomposed into Γ_h and Γ_b . Such that $\Gamma = \Gamma_h \cup \Gamma_b$ and $\Gamma_h \cap \Gamma_b = \emptyset$.

Therefore,

$$\mathbf{n} \times \mathbf{H}|_{\Gamma_h} = 0, \quad (1.7)$$

$$\mathbf{n} \cdot \mathbf{B}|_{\Gamma_b} = 0. \quad (1.8)$$

The above described condition signifies that the magnetic field \mathbf{H} is normal to the surface Γ_h and its tangential component is null. Similarly, for the magnetic flux density \mathbf{B} is tangential to the surface Γ_b and its normal component is null.

Let Γ for electric quantities can be break into Γ_e and Γ_j . Such that $\Gamma = \Gamma_e \cup \Gamma_j$ and $\Gamma_e \cap \Gamma_j = \emptyset$.

Therefore,

$$\mathbf{n} \times \mathbf{E}|_{\Gamma_e} = 0, \quad (1.9)$$

$$\mathbf{n} \cdot \mathbf{J}|_{\Gamma_j} = 0. \quad (1.10)$$

Only one of the two defined conditions is applied on the edge of the boundary Γ in 2D or on the face of the boundary Γ in 3D from magnetic quantities and electrical quantities respectively.

Interface Condition

At the interface between two materials, the discontinuous distribution of fields is observed. The discontinuous distribution is known as the interface conditions.

To define the interface conditions, let us consider an interface Γ_{12} normal to ' \mathbf{n} ' between two domains Ω_1 and Ω_2 as shown in fig.(1.1). The fields are designated

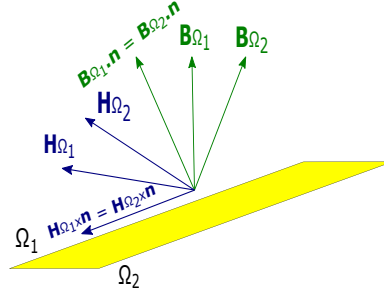


Figure 1.1 – Representation of interface between two domains.

with indices 1 and 2 on their respective domains. Then magnetic and electric fields components must satisfy the following conditions:

$$\mathbf{n} \times (\mathbf{H}_1 - \mathbf{H}_2)|_{\Gamma_{12}} = \mathbf{J}_s, \quad (1.11)$$

$$\mathbf{n} \cdot (\mathbf{J}_{e1} - \mathbf{J}_{e2})|_{\Gamma_{12}} = \frac{\partial \rho_s}{\partial t}, \quad (1.12)$$

$$\mathbf{n} \times (\mathbf{E}_1 - \mathbf{E}_2)|_{\Gamma_{12}} = 0, \quad (1.13)$$

$$\mathbf{n} \cdot (\mathbf{B}_1 - \mathbf{B}_2)|_{\Gamma_{12}} = 0, \quad (1.14)$$

if there is no surface charge and surface current density (\mathbf{J}_s) on interface. Then (1.11 - 1.12) are defined as:

$$\mathbf{n} \times (\mathbf{H}_1 - \mathbf{H}_2)|_{\Gamma_{12}} = 0, \quad (1.15)$$

$$\mathbf{n} \cdot (\mathbf{J}_{e1} - \mathbf{J}_{e2})|_{\Gamma_{12}} = 0. \quad (1.16)$$

This section defines the set of equations and boundary conditions necessary to define the electromagnetic problem. The next section will illustrate the boundary value problem under magneto-static and magneto-transient scenarios using Maxwell's equations, as mentioned above, with appropriate boundary conditions.

1.2 Magneto-static and magneto-transient problem

This section will formulate the mathematical model for the magneto-static and magneto-transient problem—the most typical problem found in the electrical engineering application with proper equations, interface, and boundary conditions.

1.2.1 Magneto-Static problem

The magneto-static problem deals with the distribution of the magnetic field caused by time-invariant currents or permanent magnets. The fig.(1.2) depicts the setup for magneto-static problem. In the magneto-static scenario, the source current density \mathbf{J}_s generates magnetic field \mathbf{H} , as mentioned above the interaction between magnetic field \mathbf{H} and electric field \mathbf{E} is neglected. After considering the above considerations, the following Maxwell's equations (1.1)-(1.6) can be written as:

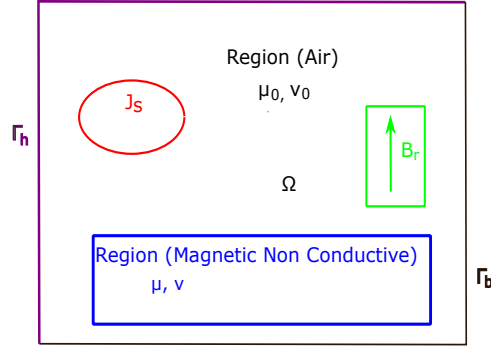


Figure 1.2 – Domain representation of magnetostatic field problem.

$$\mathbf{curl} \mathbf{H} = \mathbf{J}_s, \quad (1.17)$$

$$\mathbf{div} \mathbf{B} = 0, \quad (1.18)$$

$$\mathbf{div} \mathbf{J}_s = 0, \quad (1.19)$$

$$\mathbf{H} = \nu(\mathbf{B} - \mathbf{B}_r), \quad (1.20)$$

$$\mathbf{n} \times \mathbf{H}|_{\Gamma_h} = 0, \quad (1.21)$$

$$\mathbf{n} \cdot \mathbf{B}|_{\Gamma_b} = 0 \quad (1.22)$$

There are several potential formulations applicable to calculate the magnetostatic field problem. The principle behind using potential formulation is to reduce the number of partial differential Maxwell's equations for a detailed explanation see [40].

Magnetic vector potential (A - formulation)

The magnetic vector potential is defined by

$$\mathbf{B} = \mathbf{curl} \mathbf{A}, \quad (1.23)$$

it exactly satisfy the identity $\mathbf{div} \mathbf{curl} \mathbf{v} = 0$ for any vector function $\mathbf{v} = \mathbf{v}(\mathbf{x})$, here \mathbf{x} is the position of vector \mathbf{v} . Substituting the vector potential in Maxwell's equations and with the utilisation of constitutive relation, it leads to

$$\mathbf{curl} (\nu \mathbf{curl} \mathbf{A}) = \mathbf{J}_s + \mathbf{curl} (\nu \mathbf{B}_r), \quad (1.24)$$

$$\mathbf{n} \times \mathbf{curl} \mathbf{A}|_{\Gamma_h} = \mathbf{0}, \quad (1.25)$$

$$\mathbf{n} \times \mathbf{A}|_{\Gamma_b} = \mathbf{0}. \quad (1.26)$$

1.2.2 Magneto-transient Problem

Under magneto-transient scenario as shown in fig.(1.3), the electric field and magnetic field interact with each other. i.e. current flowing in coils generates magnetic field in the surrounding of the coil. The magnetic field varying with time generates

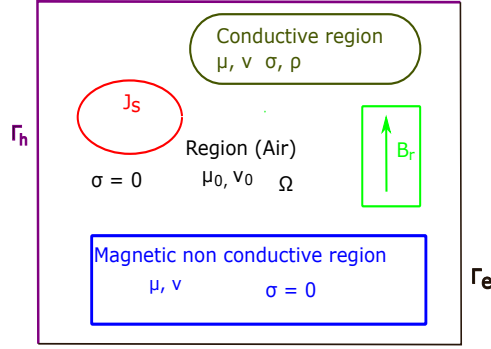


Figure 1.3 – Domain representation of magneto-transient field problem.

electric field in the conducting material.

$$\mathbf{curl} \mathbf{H} = \mathbf{J}_s + \mathbf{J}_e, \quad (1.27)$$

$$\mathbf{curl} \mathbf{E} = -\frac{\partial \mathbf{B}}{\partial t}, \quad (1.28)$$

$$\mathbf{div} \mathbf{B} = 0, \quad (1.29)$$

$$\mathbf{div} \mathbf{J}_e = 0, \quad (1.30)$$

$$\mathbf{div} \mathbf{J}_s = 0, \quad (1.31)$$

$$\mathbf{H} = \nu(\mathbf{B} - \mathbf{B}_r), \quad (1.32)$$

$$\mathbf{J}_e = \sigma \mathbf{E}, \quad (1.33)$$

$$\mathbf{n} \times \mathbf{H}|_{\Gamma_h} = 0, \quad (1.34)$$

$$\mathbf{n} \times \mathbf{E}|_{\Gamma_e} = 0. \quad (1.35)$$

The domain Ω of interest consist of two regions magnetic non conductive ($\mu, \sigma = 0$) and solid conductor ($\mu, \sigma \neq 0$). Let \mathbf{J}_s be the source current density given in coil and \mathbf{J}_e be the current induced due to change in magnetic field, \mathbf{B}_r represents magnets and $\Gamma = \Gamma_h \cup \Gamma_e$ be the boundary see fig.(1.3).

Eqn.(1.34) and eqn.(1.35) represents the tangential components of the magnetic field ' \mathbf{H} ' and the electric field ' \mathbf{E} ' represents at there respective boundary Γ_h and Γ_e as null.

Magnetic vector potential and electric scalar potential (A - V formulation)

The electric scalar potential 'V' is defined using eqn.(1.23) and eqn.(1.28) as:

$$\mathbf{E} = -\frac{\partial \mathbf{A}}{\partial t} - \mathbf{grad} V \quad (1.36)$$

1.3. SOURCE COMPUTATION USING MAGNETIC VECTOR POTENTIAL FORMULATION \mathbf{A}_j

Substituting eqn.(1.36) and eqn.(1.23) in equations (1.27 - 1.35) we get,

$$\mathbf{curl}(\nu \mathbf{curl} \mathbf{A}) + \sigma\left(\frac{\partial \mathbf{A}}{\partial t} + \mathbf{grad} V\right) = \mathbf{J}_s + \mathbf{curl}(\nu \mathbf{B}_r), \quad (1.37)$$

$$\mathbf{div}\left(\sigma\left(\frac{\partial \mathbf{A}}{\partial t} + \mathbf{grad} V\right)\right) = 0, \quad (1.38)$$

$$\mathbf{n} \times \mathbf{curl} \mathbf{A}|_{\Gamma_h} = 0, \quad (1.39)$$

$$\mathbf{n} \times \mathbf{A}|_{\Gamma_e} = 0, \quad (1.40)$$

$$\mathbf{n} \cdot \mathbf{grad} V|_{\Gamma_h} = 0, \quad (1.41)$$

$$V|_{\Gamma_e} = 0. \quad (1.42)$$

In the next section, we will study source computation using magnetic vector potential formulation \mathbf{A}_j under reduced domain.

1.3 Source computation using magnetic vector potential formulation \mathbf{A}_j

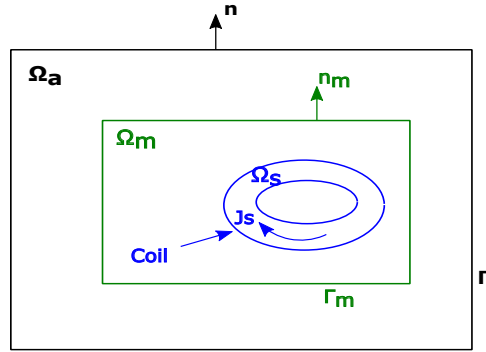


Figure 1.4 – Domain representation for source computation.

In this section, we present source computation using magnetic vector potential \mathbf{A}_j . Here we present the formulation for source computed over reduced domain Ω_m . This technique, we will be utilizing in the case of rotating electrical machine. Using this formulation, we don't need to ensure continuity between moving and fixed parts of electrical machines for source computation.

Let Ω be the domain and Γ be its boundary. Such that $\Omega = \Omega_a \cup \Omega_m$. Let coil inside the domain Ω_m . Let Ω_s be the domain of coil with current density defined as \mathbf{J}_s . Here, we assume Ω_s does not touch the boundary Γ_m .

Let us recall the equation represent problem shown in fig.(1.4).

$$\mathbf{J}_s = \mathbf{curl} \mathbf{H}_s, \quad (1.43)$$

$$= \mathbf{curl} \mathbf{H}_j, \quad (1.44)$$

$$= \mathbf{curl}(\nu \mathbf{curl} \mathbf{A}_j). \quad (1.45)$$

here \mathbf{H}_s is the source magnetic field computed analytically. \mathbf{H}_j is the projection of \mathbf{H}_s . For more detail regarding \mathbf{H}_j and \mathbf{A}_j computation, please see eqn.(A.5) and eqn.(A.7).

1.4 Summary

In this chapter, we have presented the magneto-static problem using \mathbf{A} formulation and magneto transient problem, using \mathbf{A} -V formulation.

To overcome the continuity of source computation between moving and fixed part of an electrical machine, a new formulation is presented for source computation under magnetic vector potential formulation \mathbf{A}_j .

In the next chapter, we will present the definition of functional spaces, weak form and the finite element approximation of aforementioned problem description.

Chapter 2

Numerical Modeling of low frequency Maxwell equations using edge finite element method

Contents

2.1	Functional Spaces	15
2.1.1	Lebesgue Spaces	15
2.1.2	Sobolev Spaces	15
2.1.3	Functional spaces for differential operators	15
2.1.4	Tonti Diagram	16
2.2	Finite Element Method	17
2.2.1	Approximation spaces	17
2.2.2	Mapped finite element (Reference element and real element)	18
2.2.3	Shape functions	18
2.3	Application of finite element for approximating magneto static problem	20
2.3.1	Weak form of magneto-static problem	20
2.3.2	Discretized modeling using finite element method	21
2.4	Application of finite element for approximating magneto-transient problem	21
2.4.1	Weak form of magneto-transient problem	22
2.4.2	Discretized modeling using finite element method	22
2.5	Application of finite element for source computation using magnetic vector potential formulation A_j under reduced domain	24
2.5.1	Weak form	24
2.5.2	Discretized modeling using finite element method	24
2.6	Summary	25

This chapter will introduce vector spaces that are standard settings for studying and solving the differential form of Maxwell equations. After this, we will present a brief theory on the finite element method and its application on approximating boundary value problems presented in chapter - 1.

2.1 Functional Spaces

Let $\Omega \in \mathbb{R}^3$ be the domain of interest with its boundary defined as Γ . It is a Euclidean vector space. In the below section, we will define the space on which the above mentioned partial differential equations are defined.

2.1.1 Lebesgue Spaces

Let $L^2(\Omega)$ be the square-integrable scalar space and $\mathbf{L}^2(\Omega)$ be the square-integrable vector space (for detail description see [9, 10]), defined as:

$$L^2(\Omega) = \left\{ u : \Omega \rightarrow \mathbb{R} \mid \int_{\Omega} (u(\mathbf{x}))^2 d\Omega < \infty \right\} \quad (2.1)$$

$$\mathbf{L}^2(\Omega) = \left\{ \mathbf{u} : \Omega \rightarrow \mathbb{R}^3 \mid \int_{\Omega} \|\mathbf{u}(\mathbf{x})\|^2 d\Omega < \infty \right\} \quad (2.2)$$

2.1.2 Sobolev Spaces

Let us define the Sobolev space $H^1(\Omega)$ and $\mathbf{H}^1(\Omega)$. The Sobolev space in general contains both function and its derivative (for detail description see [6, 9, 10]).

$$H^1(\Omega) = \left\{ u \in L^2(\Omega), \frac{\partial u}{\partial x_i} \in L^2(\Omega) \forall i = 1, \dots, n \right\} \quad (2.3)$$

$$\mathbf{H}^1(\Omega) = \left\{ \mathbf{u} \in \mathbf{L}^2(\Omega), \frac{\partial \mathbf{u}}{\partial x_i} \in \mathbf{L}^2(\Omega) \forall i = 1, \dots, n \right\} \quad (2.4)$$

2.1.3 Functional spaces for differential operators

For our remembrance magneto-static model uses three differential operators. The operators are gradient noted as **grad**, curl noted as **curl** and divergence noted as *div*. For each operator, we define a closed Hilbert space in which the operators are defined. The definition of spaces are:

$$H(\mathbf{grad}, \Omega) = \{ u \in L^2(\Omega) \mid \mathbf{grad} u \in \mathbf{L}^2(\Omega) \} \quad (2.5)$$

$$H(\mathbf{curl}, \Omega) = \{ \mathbf{u} \in \mathbf{L}^2(\Omega) \mid \mathbf{curl} \mathbf{u} \in \mathbf{L}^2(\Omega) \} \quad (2.6)$$

$$H(\mathbf{div}, \Omega) = \{ \mathbf{u} \in \mathbf{L}^2(\Omega) \mid \mathbf{div} \mathbf{u} \in L^2(\Omega) \} \quad (2.7)$$

Let E_u^0, E_u^1, E_u^2 be the three subspaces of respective spaces define in (2.5)-(2.7) and Γ_u be the boundary associated to variable such that

2.1. FUNCTIONAL SPACES

$$E_u^0(\Omega) = \{u \in L^2(\Omega) \mid \mathbf{grad} u \in \mathbf{L}^2(\Omega), u|_{\Gamma_u} = \text{cst}\} \subset H(\mathbf{grad}, \Omega) \quad (2.8)$$

$$\mathbf{E}_u^1(\Omega) = \{\mathbf{u} \in \mathbf{L}^2(\Omega) \mid \mathbf{curl} \mathbf{u} \in \mathbf{L}^2(\Omega), \mathbf{n} \times \mathbf{u}|_{\Gamma_u} = 0\} \subset H(\mathbf{curl}, \Omega) \quad (2.9)$$

$$\mathbf{E}_u^2(\Omega) = \{\mathbf{u} \in \mathbf{L}^2(\Omega) \mid \text{div} \mathbf{u} \in L^2(\Omega), \mathbf{n} \cdot \mathbf{u}|_{\Gamma_u} = 0\} \subset H(\text{div}, \Omega) \quad (2.10)$$

$$E_u^3(\Omega) = \text{Codomain}(\text{div}) \quad (2.11)$$

Furthermore, the implications on boundary conditions are

$$u|_{\Gamma_u} = \text{constant} \Rightarrow \mathbf{n} \times \mathbf{grad} u|_{\Gamma_u} = \mathbf{0} \quad (2.12)$$

$$\mathbf{n} \times \mathbf{u}|_{\Gamma_u} = \mathbf{0} \Rightarrow \mathbf{n} \cdot \mathbf{curl} \mathbf{u}|_{\Gamma_u} = 0 \quad (2.13)$$

From (2.8)-(2.13) we deduce following inclusions:

$$\mathbf{grad} E_u^0 \subset \mathbf{E}_u^1 \quad (2.14)$$

$$\mathbf{curl} \mathbf{E}_u^1 \subset \mathbf{E}_u^2 \quad (2.15)$$

Finally, using (2.8)-(2.10) following conclusion can be drawn:

- A scalar function u in the space E_u^0 is continuous in the entire domain.
- The tangential component of vector field $\mathbf{u} \in E_u^1$ is continuous along two domains.
- The normal component of vector field $\mathbf{u} \in E_u^2$ is continuous across two domains.

Using De Rham complex above points can be represented as:

$$E_u^0 \xrightarrow{\mathbf{grad}} \mathbf{E}_u^1 \xrightarrow{\mathbf{curl}} \mathbf{E}_u^2 \xrightarrow{\text{div}} E_u^3 \quad (2.16)$$

2.1.4 Tonti Diagram

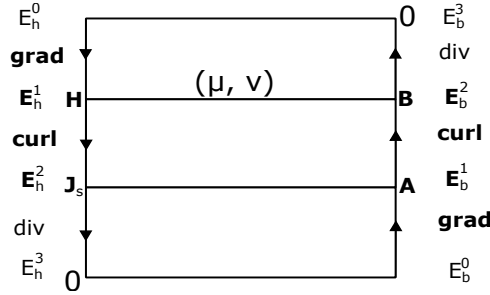


Figure 2.1 – Representation of Tonti diagram for Magneto-static scenario.

It is possible to classify variables and relations of continuous magneto-static and magneto-transient problem in a diagrammatic form. To do that, we represent the functional spaces E_h^i at the base of each step on which the variables are define. To move variables from one functional space to another functional space, we apply differential operators. After applying this concept, the two problems as shown in fig.(1.1) and fig.(1.2) are presented on Tonti diagram see fig.(2.1) and fig.(2.2) respectively.

The Tonti diagram is composed of two De Rham complexes E_h^p and E_b^p . Both complexes are interchangeable by the application of constitutive relation.

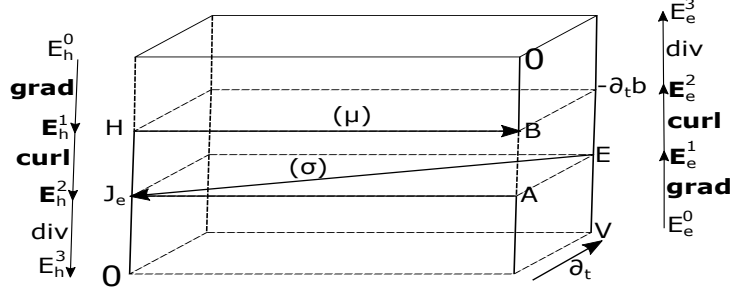


Figure 2.2 – Representation of Tonti diagram for Magneto-transient scenario.

2.2 Finite Element Method

Let the finite element is defined by (K, P_K, \sum_K) see [9]:

- K is an unit element of domain Ω . In three dimensional it can be tetrahedron, hexahedron, prism and pyramid etc.
- P_K is a functional space of dimension n_K defined over element K .
- \sum_K is a summation of n_K degree of freedoms over linear approximation u_i , where $1 \leq i \leq n_K$, defined on space P_K .

The finite element allows us to approximate the physical quantity 'u' over space P_K on element K as:

$$u_K(X) = \sum_{j=1}^{n_K} u_j w_j(X). \quad (2.17)$$

Here w_j is a basis of the space P_K . (2.17) states that the value $u_K(X)$ of the approximation function u_K at any point X in K is given by the linear combination of the basis functions w_j evaluated at point X with the u_j as coefficients.

2.2.1 Approximation spaces

To derive the edge and face basis functions, we need first to define the discrete functional spaces $W_u^0(\Omega)$, $\mathbf{W}_u^1(\Omega)$, $\mathbf{W}_u^2(\Omega)$, which are one on one mapped to there respective continuous functional spaces $E_u^0(\Omega)$, $\mathbf{E}_u^1(\Omega)$, $\mathbf{E}_u^2(\Omega)$, see (2.8)-(2.10) such that

$$W_u^0(\Omega) = \{w \in L^2(\Omega) \mid w|_K \in E_u^0(K), \forall K \in \Omega_h\} \quad (2.18)$$

$$\mathbf{W}_u^1(\Omega) = \{\mathbf{w} \in \mathbf{L}^2(\Omega) \mid \mathbf{w}|_K \in \mathbf{E}_u^1(K), \forall K \in \Omega_h\} \quad (2.19)$$

$$\mathbf{W}_u^2(\Omega) = \{\mathbf{w} \in \mathbf{L}^2(\Omega) \mid \mathbf{w}|_K \in \mathbf{E}_u^2(K), \forall K \in \Omega_h\} \quad (2.20)$$

where Ω_h is the discretized space of domain Ω , the definition for edge basis function is provided in sub-section 2.2.3.

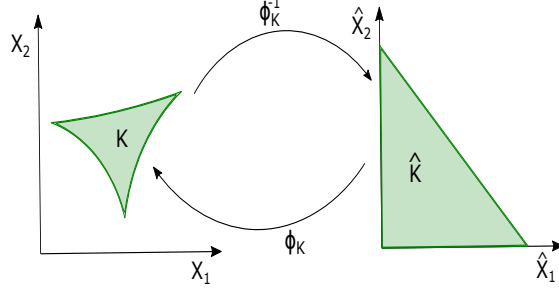


Figure 2.3 – Mapping reference element with real element using Jacobian operator.

2.2.2 Mapped finite element (Reference element and real element)

The concept of calculating interpolating shape function directly on the real element presents several limitations. The major drawback is the construction of shape function under the scenario where elements are distorted with the curvilinear boundaries. To overcome these limitations a new class of mapped finite element was developed. The objective of this section is to derive geometrical transformation that maps real complex element with simple reference elements as shown in fig.(2.3).

Let m be dimension of domain Ω , $m = 2$ for 2D and $m = 3$ for 3D. Let $K \subset \mathbb{R}^m$ corresponds to real element and $\hat{K} \subset \mathbb{R}^m$ corresponds to reference element. Let $\mathbf{x} = (x_1, \dots, x_m)$ be the coordinates of the real element K and $\hat{\mathbf{x}} = (\hat{x}_1, \dots, \hat{x}_m)$ be the coordinates of the reference element \hat{K} .

Let Φ_K be a continuous and differential function. Then performs one on one mapping between real element K to reference element \hat{K} .

$$\begin{aligned} \Phi_K : \hat{K} &\rightarrow K \\ \hat{\mathbf{x}} &\rightarrow \Phi_K(\hat{\mathbf{x}}) = \mathbf{x}. \end{aligned} \quad (2.21)$$

Also the inverse of the function Φ_K , Φ_K^{-1} is defined as $\Phi_K^{-1}(\mathbf{x}) = \hat{\mathbf{x}}, \forall \mathbf{x} \in K$. Using this theory, we now can define the transformation matrix also known as Jacobian matrices.

$$J_{K,i,j}(\hat{\mathbf{x}}) = \left(\frac{\partial \phi_{K,i}}{\partial \hat{x}_j}(\hat{x}_j) \right) \quad (2.22)$$

This relation allows us to define function u on real element and also \hat{u} on reference element. In below table.2.1 we provide the transformation for operators **grad**, **curl**, **div** for more detailed explanation see [25].

Finally, the transformation allows us to calculate shape functions on reference space and mapped it to real space.

2.2.3 Shape functions

In 3D nodal finite element (Lagrangian-element) due to lack of the divergence condition, non-physical solutions were observed. Second, the imposition of boundary

Domain \hat{K}	\mathbf{u} as a function $\hat{\mathbf{u}}$	operator on \mathbf{u} as a function $\hat{\mathbf{u}}$
$\mathbf{H}(\mathbf{grad}, \hat{K})$	$u = \hat{u}(\Phi_K^{-1})$	$\mathbf{grad} u = J_K^{-T} \mathbf{grad} \hat{u}(\Phi_K^{-1})$
$\mathbf{H}(\mathbf{curl}, \hat{K})$	$\mathbf{u} = J_K^{-T} \hat{\mathbf{u}}(\Phi_K^{-1})$	$\mathbf{curl} \mathbf{u} = \frac{J_K}{\det(J_K)} \mathbf{curl} \hat{\mathbf{u}}(\Phi_K^{-1})$
$\mathbf{H}(\mathbf{div}, \hat{K})$	$\mathbf{u} = \frac{J_K}{\det(J_K)} \hat{\mathbf{u}}(\Phi_K^{-1})$	$\mathbf{div} \mathbf{u} = \frac{1}{\det(J_K)} \mathbf{div} \hat{\mathbf{u}}(\Phi_K^{-1})$

Table 2.1 – Piola transformation.

condition at the material interface found to be inconvenient for more detail refer [28].

To overcome these challenges, a new type form of finite element was proposed by Nedelec see [44]. Where, we use vector shape function that assign degree of freedoms to the edges and faces rather than to the nodes of the element. Below, we will provide the definition of the first order incomplete edge shape function and face shape function.

Nodal shape functions

Let \mathbf{x}_i be the coordinate of node n_i . The nodal shape function $w_{n_i}^{ref}(\mathbf{x})$ for node n_i under reference coordinate is defined as:

$$w_{n_i}^{ref}(\mathbf{x}_j) = \begin{cases} 1 & \text{when } i = j, \\ 0 & \text{otherwise.} \end{cases} \quad (2.23)$$

Using Piola transformation, the nodal shape function $w_{n_i}(\mathbf{x})$ under real coordinate system is defined as:

$$w_{n_i}(\mathbf{x}) = w_{n_i}^{ref}(\Phi_k^{-1}(\mathbf{x})) \forall \mathbf{x} \in K, 1 \leq i \leq n_N. \quad (2.24)$$

here n_N is the total number of nodes.

Edge shape functions

We now introduce $\mathbf{w}_{\mathbf{a}_{ij}}$ be the edge basis function characterized on the space $\mathbf{W}_u^1(\Omega)$. Let \mathbf{a}_{ij} be the edge consist of two extreme nodes n_i and n_j . Let $\{i, \bar{j}\}$ be the face nodes which also include the node n_i of edge \mathbf{a}_{ij} but exclude the node n_j . Now, $\mathbf{w}_{\mathbf{a}_{ij}}$ be the edge shape function computed over edge \mathbf{a}_{ij} as:

$$\mathbf{w}_{\mathbf{a}_{ij}}^{ref} = w_{n_i}^{ref} \mathbf{grad} \left(\sum_{k \in \{i, \bar{j}\}} w_{n_k}^{ref} \right) - w_{n_j}^{ref} \mathbf{grad} \left(\sum_{l \in \{j, \bar{i}\}} w_{n_l}^{ref} \right) \quad (2.25)$$

$$\mathbf{w}_{\mathbf{a}_{ij}} = \mathbf{J}_k^{-T}(\Phi_k^{-1}(\mathbf{x})) \mathbf{w}_{\mathbf{a}_{ij}}^{ref}(\Phi_k^{-1}(\mathbf{x})) \quad (2.26)$$

$$\int_l \mathbf{w}_{\mathbf{a}_{ij}} \cdot d\mathbf{l} = \begin{cases} 1 & \text{along edge } \mathbf{a}_{ij} \\ 0 & \text{otherwise.} \end{cases} \quad (2.27)$$

Let w_{n_i} be the nodal basis function calculated at node ' i '. The line integral of $\mathbf{w}_{\mathbf{a}_{ij}}$ gives value 1 on an edge \mathbf{a}_{ij} and 0 on the other edge, as shown in (2.27).

2.3. APPLICATION OF FINITE ELEMENT FOR APPROXIMATING MAGNETO STATIC PROBLEM

It also shows that the tangential component of $\mathbf{w}_{\mathbf{a}_{ij}}$ is continuous along the edges. However, its normal component is not. The magnetic vector potential \mathbf{A} is defined on the functional space $\mathbf{W}_u^1(\Omega)$. The magnetic vector potential \mathbf{A} approximated on edge finite element as:

$$\mathbf{A} = \sum_{ij=1}^{n_A} A_{a_{ij}} \mathbf{w}_{\mathbf{a}_{ij}} \quad (2.28)$$

Here $A_{a_{ij}}$ is the circulation of the magnetic vector potential \mathbf{A} along edge a_{ij} of the mesh and n_A is the total number of edges.

Face shape functions

Let f_m be a face composed of nodes n_1, n_2, n_3 . The interpolating shape function for reference face element is defined as [21]:

$$\mathbf{w}_{f_m}^{ref} = a_{f_m} \sum_{k=1}^{n_{N_{f_m}}} w_{n_k}^{ref} \mathbf{grad} \left(\sum_{i \in \{n_k, \overline{n_{k+1}}\}} w_{n_i}^{ref} \right) \times \mathbf{grad} \left(\sum_{i \in \{n_k, \overline{n_{k-1}}\}} w_{n_i}^{ref} \right) \quad (2.29)$$

Here $n_{N_{f_m}}$ is the number of nodes on face f_m . a_{f_m} be the coefficient equal to 2 for triangle. Eqn.(2.29) calculate the interpolating shape function for reference face element. The interpolating shape function for real element w_{f_m} is defined as:

$$\mathbf{w}_{f_m} = \frac{\mathbf{J}_k(\Phi_k^{-1}(\mathbf{x}))}{\det(\mathbf{J}_k(\Phi_k^{-1}(\mathbf{x})))} \mathbf{w}_{f_m}^{ref}(\Phi_k^{-1}(\mathbf{x})) \forall \mathbf{x} \in K, 1 \leq m \leq n_F. \quad (2.30)$$

The vector field (interpolating shape function) \mathbf{w}_f has the following properties:-

- $\int_{f_m} \mathbf{w}_{f_m} \cdot d\mathbf{S} = \delta_{mn}$
- $\mathbf{w}_f \cdot \mathbf{n}$ the normal component is continuous across face element
- $\mathbf{w}_f \in \mathbf{W}_u^2(\Omega)$.

2.3 Application of finite element for approximating magneto static problem

Let \mathbf{A}' be a test function defined on space $\mathbf{E}_{u_0}^1(\Omega) = \{\mathbf{A}' \in \mathbf{E}_u^1(\Omega), \mathbf{A}'|_{\Gamma_e} = 0\}$ such that $\mathbf{curl} \mathbf{A}'$ belongs to space $\mathbf{L}^2(\Omega)$ and $\Gamma = \Gamma_h \cup \Gamma_b$.

2.3.1 Weak form of magneto-static problem

In this part we present the weak form for magneto static scenario (1.17 - 1.22) formulated using magnetic vector potential formulation \mathbf{A} .

$$\begin{aligned} (\nu \mathbf{curl} \mathbf{A}, \mathbf{curl} \mathbf{A}')_{\mathbf{L}^2(\Omega)} + \langle \nu \mathbf{n} \times \mathbf{curl} \mathbf{A}, \mathbf{A}' \rangle_{\mathbf{L}^2(\Gamma)} &= (\mathbf{J}_s, \mathbf{A}')_{\mathbf{L}^2(\Omega)} \\ &+ (\nu \mathbf{B}_r, \mathbf{curl} \mathbf{A}')_{\mathbf{L}^2(\Omega)} + \langle \nu \mathbf{n} \times \mathbf{B}_r, \mathbf{A}' \rangle_{\mathbf{L}^2(\Gamma)} \end{aligned} \quad (2.31)$$

Here the magnetic vector potential \mathbf{A} belongs to $\mathbf{E}_u^1(\Omega)$. As $\mathbf{n} \times \mathbf{curl} \mathbf{A}|_{\Gamma_h} = 0$ as shown in (1.25) and $\mathbf{A}'|_{\Gamma_e} = 0$, we can write $\langle \nu \mathbf{n} \times \mathbf{curl} \mathbf{A}, \mathbf{A}' \rangle_{\mathbf{L}^2(\Gamma)} = 0$. Again using (1.20) in limiting condition (1.21) and $\mathbf{A}'|_{\Gamma_e} = 0$, $\langle \nu \mathbf{n} \times \mathbf{B}_r, \mathbf{A}' \rangle_{\mathbf{L}^2(\Gamma)}$ becomes equal to zero. Therefore, equation (2.31) is reduced to:

$$(\nu \mathbf{curl} \mathbf{A}, \mathbf{curl} \mathbf{A}')_{\mathbf{L}^2(\Omega)} = (\mathbf{J}_s, \mathbf{A}')_{\mathbf{L}^2(\Omega)} + (\nu \mathbf{B}_r, \mathbf{curl} \mathbf{A}')_{\mathbf{L}^2(\Omega)} \quad (2.32)$$

2.3.2 Discretized modeling using finite element method

In this subsection, we present the discrete model of eqn.(2.32) using finite element approximation. Here \mathbf{A} belongs to $\mathbf{W}_u^1(\Omega)$ and test function \mathbf{A}' belongs to $\mathbf{W}_{u_0}^1(\Omega)$. Using finite element approximation eqn. (2.31) can be written as:

$$\begin{aligned} \sum_{k=1}^{n_A} A_{a_k} (\nu \mathbf{curl} \mathbf{w}_{a_k}(\mathbf{x}), \mathbf{curl} \mathbf{A}'(\mathbf{x}))_{\mathbf{L}^2(\Omega)} &= (\mathbf{J}_s(\mathbf{x}), \mathbf{A}'(\mathbf{x}))_{\mathbf{L}^2(\Omega)} \\ &+ (\nu \mathbf{B}_r(\mathbf{x}), \mathbf{curl} \mathbf{A}'(\mathbf{x}))_{\mathbf{L}^2(\Omega)} \end{aligned} \quad (2.33)$$

Using Galerkin method, the test function \mathbf{A}' is defined as $\mathbf{A}' = \mathbf{w}_{a_l}$ here 'l' varies between $[1, n_A]$. Now equation (2.33) is rewritten as:

$$\begin{aligned} \sum_{k=1}^{n_A} A_{a_k} (\nu \mathbf{curl} \mathbf{w}_{a_k}(\mathbf{x}), \mathbf{curl} \mathbf{w}_{a_l}(\mathbf{x}))_{\mathbf{L}^2(\Omega_h)} &= \sum_{l=1}^{n_A} (\nu \mathbf{curl} \mathbf{A}_j(\mathbf{x}), \mathbf{w}_{a_l}(\mathbf{x}))_{\mathbf{L}^2(\Omega_h)} \\ &+ \sum_{l=1}^{n_A} (\nu \mathbf{B}_r(\mathbf{x}), \mathbf{curl} \mathbf{w}_{a_l}(\mathbf{x}))_{\mathbf{L}^2(\Omega_h)} \end{aligned} \quad (2.34)$$

Here n_A is the total number of edges and Γ be the boundary of domain Ω . Finally we compute \mathbf{A} belongs to $\mathbf{W}_u^1(\Omega)$ by solving following problem:

$$R_{CC} \mathbf{A}_a = M_{JA} + M_{CB_r} \quad (2.35)$$

$$\mathbf{A}_a|_{\Gamma_b} = 0 \quad (2.36)$$

with

- $R_{CC} = \left[(\nu \mathbf{curl} \mathbf{w}_{a_k}, \mathbf{curl} \mathbf{w}_{a_l}) \right]_{1 \leq k, l \leq n_A}$
- $M_{JA} = \left[(\nu \mathbf{curl} \mathbf{A}_j, \mathbf{w}_{a_l}) \right]_{1 \leq l \leq n_A}$
- $M_{CB_r} = \left[(\nu \mathbf{B}_r, \mathbf{curl} \mathbf{w}_{a_l}) \right]_{1 \leq l \leq n_A}$
- $\mathbf{A}_a = \left[A_{a_k} \right]_{1 \leq k \leq n_A}$

2.4 Application of finite element for approximating magneto-transient problem

Let \mathbf{A}' be a test function defined on space $\mathbf{E}_{u_0}^1(\Omega) = \{\mathbf{A}' \in \mathbf{E}_u^1(\Omega), \mathbf{A}'|_{\Gamma_e} = 0\}$ such that $\mathbf{curl} \mathbf{A}'$ belongs to space $\mathbf{L}^2(\Omega)$. Similarly, \mathbf{V}' be a test function defined on space $\mathbf{E}_{u_0}^0(\Omega) = \{\mathbf{V}' \in \mathbf{E}_u^0(\Omega), \mathbf{V}'|_{\Gamma_e} = 0\}$ such that $\mathbf{grad} \mathbf{V}'$ belongs to space $\mathbf{L}^2(\Omega)$ and $\Gamma = \Gamma_h \cup \Gamma_e$.

2.4.1 Weak form of magneto-transient problem

In this part we present the weak form of the magneto-transient scenario derived using **A**-V formulation (1.37-1.42):

$$(\nu \mathbf{curl} \mathbf{A}, \mathbf{curl} \mathbf{A}')_{\mathbf{L}^2(\Omega)} + \langle \nu \mathbf{n} \times \mathbf{curl} \mathbf{A}, \mathbf{A}' \rangle_{\mathbf{L}^2(\Gamma)} + \left(\sigma \frac{\partial \mathbf{A}}{\partial t}, \mathbf{A}' \right)_{\mathbf{L}^2(\Omega)} + (\sigma \mathbf{grad} V, \mathbf{A}')_{\mathbf{L}^2(\Omega)} = (\mathbf{J}_s, \mathbf{A}')_{\mathbf{L}^2(\Omega)} + (\nu \mathbf{B}_r, \mathbf{curl} \mathbf{A}')_{\mathbf{L}^2(\Omega)} + \langle \nu \mathbf{n} \times \mathbf{B}_r, \mathbf{A}' \rangle_{\mathbf{L}^2(\Gamma)} \quad (2.37)$$

Here magnetic vector potential **A** belongs to $\mathbf{E}_u^1(\Omega)$. Since $\mathbf{n} \times \mathbf{curl} \mathbf{A}|_{\Gamma_h} = 0$ as shown in (1.39) and $\mathbf{A}'|_{\Gamma_e} = 0$; therefore, $\langle \nu \mathbf{n} \times \mathbf{curl} \mathbf{A}, \mathbf{A}' \rangle_{\mathbf{L}^2(\Gamma)}$ is equal to zero. By using (1.32) in (1.34) and $\mathbf{A}'|_{\Gamma_e} = 0$, we can rewrite $\langle \nu \mathbf{n} \times \mathbf{B}_r, \mathbf{A}' \rangle_{\mathbf{L}^2(\Gamma)}$ equal to zero. Therefore, now equation (2.37) is reduced to:

$$(\nu \mathbf{curl} \mathbf{A}, \mathbf{curl} \mathbf{A}')_{\mathbf{L}^2(\Omega)} + \left(\sigma \frac{\partial \mathbf{A}}{\partial t}, \mathbf{A}' \right)_{\mathbf{L}^2(\Omega)} + (\sigma \mathbf{grad} V, \mathbf{A}')_{\mathbf{L}^2(\Omega)} = (\mathbf{J}_s, \mathbf{A}')_{\mathbf{L}^2(\Omega)} + (\nu \mathbf{B}_r, \mathbf{curl} \mathbf{A}')_{\mathbf{L}^2(\Omega)} \quad (2.38)$$

The second equation under **A**-V formulation is defined as:

$$-\left(\sigma \frac{\partial \mathbf{A}}{\partial t}, \mathbf{grad} V' \right)_{\mathbf{L}^2(\Omega)} + \langle \sigma \mathbf{n} \cdot \frac{\partial \mathbf{A}}{\partial t}, V' \rangle_{\mathbf{L}^2(\Gamma)} - (\sigma \mathbf{grad} V, \mathbf{grad} V')_{\mathbf{L}^2(\Omega)} - \langle \sigma \mathbf{n} \cdot \mathbf{grad} V, V' \rangle_{\mathbf{L}^2(\Gamma)} = 0. \quad (2.39)$$

where electric scalar potential **V** belongs to $E_u^0(\Omega)$. Since $\mathbf{n} \cdot \mathbf{grad} V|_{\Gamma_h} = 0$, $V'|_{\Gamma_e} = 0$ and $\mathbf{n} \times \mathbf{curl} \mathbf{A}|_{\Gamma_h} = 0$ as shown in (1.41) and (1.39); therefore, $\langle \sigma \mathbf{n} \cdot \mathbf{grad} V, V' \rangle_{\mathbf{L}^2(\Gamma)}$ and $\langle \sigma \mathbf{n} \cdot \frac{\partial \mathbf{A}}{\partial t}, V' \rangle_{\mathbf{L}^2(\Gamma)}$ are equal to zero respectively. Now the equation (2.39) is rewritten as:

$$-\left(\sigma \frac{\partial \mathbf{A}}{\partial t}, \mathbf{grad} V' \right)_{\mathbf{L}^2(\Omega)} - (\sigma \mathbf{grad} V, \mathbf{grad} V')_{\mathbf{L}^2(\Omega)} = 0. \quad (2.40)$$

In the next subsection, we will present the magneto transient problem in discrete form.

2.4.2 Discretized modeling using finite element method

In this subsection, we present the discrete model of eqn.(2.38, 2.40) using finite element approximation. Here **A** belongs to $\mathbf{W}_u^1(\Omega)$ and test function **A'** belongs to $\mathbf{W}_{u_0}^1(\Omega)$. Similarly, **V** belongs to $W_u^0(\Omega)$ and test function **V'** belongs to $W_{u_0}^0(\Omega)$.

Using finite element approximation eqn. (2.37, 2.39) can be written as:

$$\begin{aligned} \sum_{k=1}^{n_A} A_{a_k} (\nu \mathbf{curl} \mathbf{w}_{a_k}(\mathbf{x}), \mathbf{curl} \mathbf{A}'(\mathbf{x}))_{\mathbf{L}^2(\Omega)} + \sum_{k=1}^{n_A} \frac{\partial A_{a_k}}{\partial t} (\sigma \mathbf{w}_{a_k}, \mathbf{A}'(\mathbf{x}))_{\mathbf{L}^2(\Omega)} + \\ \sum_{i=1}^{n_N} V_{n_i}(t) (\sigma \mathbf{grad} w_{n_i}, \mathbf{A}'(\mathbf{x}))_{\mathbf{L}^2(\Omega)} = (\mathbf{J}_s(\mathbf{x}), \mathbf{A}'(\mathbf{x}))_{\mathbf{L}^2(\Omega)} \\ + (\nu \mathbf{B}_r(t, \mathbf{x}), \mathbf{curl} \mathbf{A}'(\mathbf{x}))_{\mathbf{L}^2(\Omega)}, \end{aligned} \quad (2.41)$$

$$\begin{aligned} \sum_{k=1}^{n_A} \frac{\partial A_{a_k}}{\partial t} (\sigma \mathbf{w}_{a_k}, \mathbf{grad} V'(\mathbf{x}))_{\mathbf{L}^2(\Omega)} \\ + \sum_{i=1}^{n_N} V_{n_i}(t) (\sigma \mathbf{grad} w_{n_i}, \mathbf{grad} V'(\mathbf{x}))_{\mathbf{L}^2(\Omega)} = 0. \end{aligned} \quad (2.42)$$

Using Galerkin method, let test function \mathbf{A}' is defined as $\mathbf{A}' = \mathbf{w}_{a_l}$ here $l \in [1, n_A]$ and test function V' is defined as $V' = w_{n_j}$ here $j \in [1, n_N]$.

$$\begin{aligned} \sum_{k=1}^{n_A} A_{a_k} (\nu \mathbf{curl} \mathbf{w}_{a_k}(\mathbf{x}), \mathbf{curl} \mathbf{w}_{a_l}(\mathbf{x}))_{\mathbf{L}^2(\Omega)} + \sum_{k=1}^{n_A} \frac{\partial A_{a_k}}{\partial t} (\sigma \mathbf{w}_{a_k}, \mathbf{w}_{a_l}(\mathbf{x}))_{\mathbf{L}^2(\Omega)} + \\ \sum_{i=1}^{n_N} V_{n_i}(t) (\sigma \mathbf{grad} w_{n_i}, \mathbf{w}_{a_l}(\mathbf{x}))_{\mathbf{L}^2(\Omega)} = (\mathbf{J}_s(\mathbf{x}), \mathbf{w}_{a_l}(\mathbf{x}))_{\mathbf{L}^2(\Omega)} \\ + (\nu \mathbf{B}_r(t, \mathbf{x}), \mathbf{curl} \mathbf{w}_{a_l}(\mathbf{x}))_{\mathbf{L}^2(\Omega)}, \end{aligned} \quad (2.43)$$

$$\begin{aligned} \sum_{k=1}^{n_A} \frac{\partial A_{a_k}}{\partial t} (\sigma \mathbf{w}_{a_k}, \mathbf{grad} w_{n_j}(\mathbf{x}))_{\mathbf{L}^2(\Omega)} \\ + \sum_{i=1}^{n_N} V_{n_i}(t) (\sigma \mathbf{grad} w_{n_i}, \mathbf{grad} w_{n_j}(\mathbf{x}))_{\mathbf{L}^2(\Omega)} = 0. \end{aligned} \quad (2.44)$$

Here n_A and n_N are the total number of edges and the total number of nodes respectively. Γ_e be the electrical boundary of the domain Ω . Finally we compute \mathbf{A} belonging to $\mathbf{W}_u^1(\Omega)$ and V belonging to $\mathbf{W}_u^0(\Omega)$ by solving following problem:

$$R_{CC} \mathbf{A}_a + R_{AA} \frac{\partial \mathbf{A}_a}{\partial t} + R_{AG} \mathbf{V}_n = \mathbf{M}_{JA} + \mathbf{M}_{CB_r}, \quad (2.45)$$

$$R_{AG}^T \frac{\partial \mathbf{A}_a}{\partial t} + R_{GG} \mathbf{V}_n = \mathbf{0}, \quad (2.46)$$

$$\mathbf{A}_a|_{\Gamma_e} = \mathbf{0}, \quad (2.47)$$

$$V_n|_{\Gamma_e} = 0. \quad (2.48)$$

with

$$\bullet R_{CC} = \left[(\mu^{-1} \mathbf{curl} \mathbf{w}_{a_k}(\mathbf{x}), \mathbf{curl} \mathbf{w}_{a_l}(\mathbf{x})) \right]_{1 \leq k, l \leq n_A}$$

$$\bullet \mathbf{A}_a = \left[A_{a_k}(t) \right]_{1 \leq k \leq n_A}$$

$$\bullet R_{AA} = \left[(\sigma \mathbf{w}_{a_k}(\mathbf{x}), \mathbf{w}_{a_l}(\mathbf{x})) \right]_{1 \leq k, l \leq n_A}$$

2.5. APPLICATION OF FINITE ELEMENT FOR SOURCE COMPUTATION USING MAGNETIC VECTOR POTENTIAL FORMULATION \mathbf{A}_j UNDER REDUCED DOMAIN

- $\mathbf{V}_n = [V_{n_i}(t)]_{1 \leq i \leq n_N}$
- $\mathbf{M}_{JA} = [\mathbf{J}_s(\mathbf{x}), \mathbf{w}_{a_l}(\mathbf{x})]_{1 \leq l \leq n_A}$
- $\mathbf{M}_{CB} = [\sigma \mathbf{B}_r(t, \mathbf{x}), \text{curl } \mathbf{w}_{a_l}(\mathbf{x})]_{1 \leq l \leq n_A}$
- $R_{GG} = [\sigma \text{grad } w_{n_i}(\mathbf{x}), \text{grad } w_{n_j}(\mathbf{x})]_{1 \leq i, j \leq n_N}$

2.5 Application of finite element for source computation using magnetic vector potential formulation \mathbf{A}_j under reduced domain

2.5.1 Weak form

In this part we present the weak form for source term \mathbf{J}_S computed using magnetic vector potential \mathbf{A}_j under reduced domain Ω_m , which is a semi-norm projection $\mathbf{H}(\text{curl}, \Omega)$ of magnetic source field \mathbf{H}_s computed analytically refer section 1.3.

$$(\mathbf{J}_s, \mathbf{A}')_{\mathbf{L}^2(\Omega_m)} = (\text{curl}(\nu \text{curl } \mathbf{A}_j), \mathbf{A}')_{\mathbf{L}^2(\Omega_m)} \quad \forall \mathbf{A}' \in \mathbf{E}_{u0}^1(\Omega), \quad (2.49)$$

$$= (\nu \text{curl } \mathbf{A}_j, \text{curl } \mathbf{A}')_{\mathbf{L}^2(\Omega_m)} + \langle \nu \mathbf{n} \times \text{curl } \mathbf{A}_j, \mathbf{A}' \rangle_{\mathbf{L}^2(\Gamma_m)} \quad (2.50)$$

2.5.2 Discretized modeling using finite element method

Using Galerkin method, let test function \mathbf{A}' is defined as $\mathbf{A}' = \mathbf{w}_{a_l}$ here 'l' varies between $[1, n_{A_m}]$. Now equation (2.49) is rewritten as:

$$(\mathbf{J}_s, \mathbf{w}_{a_l})_{\mathbf{L}^2(\Omega_m)} = (\nu \text{curl } \mathbf{A}_j, \text{curl } \mathbf{w}_{a_l})_{\mathbf{L}^2(\Omega_m)} + \langle \nu \mathbf{n} \times \text{curl } \mathbf{A}_j, \mathbf{w}_{a_l} \rangle_{\mathbf{L}^2(\Gamma_m)} \quad (2.51)$$

Here below $\mathbf{w}_{\omega_{a_l}}$ represents edges belongs to reduced domain (Ω_m) but excludes the edges belongs to (Γ_m). $\mathbf{w}_{\gamma_{a_l}}$ represents the edges belongs to the boundary of reduced domain.

$$\mathbf{w}_{a_l} = \mathbf{w}_{\omega_{a_l}} + \mathbf{w}_{\gamma_{a_l}}. \quad (2.52)$$

By using (2.52) in (2.51), eqn.(2.51) is rewritten as:

$$\begin{aligned} (\mathbf{J}_s, \mathbf{w}_{a_l})_{\mathbf{L}^2(\Omega_m)} &= (\nu \text{curl } \mathbf{A}_j, \text{curl } \mathbf{w}_{\omega_{a_l}})_{\mathbf{L}^2(\Omega_m)} + \langle \nu \mathbf{n} \times \text{curl } \mathbf{A}_j, \mathbf{w}_{\omega_{a_l}} \rangle_{\mathbf{L}^2(\Gamma_m)} \\ &\quad + (\nu \text{curl } \mathbf{A}_j, \text{curl } \mathbf{w}_{\gamma_{a_l}})_{\mathbf{L}^2(\Omega_m)} + \langle \nu \mathbf{n} \times \text{curl } \mathbf{A}_j, \mathbf{w}_{\gamma_{a_l}} \rangle_{\mathbf{L}^2(\Gamma_m)} \end{aligned} \quad (2.53)$$

The source is computed only on the edges belonging to $\Omega_m \setminus \Gamma_m$. Therefore, $\mathbf{w}_{\gamma_{a_l}}$ in eqn.(2.53) becomes zero and trace of $\mathbf{w}_{\omega_{a_l}}$ on (Γ_m) is also zero. Hence the final term is written as:

$$(\mathbf{J}_s, \mathbf{w}_{a_l})_{\mathbf{L}^2(\Omega_m)} = (\nu \text{curl } \mathbf{A}_j, \text{curl } \mathbf{w}_{\omega_{a_l}})_{\mathbf{L}^2(\Omega_m)}. \quad (2.54)$$

Finally, we present (2.54) in matrix form:

$$\mathbf{M}_{\mathbf{JA}} = \mathbf{M}_{\mathbf{JA}_{\Omega_m}}, \quad (2.55)$$

$$= \mathbf{M}_{R_{\Omega_m} \mathbf{curl} \mathbf{A}_{\Omega_m}}. \quad (2.56)$$

with,

$$\bullet \mathbf{M}_{\mathbf{JA}_{\Omega_m}} = \left[\mathbf{J}_s(\mathbf{x}), \mathbf{w}_{a_l}(\mathbf{x}) \right]_{1 \leq l \leq n_{A_{\Omega_m}}}.$$

$$\bullet \mathbf{M}_{R_{\Omega_m} \mathbf{curl} \mathbf{A}_{\Omega_m}} = \left[(\nu \mathbf{curl} \mathbf{A}_j, \mathbf{curl} \mathbf{w}_{a_l}) \right]_{1 \leq l \leq n_{A_{\Omega_m}}}.$$

2.6 Summary

In this chapter, the numerical modeling of magneto static and magneto transient scenarios has been studied using A formulation and A-V formulation respectively. We have also discussed briefly about the vector finite elements in the starting of this chapter.

In the next part, we are going to give detailed introduction about the methods that are developed to simulate movement in the electrical machines numerically modeled using finite element method.

Part II

Taking movement into account for magnetic vector potential formulation

Chapter 3

State of the art for taking movement into account

Contents

3.1	Taking movement into account in different frame of reference	29
3.1.1	Eulerian approach	29
3.1.2	Lagrangian approach	30
3.2	Methods based on volume air-gap principle	31
3.2.1	Remeshing	32
3.2.2	Macro element	33
3.2.3	Boundary element method	34
3.2.4	Overlapping finite element	34
3.3	Method based on sliding surface principle	35
3.3.1	Lock step method	36
3.3.2	Lagrange multiplier	37
3.3.3	Mortar method	38
3.3.4	Interpolation	39
3.3.5	Mixed finite element method / Natural element method .	40
3.4	Conclusion	40

The objective of this thesis is to model rotating electrical machine using magnetic vector potential. The machine is decomposed into two parts the moving part and the fixed part. In this chapter, we will study how to take into account movement in the numerical modelling of Maxwell's equation.

3.1 Taking movement into account in different frame of reference

Let Ω be the domain representing an electrical machine and $\Omega = \Omega_m + \Omega_f$. The rotating part of electrical machine is defined as Ω_m and the fixed part as Ω_f . Let the velocity with which the Ω_m is rotating is \mathbf{v} .

The methods to take into account movement are broadly classified under two popular approaches:

- The Eulerian approach: Under this approach, the frame of reference is fixed and independent to the position of domain Ω_m
- The Lagrangian approach: Under this approach, two frames of references are introduced one on domain Ω_m and other on Ω_f . The frame of reference on domain Ω_m is varying with change in the positioning of Ω_m .

Definition (Material derivative)

Let ϕ be the quantity of interest. In spatial description, attention is focused on space ' \mathbf{x} ' $\in \mathbb{R}^3$ occupied by the particle ' \mathbf{X} '. Here ' \mathbf{x} ' is the spatial coordinates and ' t ' represent time. Such that:

$$\phi = \phi(\mathbf{x}, t) \quad (3.1)$$

$$\mathbf{X}(\mathbf{x}, t_1) \neq \mathbf{X}(\mathbf{x}, t_2) \quad (3.2)$$

t_1 and t_2 represents particular instances of time ' t '. Under spatial description one thing should be noticed from eqn.(3.2) that particle ' \mathbf{X} ' during time t_1 isn't the same particle ' \mathbf{X} ' during time t_2 in the spatial coordinates ' \mathbf{x} '.

Under spatial description, the time derivative of ϕ is known as material derivative. It consist of two parts: the change in ϕ at space ' \mathbf{x} ' in time and change brought by the new particle. This is expressed as:

$$\frac{d\phi}{dt} = \frac{\partial\phi}{\partial t} + (\mathbf{v} \cdot \mathbf{grad})\phi \quad (3.3)$$

3.1.1 Eulerian approach

We have already observed in section 1.1 the magnetic component (\mathbf{H} and \mathbf{B}), and the electric component (\mathbf{E} and \mathbf{J}_e) varying both with respect to time and space.

To understand more precisely, let Ω_m of electrical machine be rotating with velocity ' \mathbf{v} '. Then change in magnetic flux density \mathbf{B} with respect to time ' t ' is written as:

$$\frac{d\mathbf{B}}{dt} = \frac{\partial\mathbf{B}}{\partial t} + (\mathbf{v} \cdot \mathbf{grad})\mathbf{B} \quad (3.4)$$

3.1. TAKING MOVEMENT INTO ACCOUNT IN DIFFERENT FRAME OF REFERENCE

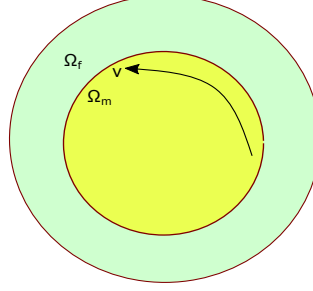


Figure 3.1 – Representation of electrical machine divided into two sub domains moving(Ω_m) and fixed(Ω_f).

Eqn.(3.4) represents the material derivative of ' \mathbf{B} ' in time ' t '. The first part in the right hand side of eqn.(3.4) ' $\frac{\partial \mathbf{B}}{\partial t}$ ' represents the change in ' \mathbf{B} ' with respect to time and second term in the right hand side represents convective derivative (change in ' \mathbf{B} ' with respect to space) and velocity ' \mathbf{v} '.

Using vector identity ($\mathbf{v} \cdot \text{grad} \mathbf{B}$) decomposed as:

$$(\mathbf{v} \cdot \text{grad} \mathbf{B}) = \mathbf{v} \text{div} \mathbf{B} - \text{curl}(\mathbf{v} \times \mathbf{B}) \quad (3.5)$$

Using eqn.(3.5) in (3.4), since $\text{div} \mathbf{B} = 0$ and $-\frac{\partial \mathbf{B}}{\partial t} = \text{curl} \mathbf{E}$, the Maxwell-Faraday law (1.2) in Eulerian approach defined as:

$$\frac{d\mathbf{B}}{dt} = -\text{curl}(\mathbf{E} + \mathbf{v} \times \mathbf{B}) \quad (3.6)$$

The main disadvantage of this method is the additional term ($\mathbf{v} \times \mathbf{B}$) in the Maxwell-Faraday equation makes the matrix system asymmetric. The method is numerically stable only with hexahedra meshes in the moving part for more information refer [39].

3.1.2 Lagrangian approach

Let us consider magnetic flux density ' \mathbf{B} ' be property of our interest. Such that for a particle position at ' \mathbf{X} ' at time ' t ' is written as:

$$\mathbf{B} = \mathbf{B}(\mathbf{X}, t) \quad (3.7)$$

In eqn.(3.7) the attention is focused on particle position in contrast to eqn.(3.1) where attention is focused on space. Therefore, the change in magnetic flux density \mathbf{B} with respect to time is written as:

$$\frac{d\mathbf{B}}{dt} = \frac{\partial \mathbf{B}}{\partial t} \quad (3.8)$$

The change in magnetic flux density \mathbf{B} with respect to space is not taken into account in Lagrangian approach.

When the movement is applied under Lagrangian approach the mesh of the rotor side moves leads to hanging nodes problem (Non conformed mesh) at the interface of moving part (rotor) and fixed part (stator) of electrical machine see fig.3.2.

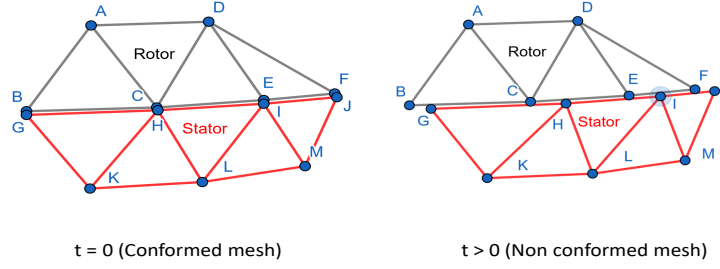


Figure 3.2 – Initial conformed mesh scenario becomes non conformed when the rotor part start moving.

To impose the continuity conditions (1.13-1.14) at the interface under non conformed mesh scenario several methods have been developed and studied under edge finite element but very little study has been carried out on comparing these methods on three dimensional industrial problem.

In the next section we will study the methods based on air-gap and sliding interface principle under Lagrangian approach.

3.2 Methods based on volume air-gap principle

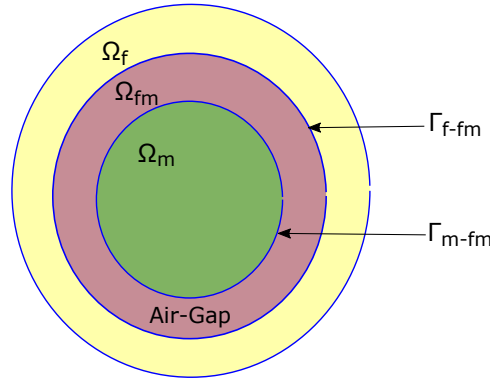


Figure 3.3 – Representation of airgap(Ω_{fm}) between two sub domains moving(Ω_m) and fixed(Ω_f) of an electrical machine.

The electrical machine (Ω) comprises of three sub-domains:

$$\Omega = \Omega_f \cup \Omega_m \cup \Omega_{fm} \quad (3.9)$$

$$\Gamma_{f-fm} = \Omega_f \cap \Omega_{fm} \quad (3.10)$$

$$\Gamma_{m-fm} = \Omega_m \cap \Omega_{fm} \quad (3.11)$$

where,

- Ω_f is the fixed part.
- Ω_m is the moving part.

- Ω_{fm} is the air-gap.
- Γ_{f-fm} and Γ_{m-fm} are the interfaces.

For more precise information please see fig.(3.3).

In this section, we will be discussing about the methods based on volume air-gap: remeshing, boundary integral method, macro element method and overlapping method.

3.2.1 Remeshing

To take movement into account the most simple way is to apply remeshing in the air-gap region (Ω_{fm}). The remeshing was first presented for rotating electrical machine using Delaunay adaptive rotating mesh in [54].

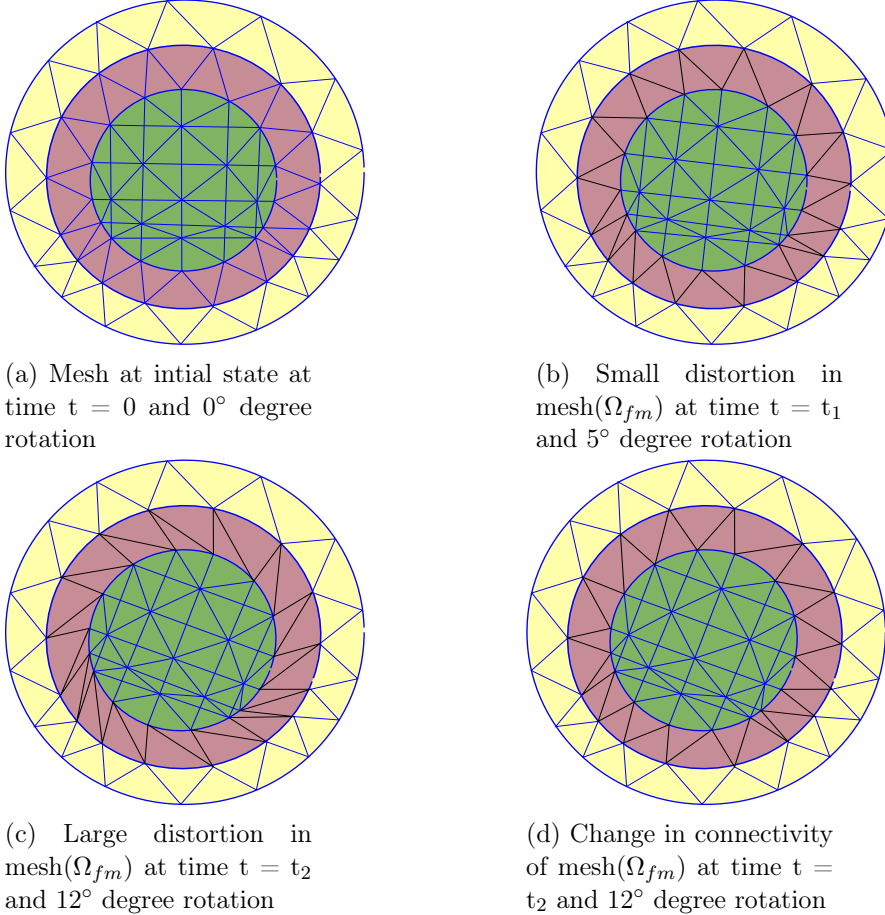


Figure 3.4 – Discretization process in the band (air-gap region Ω_{fm}).

The remeshing of the air-gap region Ω_{fm} is known as moving band method in [19, 57]. In the fig.(3.4), we presented the stages of distortion of mesh in the air-gap(Ω_{fm}), when movement is taken into account in an electrical machine. In fig.(3.5) the region marked with yellow color represents fixed part (Ω_f) of an electrical machine, similarly region marked with color green represents moving part (Ω_m). The

region between Ω_f and Ω_m is deemed as an air-gap. Now, we use this definition for fig.(3.4) such that fig.(3.4a) represents the initial conformed mesh when no movement is applied.

In fig.(3.4b) the electrical machine rotated to 5° degree from its initial position, a small distortion is noticed in the mesh of an air-gap region see fig.(3.4b). In fig.(3.4c) the moving part (Ω_m) has been rotated to 12° degree from its initial position and the scale of distortion has been increased to a level that it may affect the accuracy of result. Once the mesh has reached to maximum level of strain (distortion) change in connectivity of mesh (Ω_{fm}) performed as shown in fig.(3.4d).

No increment in the number of unknown is observed during remeshing. Today, we have robust algorithm available for remeshing (based on Delaunay triangulation). But, remeshing in 3D is still computationally very costly and sometimes if the air-gap isn't properly defined it disrupt the numerical solution.

To avoid these challenges in the next section we will present the method based on macro-element.

3.2.2 Macro element

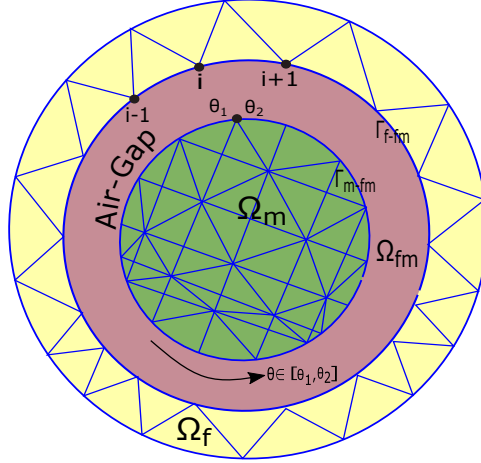


Figure 3.5 – 2D representation of airgap (Macro element) between two sub domains moving(Ω_m) and fixed(Ω_f) of an electrical machine.

The macro element technique is based on analytical expression for field computed in the region Ω_{fm} . In the macro element (air-gap Ω_{fm}) region the magnetic permeability μ is taken as constant and current density \mathbf{J} is equal to zero. For the first order nodal shape function refer [1] and for the second order shape function refer [24].

To ensure the continuity of the field on the interface between air-gap of both side of rotor ' Γ_{m-fm} ' and stator ' Γ_{f-fm} '. The boundary condition on the air-gap is described as:

$$A(r, \theta) = \sum_{i=J}^L \alpha_i(r, \theta) A_i \quad (3.12)$$

3.2. METHODS BASED ON VOLUME AIR-GAP PRINCIPLE

Here $J \in [1, L = S]$, if interface is Γ_{m-fm} and $J \in [1, L = T]$, if interface is Γ_{f-fm} . S and T are the total number of unknowns belongs to their respective interfaces. $\alpha_i(\theta)$ is the Lagrange polynomials refer [1].

The method presents good quality of results. In [1] it is shown the accuracy of results depends only on the quality of discretization of mesh in rotor and stator part of electrical machine.

Nevertheless, increase in computation times is noticed due to increase in the bandwidth of matrix. An improvement to this challenge was presented for 2D problem in [35]. The method shows promising results for 2D nodal finite element method, but turn out to be costlier in 3D finite element method due to dense matrix. The macro-element has never been tried with edge-finite element method.

3.2.3 Boundary element method

The coupling of finite element and boundary element method has proven to be an effective method for problem involving movement. For 2D problem and axis-symmetric problem, it was initially proposed by [58] and then extended to 2D electromagnetic field problem by [59]. In 3D hybrid finite element - boundary element method proposed by [41]-[13]-[33] and coupling with edge edge finite element in [13].

In general the method allows to approximate air region using boundary element method and the rest of the region approximated using finite element. This set of approximation allows us to retain non-linear property of finite element. To apply this method for our problem, regions Ω_f and Ω_m see fig.(3.5) are approximated using finite element. The interface $(\Gamma_{f-fm} \cup \Gamma_{m-fm})$ air-gap is approximated using boundary element. The boundary element method is a generalization of macro-element method in a way i.e. it is independent of interface geometry.

The advantage of the method is that the mesh at interface doesn't deformed and good accuracy of result is obtained. It is possible to apply this method for 3D problem using hybrid edge finite element - boundary element method. The main drawback of this method is the increase in bandwidth of matrix, which results in increase in computation time.

In the next sub-section, we will discuss overlapping finite element method based on volume air-gap. Where, we will try to find the answer regarding the improvement in computation time in contrast to macro-element and boundary element method.

3.2.4 Overlapping finite element

The overlapping method was first proposed by [62] for 2D problem to take movement into account. This method has been applied for 3D problem using hexahedron meshes in [15]-[30]. It was initially proposed for tetrahedron meshes and arbitrary meshes in [30]-[31]. The overlapping method was also proposed for edge elements [32].

In the overlapping method the meshes of stator (Ω_f) and rotor (Ω_m) are independently created, separated by an air-gap (Ω_{fm}) see fig.(3.6). At each step of rotation of domain (Ω_m) an overlapping mesh is created on a air-gap (Ω_{fm}) by performing orthogonal projection of nodes on opposite site.

To apply overlapping following steps are performed:-

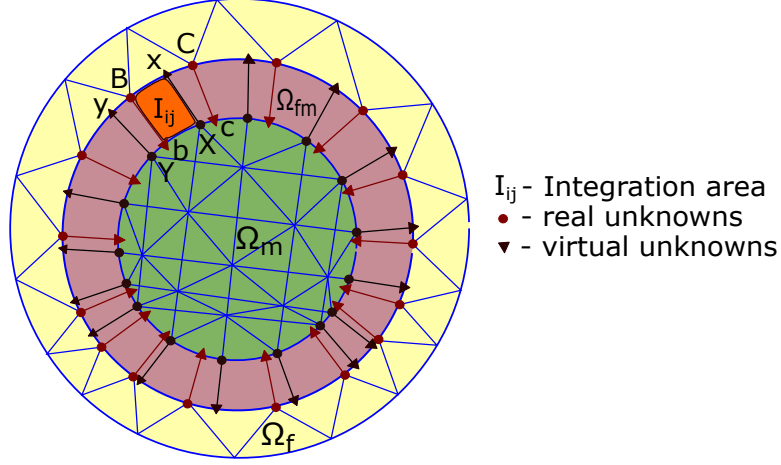


Figure 3.6 – Creation of overlapping meshes in the region Ω_{fm} by orthogonal projection of nodes.

- Projection:- The nodes B and C at Γ_{f-fm} are orthogonally projected as virtual nodes b and c at Γ_{m-fm} . Similarly, nodes X and Y belonging to Γ_{m-fm} are orthogonally projected as virtual nodes x and y at Γ_{f-fm} see fig.(3.6). The quadrangular virtual element BbXx is created in the region Ω_{fm} see fig.(3.6). In the case of 3D problem, the virtual element are hexahedron if the mesh are hexahedron and prism if the mesh is tetrahedron.
- Computation of integration area (I_{ij}):- To compute the integration area ' I_{ij} ' under edge finite element, edges (BC, XY, Bb, Xx) are considered see figure.(3.6). For nodal finite element considered nodes are B, C, X and Y. The virtual nodes shape function are not included for calculating basis. For element 'BbXx' \mathbf{A} is expressed as:

$$\mathbf{A} = A_{BC}\mathbf{W}_{BC} + A_{XY}\mathbf{W}_{XY} + A_{Bb}\mathbf{W}_{Bb} + A_{Xx}\mathbf{W}_{Xx} \quad (3.13)$$

where \mathbf{W} 's are the edge basis function and A's are the edge coefficient.

The advantage of the overlapping method is that it converges and matrix remains sparse. The quality of the solution is good even on irregular mesh. The accuracy of approximation decreases with increase in thickness of an air-gap. In edge element new unknowns are introduced in Ω_{fm} for more detail see [32]. However, the performance of overlapping method is improved in the case of edge element by neglecting edge unknowns in Ω_{fm} .

The creation of overlapping 3D element in the case of tetrahedron mesh is bit complex to implement for curved or arbitrary surface [30]-[31]. In the next section, we will discuss about the sliding interface principle and the methods based on sliding interface.

3.3 Method based on sliding surface principle

Under the sliding interface principle, the electrical machine is composed of two domains. Let fixed domain be represented as Ω_f and moving domain be represented

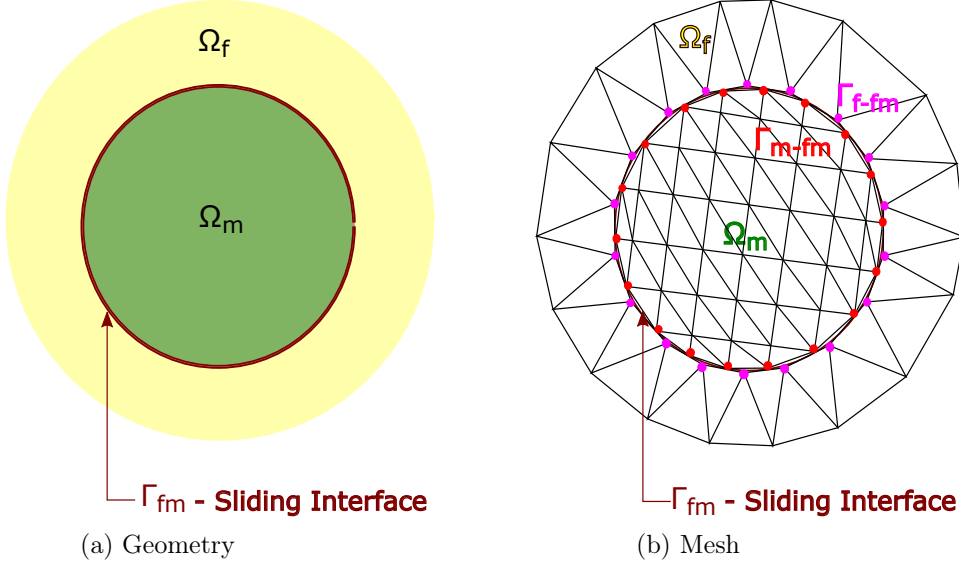


Figure 3.7 – 2D representation of sliding interface (Γ_{fm}) between two sub domains moving(Ω_m) and fixed(Ω_f) of an electrical machine.

as Ω_m , such that the interface between Ω_f and Ω_m is depicted as Γ_{fm} see fig.(3.7a) and known as sliding interface.

Some definitions:

- $\Omega = \Omega_f \cup \Omega_m$,
- $\Gamma_{fm} = \Omega_f \cap \Omega_m$.

To mesh the domain Ω two independent interfaces are created $\Gamma_{f-fm} \in \Omega_f$ and $\Gamma_{m-fm} \in \Omega_m$ along Γ_{fm} . Since the interface $\Gamma_{m-fm} \notin \Omega_f$, therefore Ω_m can freely slide or rotate along interface Γ_{fm} and Ω_f stays fixed along interface Γ_{fm} .

To explain more precisely above mentioned scenario, we will refer fig.(3.7b). In fig.(3.7b) mesh of domain Ω_f is coarser then mesh of domain Ω_m . The nodes (color) of interface mesh belonging to Γ_{m-fm} are in red, while for nodes belonging to Γ_{f-fm} in pink. The domain Ω_m is rotated to an angle of 5° , therefore we observe non conformed mesh at interface Γ_{fm} in fig.(3.7b).

In the coming sub-section, we will introduce method based on sliding interface principle: Lock-step method, penalty based methods, interpolation and some new horizons.

3.3.1 Lock step method

The lock-step method is one of the earliest and simplest technique adopted under sliding interface principle for taking movement into account. [49] demonstrates lock-step method for 2D induction motor analysis. [23]-[12] demonstrates for 3D induction motor.

In the lock-step method a band of regular mesh is generated along both sides of sliding interface Γ_{fm} . Here by regular mesh, we mean the size and the shape of each element of mesh is equal to one another. A representation of regular mesh along

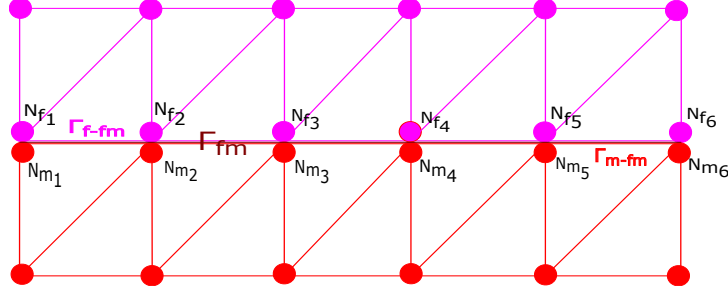


Figure 3.8 – Mesh position at initial state.

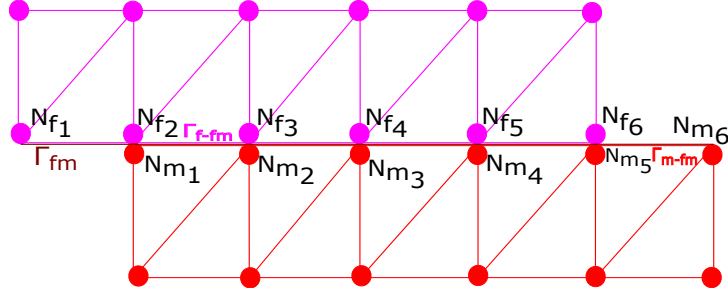


Figure 3.9 – Mesh position after movement

sliding interface Γ_{fm} is shown in fig.(3.8). In fig.(3.8) the elements and nodes in pink color depicts mesh of the fixed side Ω_f , the mesh in red color shows mesh of moving side Ω_m . The nodes of element along interface are represented as \mathbf{N}_{f_i} and \mathbf{N}_{m_i} respectively for Γ_{f-fm} and Γ_{m-fm} . Here $i \in [1, 6]$ for description see fig.(3.8).

To take movement into account using lock-step method, the time-step and rotation speed is defined such that at each step of rotation the mesh of mobile part (Ω_m) always remain conformed with mesh of fixed part (Ω_f) along the interface Γ_{fm} . To understand more precisely, fig.(3.8) represents mesh position at initial state ($t=0$), here nodes $\mathbf{N}_{f_i} \in \Gamma_{f-fm}$ are in front of nodes $\mathbf{N}_{m_i} \in \Gamma_{m-fm}$. Fig.(3.9) depicts positioning of mesh when movement is applied i.e. time ($t=t_1$), a change in combination take place and nodes $\mathbf{N}_{f_{i+1}} \in \Gamma_{f-fm}$ are in front of nodes $\mathbf{N}_{m_i} \in \Gamma_{m-fm}$.

The advantage of lock-step technique is mesh stays conformed at each step of rotation. The technique is simple to implement. The drawback of this technique is time-step is dependent on the rotation speed of moving part Ω_m .

The method can be implemented for both 2D and 3D problem with nodal finite element or edge finite element. In the next sub-section we will try discuss the methods that aren't dependent of regular band of mesh and rotation speed.

3.3.2 Lagrange multiplier

[55] showed the application of functional minimization using Lagrange multiplier to model a movement for 2D switch reluctance motor. [55] applied Lagrange multiplier for a problem formulated using magnetic vector potential \mathbf{A} on nodal finite elements. After this [38]-[34] extended its application for 3D problem formulated using magnetic vector potential formulation \mathbf{A} or magnetic scalar potential ϕ . [38] also showed Gaussian integration in the case tetrahedral mesh and [26] proposed the

3.3. METHOD BASED ON SLIDING SURFACE PRINCIPLE

method for edge finite elements.

$$\Pi = \int_{\Omega} (\mathbf{H} \text{curl} \mathbf{A} - \mathbf{A} \mathbf{J}_s) d\Omega \quad (3.14)$$

$$\Pi' = \int_{\Gamma_{fm}} \lambda (\mathbf{A}_{\Gamma_{f-fm}} - \mathbf{A}_{\Gamma_{m-fm}}) d\Gamma \quad (3.15)$$

Here Π in eqn.(3.14) describes a magnetostatic problem solved for unknown \mathbf{A} and Π' in eqn.(3.15) describe the coupling term introduced at the interface Γ_{fm} with Lagrange multiplier λ see [38].

The Lagrange multiplier method use sliding interface principle as shown in fig.(3.7). On each domain Ω_m and Ω_f eqn.3.14 is solved. To impose continuity on Γ_{fm} coupling term Π' eqn.3.15 is imposed on mesh interface i.e. on Γ_{f-fm} and Γ_{m-fm} . During solving, the Lagrange multiplier λ is replaced by their values calculated using functional minimization principle see [55]-[38]-[34].

The advantage of the method is the matrix remains symmetric. The method also posses several drawbacks and are listed below:

- The efficiency of method is highly dependent on choice of formulation. [38] showed when permeability of ferromagnetic material is increased, loss in accuracy was observed under ϕ formulation.
- The definition of integrating function on interface Γ_{fm} is difficult to define. The best form is to perform the intersection of meshes Γ_{f-fm} and Γ_{m-fm} and then use Gauss quadrature. However, the intersection becomes complex for 3D problem with tetrahedral meshes.
- The matrix becomes singular and ill-conditioned.
- Numerous numerical experiments have shown that the method is not effective for real applications and shows bad convergence with edge elements, when mesh consist of combination of hexahedron and tetrahedron elements.

Finally, we can conclude that Lagrange multiplier can be applied for 2D or 3D problem, even with edge finite element. But according to literature method proves to be in-efficient for real problems.

To overcome this challenge, In the next sub-section we will introduce mortar method, which is very close to Lagrange multiplier.

3.3.3 Mortar method

To take movement into account, the mortar method was first studied on 2D and 3D problem using nodal finite element by [50]-[16]-[17]-[5]. Then [51]-[52] extended it's application to 2D problem in edge finite element. In 3D edge finite element the method was proposed by [53]-[14]. Also in [60] this method was compared with interpolation based on accuracy and performance on nodal finite element.

In the mortar method solving a problem defined on domain Ω is equivalent to solving sub-problems defined on sub-domains Ω_f and Ω_m as $\Omega = \Omega_f \cup \Omega_m$. The continuity condition is imposed in a weak sense on sliding interface Γ_{fm} using Lagrange

type multiplier. In nodal finite element, the Lagrange type multiplier imposed continuity of unknowns through interface Γ_{fm} and in edge finite element the continuity is imposed of tangential component of unknowns along interface Γ_{fm} .

The unknowns belonging to mesh interfaces Γ_{f-fm} and Γ_{m-fm} are connected to each other by imposing the continuity. This connectivity or continuity are called in matrix representation as coupling matrices C and D.

In Lagrange multiplier method, we calculated ' λ ' using principle of minimization, whereas in mortar the unknowns in Lagrange type multiplier are replaced with functional form of Galerkin method. In mortar method coupling matrix 'C' is calculated using shape function of unknowns belonging to interface Γ_{f-fm} , whereas coupling matrix 'D' is dependent on shape functions of both interfaces i.e. Γ_{f-fm} and Γ_{m-fm} . Since, we are dealing with 3D curved interface, it is necessary to create third mesh (intermediate mesh between Γ_{f-fm} and Γ_{m-fm}) for accurate calculation of matrix 'D'.

The advantage of this method is it gives very accurate result, the order of accuracy is coherent to order of accuracy of conformed finite element. To maintain a good order of accuracy the intermediate mesh created for calculating matrix D is very fine almost four times and the inversion of the matrix C is full matrix. This increases computation time and computational memory for a problem.

In the next chapter, we will provide the detail description of mortar method. In the next sub-section, we will study another popular technique known as interpolation and try to find out the advantages and drawbacks of the method.

3.3.4 Interpolation

To take movement into account interpolation method was first proposed by [46]-[20] for 1st order interpolating function on nodal finite element. [60] proposed the 2nd and 3rd order interpolating function for 3D problems approximated using nodal finite elements. The interpolation on non conforming edge elements in 3D was proposed by [26]-[29]-[43]-[45]-[66].

On the sliding interface, the interpolation is carried out on a line for 2D problem and on a surface for 3D problem. The interpolation can be applied for nodal element, edge element and face element. The simplest form interpolation is nodal interpolation. The interpolation on edge element and face element is bit complex, especially on curved surface.

To give a simple example of the 1st order nodal interpolation for 2D problem see fig.(3.7b). In fig.(3.7b) the nodes N_{m_i} belonging to Γ_{m-fm} are not in coincident with nodes N_{f_i} belonging to Γ_{f-fm} . Under this scenario to impose the continuity using nodal interpolation, the nodal unknowns of interface Γ_{m-fm} are replaced with linear combination of nodal unknowns belongs to Γ_{f-fm} and each nodal unknowns belongs to Γ_{f-fm} in linear combination is multiplied by its weights known as interpolating coefficient. The same can be applied in the case of edge element but the calculation of interpolating coefficient is bit complex and will be described in the chapter-5.

The main advantage of this method is the resolution of matrix remain sparse and symmetrical. The performance of this method is really good as no intermediate mesh is created. Although, the accuracy of the method is affected in the case of first order incomplete edge element under the irregular mesh scenario. To overcome this shortcoming a third mesh is necessary created from intersecting elements of

3.4. CONCLUSION

interfaces Γ_{f-fm} and Γ_{m-fm} , which is again a complex task.

The method can be easily applied to 2D or 3D problems. The method has the capability to deliver the result of order of accuracy coherent to order of accuracy of finite elements.

In the next sub-section, we will give a small introduction on methods that holds a good prospects for taking movement into account.

3.3.5 Mixed finite element method / Natural element method

In a recent past, a new type of method has been developed, which attains the characteristics of meshless methods like the capability to cope up with geometrical changes and alleviation of computational cost due to mesh generation, but also retains the capability of FEM to impose the boundary condition at domain boundary see [64]-[65].

[27] proposed a constraint natural element method to take movement into account for 2D problem. [27] tested this approach on 2D variable reluctance motor. In [27] author proved by moving the nodes at the interface doesn't affect the accuracy of the solution. The method can be applied for magnetic vector potential formulation \mathbf{A} and also for magnetic scalar potential formulation ϕ . The extension of the method in edge element framework is complicated see [11].

3.4 Conclusion

Methods to take movement into account	2D	3D	Nodal FEM	Edge FEM	Intermediate Mesh	Accuracy	Performance
Remeshing	✓	✓	✓	✓	✓	✗	✗
Macro element	✓	✗	✓	✗	✗	✓	✓
Boundary Element Method	✓	✓	✓	✓	✗	✓	✗
Overlapping	✓	✓	✓	✓	✓	✓	✓
Lock-Step	✓	✓	✓	✓	✗	✓	✓
Lagrange Multiplier	✓	✓	✓	✓	✓	✗	✗
Mortar Method	✓	✓	✓	✓	✓	✓	✗
Interpolation	✓	✓	✓	✓	✗	✓	✓
C-NEM/Mixed FE	✓	✗	✓	✓	✗	✓	✓

Table 3.1 – Summary of methods to take movement into account.

The state of the art for the methods to take movement into account is summarized in table.(6.4). The method is chosen on four important criterion:

- Accuracy:- The method should have the capability to deliver results of accuracy in coherent with edge finite element theory.

- Third mesh (Intermediate mesh):- The implementation of an intermediate mesh should not be complicated.
- 3D problem:- The method should be capable of solving 3D problem under edge FEM framework.
- Performance:- The method shouldn't be computationally costly.

Four methods based on volume air-gap are studied. The first method remeshing has the capability to solve the 3D problem. Since the mesh at the interface is very fine to capture the physics accurately, remeshing at the interface becomes computationally costly and sometimes, the accuracy of results are also affected. Second, macro element method is difficult to apply in 3D because the resolution of matrix becomes dense and the method has never been tried on edge elements. Third, Boundary element method is difficult to apply for the reasons same as macro element method. Lastly, overlapping method has the ability to solve 3D problem with good accuracy. However, creation of intermediate mesh in the air-gap is complicated to implement for curved surfaces.

Again four methods under sliding interface principle are studied as well. Lock-step method is capable of solving 3D problem under edge element but the method is limited to regular mesh and rotation speed. Lagrange method failed to solve lacks the ability to solve real 3D test cases. Mortar method shows promising results in terms of robustness and accuracy in solving 3D problems under edge elements. Interpolation method respects all the criterion for taking movement into account.

Mixed finite element is new domain, it has shown promising results under 2D scenario for taking movement into account. It will be interesting to see its application on 3D problems. The application of mixed finite element seems bit difficult in the context of edge finite element.

Finally, three methods shows good prospects in 3D under edge elements to obtain good results for problem involving rotation movement: Interpolation, overlapping and mortar methods.

In this thesis, we are going to test interpolation and mortar methods. We will be leaving overlapping method out from comparison because the creation of intermediate mesh in the air-gap is complicated to implement for curved surfaces for this method.

Chapter 4

Mortar method

Contents

4.1	Theory of mortar method	43
4.1.1	Coupling matrices	43
4.1.2	Matrix structure after including coupling matrices	45
4.2	Implementation of mortar method	46
4.2.1	Integrating domain	46
4.2.2	Computation of coupling matrices	47
4.2.3	Inversion of coupling matrix C	49
4.3	Conclusion	50

In this chapter, we present the mortar method. Here, we will discuss in great detail about the mortar structure, the implementation of mortar method and the computation of coupling matrices.

4.1 Theory of mortar method

In the mortar method, the meshes at the interface of sub domains do not match, which introduces undesirable discontinuities in field along interface. Equality along the interface is imposed by using Lagrange type multiplier. To describe mortar method, we will be using similar notations as we have described in previous chapters. Let Ω be the domain of interest. The domain Ω is sub-divided into two sub-domains called as fixed domain Ω_f and moving domain Ω_m , $\Omega = \Omega_f \cup \Omega_m$. The sliding interface existing between two sub-domains is represented as Γ_{fm} , $\Gamma_{fm} = \Omega_f \cap \Omega_m$.

In practicality to impose sliding interface, the double surfaces (3D) or double interfaces (2D) are created along interface Γ_{fm} called as $\Gamma_{f-fm} = \Omega_f \cap \Gamma_{fm}$ (fixed side) and $\Gamma_{m-fm} = \Omega_m \cap \Gamma_{fm}$ (moving side).

The discretized domains and interfaces are defined as Ω_h , Ω_{fh} , Ω_{mh} and Γ_{f-fmh} , Γ_{m-fmh} respectively. In the next section, we will discuss in detail about the construction of Lagrange type multiplier and how it is imposed at the interfaces Γ_{f-fm} (fixed side) and Γ_{m-fm} (moving side) for ensuring the continuity of fields.

4.1.1 Coupling matrices

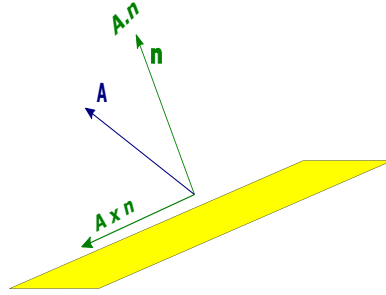


Figure 4.1 – Representation of vector components.

Let \mathbf{A} be the unknown defined on the edge of the finite element mesh. The unknown \mathbf{A} is composed of tangential and normal component defined as:

$$\mathbf{A} = (\mathbf{A} \cdot \mathbf{n})\mathbf{n} + (\mathbf{A} \times \mathbf{n}) \times \mathbf{n}. \quad (4.1)$$

Here \mathbf{n} represents the unit vector perpendicular to surface Γ_{fm} . $\mathbf{A} \cdot \mathbf{n}$ and $\mathbf{A} \times \mathbf{n}$ depicts the normal and the tangential components of \mathbf{A} see figure.(4.1).

Under 3D edge element, the continuity of the tangential component of unknown \mathbf{A} is imposed along interface Γ_{fm} . To impose the continuity Lagrange type multiplier \mathbf{A}' is used as:

$$\int_{\Gamma_{fm}} \mathbf{A}' (\mathbf{A} \times \mathbf{n}|_{\Gamma_{f-fm}} - \mathbf{A} \times \mathbf{n}|_{\Gamma_{m-fm}}) d\Gamma = 0. \quad (4.2)$$

4.1. THEORY OF MORTAR METHOD

Lets extend eqn.(4.2) on a discretized domain. But before that, lets define certain notations that will be utilized . Let n_{A_Ω} be the total number of edges on which unknown \mathbf{A} is approximated. Such that:

$$n_{A_\Omega} = n_{A_{\Omega_f}} + n_{A_{\Omega_m}} \quad (4.3)$$

where $n_{A_{\Omega_f}}$ and $n_{A_{\Omega_m}}$ be the total number of edges belonging to the fixed side and the moving side of a domain Ω . Let $\Omega_m \setminus \Gamma_{m-fm}$ and $\Omega_f \setminus \Gamma_{f-fm}$ be the discretized domain excluding the edges that approximates interfaces Γ_{m-fm} and Γ_{f-fm} respectively. Under this defined scenario the number of edge unknowns are defined as:

$$n_{A_{\Omega_f}} = n_{A_{\Omega_f \setminus \Gamma_{f-fm}}} + n_{A_{\Gamma_{f-fm}}} \quad (4.4)$$

$$n_{A_{\Omega_m}} = n_{A_{\Omega_m \setminus \Gamma_{m-fm}}} + n_{A_{\Gamma_{m-fm}}} \quad (4.5)$$

If we assume that we know the solution of unknown of \mathbf{A} , then on edge finite element space \mathbf{A} is approximated as:

$$\mathbf{A} = \sum_{i=1}^{n_{A_{\Omega_f \setminus \Gamma_{f-fm}}}} A_{a_{f_i}} \mathbf{w}_{a_{f_i}} + \sum_{j=1}^{n_{A_{\Gamma_{f-fm}}}} A_{a_{f_j}} \mathbf{w}_{a_{f_j}} + \sum_{k=1}^{n_{A_{\Omega_m \setminus \Gamma_{m-fm}}}} A_{a_{m_k}} \mathbf{w}_{a_{m_k}} + \sum_{l=1}^{n_{A_{\Gamma_{m-fm}}}} A_{a_{m_l}} \mathbf{w}_{a_{m_l}} \quad (4.6)$$

Here $\mathbf{w}_{a_{f_i}}$ is an edge basis function approximated over domain $\Omega_f \setminus \Gamma_{f-fm}$ and i belong to $1 \leq i \leq n_{A_{\Omega_f \setminus \Gamma_{f-fm}}}$. Similarly, this definition is extended for $\mathbf{w}_{a_{f_j}}$, $\mathbf{w}_{a_{m_k}}$ and $\mathbf{w}_{a_{m_l}}$. $A_{a_{f_i}}$, $A_{a_{f_j}}$, $A_{a_{m_k}}$ and $A_{a_{m_l}}$ are the expansion coefficients defined on edges $a_{f_i} \in \Omega_f \setminus \Gamma_{f-fm}$, $a_{f_j} \in \Gamma_{f-fm}$, $a_{m_k} \in \Omega_m \setminus \Gamma_{m-fm}$ and $a_{m_l} \in \Gamma_{m-fm}$.

Now using Galerkin method approximation of eqn.(4.6), the continuity condition eqn.(4.2) on finite element space is approximated as:

$$\sum_{j=1}^{n_{A_{\Gamma_{f-fm}}}} A_{a_{f_j}} \int_{\Gamma_{fm}} \mathbf{A}' \cdot (\mathbf{w}_{a_{f_j}} \times \mathbf{n}) d\Gamma = \sum_{l=1}^{n_{A_{\Gamma_{m-fm}}}} A_{a_{m_l}} \int_{\Gamma_{fm}} \mathbf{A}' \cdot (\mathbf{w}_{a_{m_l}} \times \mathbf{n}) d\Gamma. \quad (4.7)$$

Again using Galerkin method, the Lagrange multiplier \mathbf{A}' is approximated as:

$$\mathbf{A}' = \mathbf{w}_{a_{f_p}} \times \mathbf{n} \quad 1 \leq p \leq n_{A_{\Gamma_{f-fm}}} \quad (4.8)$$

Now lets write eqn.(4.7) in more compact form i.e. in matrix form:

$$C \mathbf{A}_{\Gamma_{f-fm} a} = D \mathbf{A}_{\Gamma_{m-fm} a}, \quad (4.9)$$

here,

- $C = [\int_{\Gamma_{f-fm}} (\mathbf{w}_{a_{f_p}} \times \mathbf{n}) \cdot (\mathbf{w}_{a_{f_j}} \times \mathbf{n}) d\Gamma]_{1 \leq p, j \leq n_{A_{\Gamma_{f-fm}}}} = [c_a(p, j)]_{1 \leq p, j \leq n_{A_{\Gamma_{f-fm}}}}$ is a coupling matrix.

- $D = [\int_{\Gamma_{fm}} (\mathbf{w}_{a_{fp}} \times \mathbf{n}) \cdot (\mathbf{w}_{a_{ml}} \times \mathbf{n}) d\Gamma]_{\substack{1 \leq p \leq n_{A_{\Gamma_{f-fm}}} \\ 1 \leq l \leq n_{A_{\Gamma_{m-fm}}}}} = [d_a(p, l)]_{\substack{1 \leq p \leq n_{A_{\Gamma_{f-fm}}} \\ 1 \leq l \leq n_{A_{\Gamma_{m-fm}}}}}$ is a coupling matrix.
- $\mathbf{A}_{\Gamma_{f-fm}a} = [A_{a_{fj}}]_{1 \leq j \leq n_{A_{\Gamma_{f-fm}}}}$ are the edge coefficients defined on edges $\in \Gamma_{f-fm}$.
- $\mathbf{A}_{\Gamma_{m-fm}a} = [A_{a_{ml}}]_{1 \leq l \leq n_{A_{\Gamma_{m-fm}}}}$ are the edge coefficients defined on edges $\in \Gamma_{m-fm}$.

Lets recall eqn.(4.7), the coupling matrix C is only computed on the interface Γ_{f-fm} . The coupling matrix C is a square matrix, as it is computed only on interface Γ_{f-fm} . Therefore, the size of coupling matrix C is $n_{A_{\Gamma_{f-fm}}} \times n_{A_{\Gamma_{f-fm}}}$. The idea behind calculating C just on interface Γ_{f-fm} is to avoid calculation of C at each step of movement. The calculation of coupling matrix D_a takes into account edges belonging to the interfaces Γ_{f-fm} and Γ_{m-fm} . The coupling matrix D is rectangular in size $n_{A_{\Gamma_{m-fm}}} \times n_{A_{\Gamma_{f-fm}}}$. As already discuss D is dependent on both interfaces Γ_{f-fm} and Γ_{m-fm} . Therefore, coupling matrix D is calculated at each step of rotation.

4.1.2 Matrix structure after including coupling matrices

Using (2.45) linear system of equations representing the problem imposed on domain Ω is defined as:

$$\mathbf{R}_{\Omega} \mathbf{A}_{\Omega} = \mathbf{M}_{\Omega} \quad (4.10)$$

here,

- \mathbf{R}_{Ω} is the stiffness matrix build on domain Ω ,
- \mathbf{A}_{Ω} is the vector containing unknowns approximated on domain Ω ,
- \mathbf{M}_{Ω} is the source vector on domain Ω .

Now we introduce two sub-domains Ω_f and Ω_m in eqn.(4.10). The eqn.(4.10) in block matrix form is written as:

$$\begin{bmatrix} \mathbf{R}_{\Omega_f} & 0 \\ 0 & \mathbf{R}_{\Omega_m} \end{bmatrix} \begin{bmatrix} \mathbf{A}_{\Omega_f} \\ \mathbf{A}_{\Omega_m} \end{bmatrix} = \begin{bmatrix} \mathbf{M}_{\Omega_f} \\ \mathbf{M}_{\Omega_m} \end{bmatrix} \quad (4.11)$$

Let us expand our main problem (4.11) by introducing continuity condition (4.9). Such that Ω_f is composed of $\Omega_f \setminus \Gamma_{f-fm} \cup \Gamma_{f-fm}$ and Ω_m is composed of $\Omega_m \setminus \Gamma_{m-fm} \cup \Gamma_{m-fm}$.

$$\begin{bmatrix} \mathbf{R}_{\Omega_f \setminus \Gamma_{f-fm}} & \mathbf{S}_{\Omega_f} & 0 & 0 \\ \mathbf{S}_{\Omega_f} & \mathbf{R}_{\Gamma_{f-fm}} & 0 & 0 \\ 0 & 0 & \mathbf{R}_{\Omega_m \setminus \Gamma_{m-fm}} & \mathbf{S}_{\Omega_m} \\ 0 & 0 & \mathbf{S}_{\Omega_m} & \mathbf{R}_{\Gamma_{m-fm}} \end{bmatrix} \begin{bmatrix} \mathbf{A}_{\Omega_f \setminus \Gamma_{f-fm}} \\ \mathbf{A}_{\Gamma_{f-fm}} \\ \mathbf{A}_{\Omega_m \setminus \Gamma_{m-fm}} \\ \mathbf{A}_{\Gamma_{m-fm}} \end{bmatrix} = \begin{bmatrix} \mathbf{M}_{\Omega_f \setminus \Gamma_{f-fm}} \\ \mathbf{M}_{\Gamma_{f-fm}} \\ \mathbf{M}_{\Omega_m \setminus \Gamma_{m-fm}} \\ \mathbf{M}_{\Gamma_{m-fm}} \end{bmatrix} \quad (4.12)$$

4.2. IMPLEMENTATION OF MORTAR METHOD

- \mathbf{S}_{Ω_f} is mass matrix that connects domain mesh $\Omega_f \setminus \Gamma_{f-fm}$ with interface mesh Γ_{f-fm} .
- \mathbf{S}_{Ω_m} is mass matrix that connects domain mesh $\Omega_m \setminus \Gamma_{m-fm}$ with interface mesh Γ_{m-fm} .

Since, the unknowns of fixed side Γ_{f-fm} are defined in accordance with moving side Γ_{m-fm} . Therefore, using the coupling matrices C and D the unknown vector \mathbf{A} in linear system of equation is re-written as:

$$\begin{bmatrix} \mathbf{A}_{\Omega_f \setminus \Gamma_{f-fm}} \\ \mathbf{A}_{\Gamma_{f-fm}} \\ \mathbf{A}_{\Omega_m \setminus \Gamma_{m-fm}} \\ \mathbf{A}_{\Gamma_{m-fm}} \end{bmatrix} = \begin{bmatrix} I & 0 & 0 \\ 0 & 0 & C^{-1}D \\ 0 & I & 0 \\ 0 & 0 & I \end{bmatrix} \begin{bmatrix} \mathbf{A}_{\Omega_f \setminus \Gamma_{f-fm}} \\ \mathbf{A}_{\Omega_m \setminus \Gamma_{m-fm}} \\ \mathbf{A}_{\Gamma_{m-fm}} \end{bmatrix} \quad (4.13)$$

After replacing unknown vector \mathbf{A} by eqn.(4.13) in eqn.(4.12). It leads to new orientation of linear system of equation in matrix form:

$$\begin{bmatrix} \mathbf{R}_{\Omega_F \setminus \Gamma_{F-FM}} & 0 & \mathbf{S}_{\Omega_F} C^{-1} D \\ 0 & \mathbf{R}_{\Omega_M \setminus \Gamma_{M-FM}} & \mathbf{S}_{\Omega_M} \\ (C^{-1}D)^T \mathbf{S}_{\Omega_F}^T & \mathbf{S}_{\Omega_M}^T & (C^{-1}D)^T \mathbf{R}_{\Gamma_{F-FM}} (C^{-1}D) + \mathbf{R}_{\Gamma_{M-FM}} \end{bmatrix} \begin{bmatrix} \mathbf{A}_{a, \Omega_F \setminus \Gamma_{F-FM}} \\ \mathbf{A}_{a, \Omega_M \setminus \Gamma_{M-FM}} \\ \mathbf{A}_{a, \Gamma_{M-FM}} \end{bmatrix} = \begin{bmatrix} \mathbf{M}_{\Omega_F \setminus \Gamma_{F-FM}} \\ \mathbf{M}_{\Omega_M \setminus \Gamma_{M-FM}} \\ (C^{-1}D)^T \mathbf{M}_{\Gamma_{F-FM}} + \mathbf{M}_{\Gamma_{M-FM}} \end{bmatrix} \quad (4.14)$$

Two important points are needed to be observed in eqn.(4.14). First, the sparsity of the block matrix is affected. Secondly, the computation requires to perform inversion of coupling matrix C. In the next section, we are going to explain the different stages of implementing mortar method for 3D problem.

4.2 Implementation of mortar method

In this section we will discuss two important points: first, the integrating domain in the case of 3D and secondly, the numerical calculation of coupling matrices C and D.

4.2.1 Integrating domain

The coupling matrix C depends only on the shape function of the fixed side interface Γ_{f-fm} . Therefore, while calculating coupling matrix C, we will only consider the edges of Γ_{f-fm} as shown in fig.(4.2). When the rotor part of electrical machine moves the interface meshes Γ_{f-fm} and Γ_{m-fm} become non-conformed. Since, we are dealing with the curved surface, in the non conformed scenario the meshes belonging to Γ_{f-fm} penetrates the interface Γ_{m-fm} and vice-versa. The calculation of coupling matrix D becomes difficult. To overcome this challenge a third mesh is created called as mortar mesh see fig.(4.2).

In 3D the meshes on the fixed interface Γ_{f-fm} and the moving interface Γ_{m-fm} are triangular or quadrangular facets. We can construct a mortar mesh by projecting

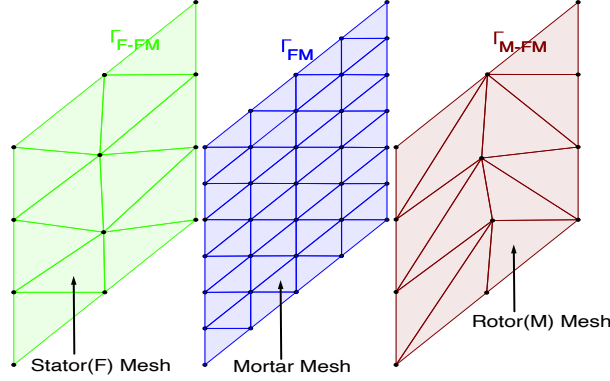
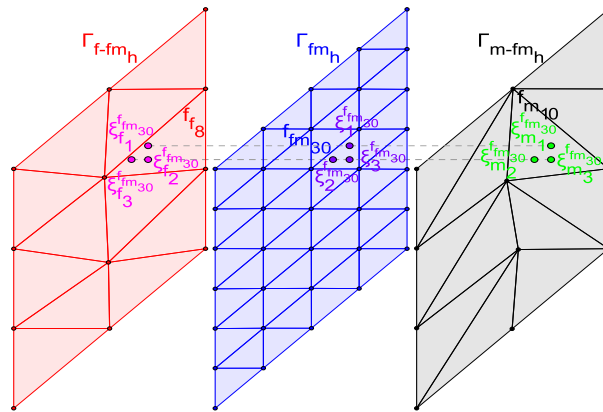


Figure 4.2 – Representation of Mortar Interface.

the meshes of the interfaces Γ_{f-fm} and Γ_{m-fm} on the surface Γ_{fm} and perform the intersection. This process of projection and intersection is easy in the case of quadrangular mesh but in the case of triangle-triangle intersection it becomes complicated. As in this case, we will have polyhedron with maximum of six edges. In this case [14] proposed a simpler approach, where we create an independent mesh. This independent mesh Γ_{fm} needs to be roughly 2 times finer than mesh at the interfaces Γ_{f-fm} and Γ_{m-fm} . However, in the case of curved surface a loss in accuracy was observed. Therefore, we have used a mesh Γ_{fm} which at least four times finer than mesh at the interfaces Γ_{f-fm} and Γ_{m-fm} .

In next section we will discuss about the numerical implementation of calculating coupling matrices C and D.

4.2.2 Computation of coupling matrices


 Figure 4.3 – Projection of Gauss points from Γ_{fm} to Γ_{f-fm} and Γ_{m-fm} .

Lets recall few definition. The mesh belonging to interface Γ_{f-fm} will be denominated as Γ_{f-fm_h} . Similarly for interface Γ_{m-fm} mesh will be denominated as Γ_{m-fm_h} . In 3D to numerically calculate $[c_a(p, j)]$ and $[d_a(p, l)]$ in (4.9) [53]-[14] proposed a method based on Gauss quadrature method. In this sub-section, we will study the calculation of coupling matrices C and D using Gaussian quadrature method.

4.2. IMPLEMENTATION OF MORTAR METHOD

Let $n_{\Gamma_{f-fm}}$, $n_{\Gamma_{m-fm}}$ and $n_{\Gamma_{fm}}$ be the number of face elements of the mesh belongs to Γ_{f-fm} , Γ_{m-fm} and Γ_{fm} respectively.

Let f_{f_q} be a face element belong to fixed interface Γ_{f-fm} , where q is ranging between $[1, n_{\Gamma_{f-fm}}]$. Similarly f_{m_r} be a face element belong to moving interface Γ_{m-fm} , where r is ranging between $[1, n_{\Gamma_{m-fm}}]$.

Let n_{gp_f} be the number of Gauss points for integrating over a face f_i . Let $\omega_g^{f_i}$ and $\xi_g^{f_i}$ be the weights and position of Gauss points respectively for the face element f_i , where i range between $[1, n_F]$ and g ranges between $[1, n_{gp_f}]$.

Projection of Gauss points from mortar mesh (Γ_{fm_h}) to interface meshes Γ_{f-fm_h} and Γ_{m-fm_h}

According to [53]-[14]-[25] $\xi_g^{f_{fms}}$ and $\xi_g^{f_{fms}}$ be the orthogonal projection of Gauss point $\xi_g^{f_{fms}}$ on the meshes \in to interface Γ_{f-fm} and Γ_{m-fm} respectively. Where g and s ranges between $[1, n_{gp_f}]$ and $[1, n_{\Gamma_{fm}}]$. The steps to perform orthogonal projection are described below:-

- First step is to build an operator that perform orthogonal projection of face elements f_{fms} . Each face element $\in \Gamma_{fm}$ is projected on each face elements $\in \Gamma_{f-fm}$ and Γ_{m-fm} .
- Second step is to project each Gauss points $\xi_g^{f_{fms}}$ on the meshes belong to Γ_{f-fm} , here, $g \in [1, n_{gp_f}]$ and $s \in [1, n_{\Gamma_{fm}}]$.
- Third step is to project each Gauss points $\xi_g^{f_{fms}}$ on the meshes belong to Γ_{m-fm} , here, $g \in [1, n_{gp_f}]$ and $s \in [1, n_{\Gamma_{fm}}]$.

To visualize this process, lets see fig.(4.3). The Gauss points $\xi_1^{f_{fms30}}$, $\xi_2^{f_{fms30}}$ and $\xi_3^{f_{fms30}}$ of face element $f_{fms30} \in \Gamma_{fm}$ is orthogonally projected on facet $f_{f8} \in \Gamma_{f-fm}$ and projected Gauss points are named as $\xi_{f1}^{f_{fms30}}$, $\xi_{f2}^{f_{fms30}}$ and $\xi_{f3}^{f_{fms30}}$ belongs to f_{f8} . Similarly, Gauss points $\xi_1^{f_{fms30}}$, $\xi_2^{f_{fms30}}$ and $\xi_3^{f_{fms30}}$ of face element $f_{fms30} \in \Gamma_{fm}$ is orthogonally projected on facet $f_{m1} \in \Gamma_{m-fm}$ and projected Gauss points are named as $\xi_{m1}^{f_{fms30}}$, $\xi_{m2}^{f_{fms30}}$ and $\xi_{m3}^{f_{fms30}}$ belongs to f_{m1} .

Computation of coupling term C and D on edge elements

Using Gauss quadrature formula c_a and d_a in (4.9) can be computed as:

$$\begin{aligned} c_a(p, j) &= \int_{\Gamma_{f-fm}} (\mathbf{w}_{a_{fp}} \times \mathbf{n}) \cdot (\mathbf{w}_{a_{fj}} \times \mathbf{n}) d\Gamma \\ &= \sum_{q=1}^{n_{\Gamma_{f-fm}}} \sum_{g=1}^{n_{gp_f}} (\mathbf{w}_{a_{fp}}(\xi_g^{f_{f_q}}) \times \mathbf{n}_{f_{f_q}}) \cdot (\mathbf{w}_{a_{fj}}(\xi_g^{f_{f_q}}) \times \mathbf{n}_{f_{f_q}}) \omega_g^{f_{f_q}} \end{aligned} \quad (4.15)$$

$$\begin{aligned} d_a(p, l) &= \int_{\Gamma_{FM}} (\mathbf{w}_{a_{fp}} \times \mathbf{n}) \cdot (\mathbf{w}_{a_{ml}} \times \mathbf{n}) d\Gamma \\ &= \sum_{s=1}^{n_{\Gamma_{fm}}} \sum_{g=1}^{n_{gp_f}} (\mathbf{w}_{a_{fp}}(\xi_g^{f_{fms}}) \times \mathbf{n}_{f_{fms}}) \cdot (\mathbf{w}_{a_{ml}}(\xi_g^{f_{fms}}) \times \mathbf{n}_{f_{fms}}) \omega_g^{f_{fms}} \end{aligned} \quad (4.16)$$

Here $\mathbf{n}_{f_{fq}}$ and $\mathbf{n}_{f_{fms}}$ be the outward normal to each surface element belonging to interface Γ_{f-fm} and Γ_{fm} respectively. $\xi_g^{f_{fq}}$ be the local coordinates of respective Gauss points and $\omega_g^{f_{fq}}$ be its weights for each surface element belong to interface Γ_{f-fm} . $\xi_g^{f_{fms}}$ be the local coordinates of respective Gauss points and $\omega_g^{f_{fms}}$ be its weights for each surface element belong to interface Γ_{fm} .

4.2.3 Inversion of coupling matrix C

By taking edge shape function definition into account, the coupling matrix C has the band size of $2N(n_a+1)$, where

- N = order of basis function.
- n_a = it is the total number of edges belong to elements, that shares edge of interest (but excluded from n_a).

In our case we will be utilizing the first order edge shape function. Therefore, in our case $N = 1$. Since, the coupling matrix C is made up edges of mesh element belong to interface Γ_{f-fm} , in 3D the domain Ω_f is meshed with either hexahedron or tetrahedron. Therefore, generating two scenarios.

Lets discuss two scenario of coupling matrix C bandwidth:-

1. The domain is meshed using hexahedron mesh element.
2. The domain is meshed using tetrahedron mesh element.

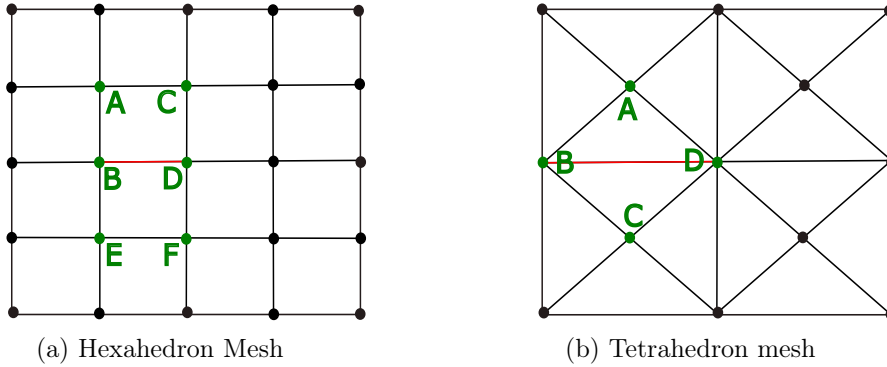


Figure 4.4 – Depiction of surface mesh along interface Γ_{f-fm} based on domain Ω_f meshed with hexahedron or tetrahedron volume element.

Scenario 1 (Hexahedron mesh)

Lets consider domain Ω_f is composed of only hexahedron mesh element in 3D. Then at the interface Γ_{f-fm} the surface element will comprised of quadrangular elements as shown in fig.(4.4a). In this scenario each edge belonging to surface element Γ_{f-fm} is shared by two surface element. For example from fig.(4.4a) edge BD shown in color red is shared by surface elements ABDC and BDEF, In this example $n_a = (\text{edge}_{AB}, \text{edge}_{CA}, \text{edge}_{DC}, \text{edge}_{DF}, \text{edge}_{FE}, \text{edge}_{EB}) = 6$.

So in 3D with hexahedron mesh and first order edge shape function the bandwidth of coupling matrix C will be of size 14.

4.3. CONCLUSION

Scenario 2 (Tetrahedron mesh)

Lets consider domain Ω_f is composed of only tetrahedron mesh element in 3D. Then at the interface Γ_{f-fm} the surface element will comprised of triangular elements as shown in fig.(4.4b). In this scenario each edge belonging to surface element Γ_{f-fm} is shared by two surface element. For example from fig.(4.4b) edge BD shown in color red is shared by surface elements ABD and BCD, In this example $n_a = (\text{edge}_{AB}, \text{edge}_{DA}, \text{edge}_{BC}, \text{edge}_{CD}) = 4$.

So in 3D with tetrahedron mesh and first order edge shape function the bandwidth of coupling matrix C will be of size 10.

Finally, In 3D the coupling matrix C is of bandwidth 14 and 10 for hexahedron and tetrahedron element respectively. The matrix C can be easily inverted using direct solver MUMPS see [3].

4.3 Conclusion

In this chapter, we studied mortar method. The method impose continuity along the sliding interface Γ_{fm} with the help of Lagrange type multiplier. Numerically, we have described how the unknowns $\mathbf{A}_{\Gamma_{f-fm}}$ belongs to fixed side interface Γ_{fm} are expressed as a function of unknowns $\mathbf{A}_{\Gamma_{m-fm}}$ belongs to moving side interface Γ_{m-fm} using coupling matrices C and D.

To express unknowns $\mathbf{A}_{\Gamma_{f-fm}}$ as a function of unknowns $\mathbf{A}_{\Gamma_{m-fm}}$, it is require to define the integrating domain using coupling matrices C and D see eqn.(4.9). The coupling matrix C is computed over the edges belongs to mesh of interface Γ_{f-fm} . A third mesh is necessary to construct for computing matrix D. Since, we are dealing with curved surfaces, for 3D scenario a general independent mesh 4 times finer than mesh belongs to Γ_{f-fm} and Γ_{m-fm} is created see fig.(4.2). Next, we have shown the calculation of edge based coefficient c_a and d_a belongs to coupling matrices C and D respectively. There are several methods to calculate these edge based coefficient in our case we have utilized 2D Gauss quadrature formula see eqn.(4.15 - 4.16). Finally, In the end coupling matrix C is inverted using direct solver MUMPS.

In the next chapter, we will study another method based on sliding interface known as interpolation. In this chapter we will be discussing the principle of interpolation, computation of interpolating coefficient and linear combination.

Chapter 5

Interpolation Method

Contents

5.1	Introduction to interpolation method	53
5.2	Nodal interpolation method	54
5.2.1	Principle	54
5.2.2	Computation of the interpolation coefficient	56
5.3	Edge interpolation method	57
5.3.1	Extending the idea to first order incomplete edge finite element framework	57
5.3.2	Computation of the interpolation coefficient	58
5.4	Performing Linear combination	59
5.5	Conclusion	61

5.1 Introduction to interpolation method

As already discussed in chapter 4, the movement generates a non - conforming mesh at the interfaces between the fixed part mesh Γ_{f-fm_h} and the moving part mesh Γ_{m-fm_h} . Therefore, the nodes, edges and surface of the mesh elements are no longer coincident at the interface Γ_{fm} . To connect the two meshes and, therefore, unknowns, we resort to an interpolation technique.

The interpolation technique can be performed for different types of quantities approximated on the nodes, edges and face of an element. The interpolation is easily applicable on quantities approximated on the elements' nodes and edges but becomes difficult to develop for quantities approximated on face elements see [26]. Also, in the case of tetrahedral mesh to perform interpolation by face element, we need to create an integrating mesh formed by intersecting meshes belonging to Γ_{f-fm_h} and Γ_{m-fm_h} over each other. The implementation of integrating mesh on the curved surface is complex.

The method was originally proposed by [46] for the unknowns approximated on mesh elements' nodes. It was then extended to second order polynomial interpolation by [60]. In this chapter, we propose two strategies to connect unknowns belonging to non conformed interface in the case of magnetic vector potential \mathbf{A} approximated on the edges of the mesh elements. The strategies are:

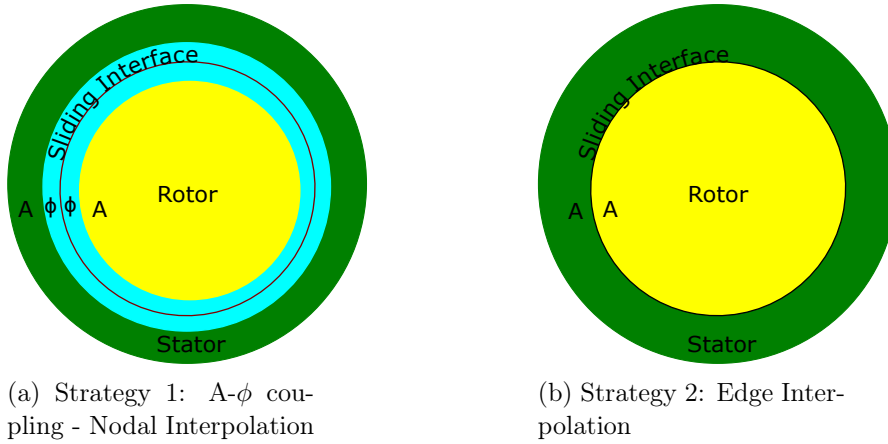


Figure 5.1 – 2D representation of Interpolation strategy based on nodal elements and edge elements.

1. The magnetic non conducting materials is approximated using magnetic vector potential \mathbf{A} formulation and region with air is approximated with magnetic scalar potential ϕ formulation (\mathbf{A} - ϕ coupling) and nodal interpolation is performed in the air region between Γ_{f-fm} and Γ_{m-fm} .
2. Both magnetic non conducting and air regions are approximated using magnetic vector potential \mathbf{A} formulation and interpolation is performed between edge elements belongs to interfaces Γ_{f-fm} and Γ_{m-fm} .

5.2 Nodal interpolation method

An illustration of the interpolation method is presented for 2D case in fig.(5.2 - 5.3). Fig.(5.2) represents the initial mesh position along the interface Γ_{fm} of mobile part and fixed part, each node N_{f_i} is coincidental with each node N_{m_i} , where i varies between $1 \leq i \leq 6$. Fig.(5.3) represents the mesh after a movement step. In this case along interface Γ_{fm} each node N_{f_i} is not coincidental with each node N_{m_i} , where i varies between $1 \leq i \leq 6$.

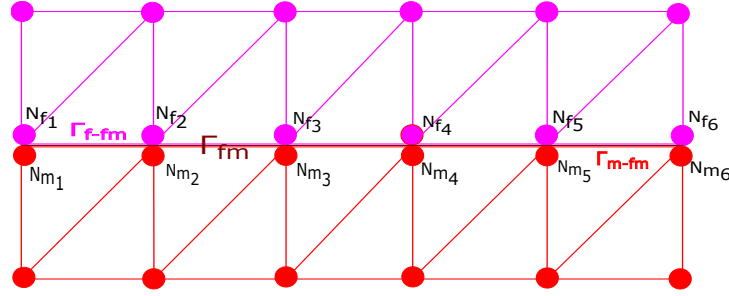


Figure 5.2 – Mesh position at initial state.

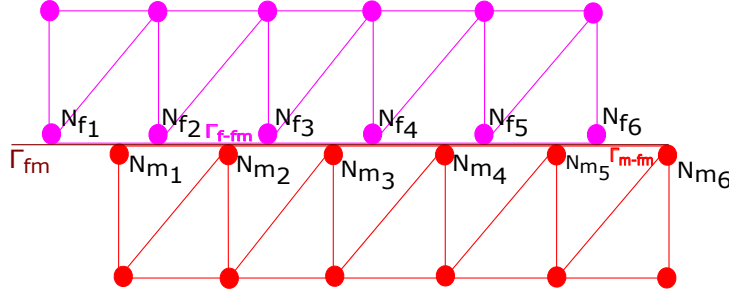


Figure 5.3 – Mesh position after movement

In the next sub-section, we will now describe the approach to impose continuity under the scenario shown in fig.(5.3) based on 2D nodal interpolation.

5.2.1 Principle

In this case the nodal unknowns are magnetic scalar potentials and denoted as $\phi_{n_{f_i}}$ and $\phi_{n_{m_j}}$ for the fixed (Γ_{f-fm}) and mobile (Γ_{m-fm}) sides respectively.

Lets assume the nodal unknowns belongs to Γ_{m-fm} side are expressed as linear combination of nodal unknowns belongs to Γ_{f-fm} side. The expression is written as:

$$\phi_{n_{m_j}} = \sum_{i=1}^{n_{\Gamma_{f-fm}}} \alpha_i \phi_{n_{f_i}} \quad (5.1)$$

where,

- $\phi_{n_{m_j}}$ is the nodal unknown associated to nodes belonging to the mobile side (Γ_{m-fm}) of the interface.
- $\phi_{n_{f_i}}$ is the nodal unknown associated to nodes belonging to the fixed side (Γ_{f-fm}) of the interface.
- α_i is the interpolation coefficient.
- $n_{\Gamma_{f-fm}}$ is the total number of nodes belonging to the fixed side (Γ_{f-fm}) of the interface.

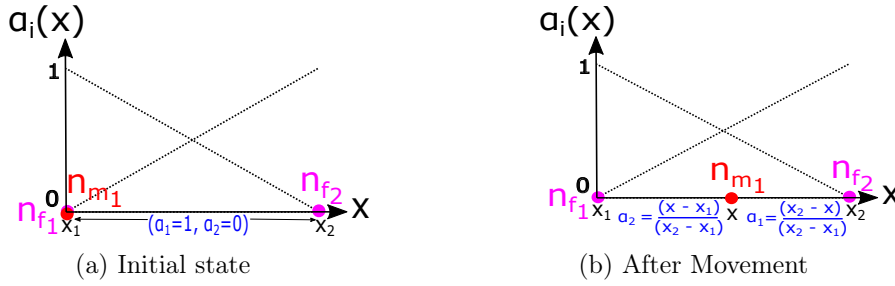


Figure 5.4 – 1D projection of node n_{m_1} belongs to interface Γ_{m-fm} on interface Γ_{f-fm} .

Using (5.1) we can express nodal unknown $\phi_{n_{m_1}}$ based on node n_{m_1} represented in fig.(5.2) and fig.(5.3) as a combination of nodal unknown $\phi_{n_{f_1}}$ and $\phi_{n_{f_2}}$ based on nodes n_{f_1} and n_{f_2} belongs to fixed side (Γ_{f-fm}) of interface :

$$\phi_{n_{m_1}} = \alpha_1 \phi_{n_{f_1}} + \alpha_2 \phi_{n_{f_2}}. \quad (5.2)$$

To calculate interpolating coefficients α_1 and α_2 , node n_{m_1} is projected on edge contains nodes n_{f_1} and n_{f_2} . Let the 1D coordinate of projected node n_{m_1} be x as shown in fig.(5.4). After the projection, using 1D FEM we calculate the 1D shape function for the nodes n_{f_1} and n_{f_2} at the coordinate x . The following conclusion are drawn for interpolating coefficient:

- $\alpha_1 + \alpha_2 = 1$
- In the initial state see fig.(5.4a) the node $\phi_{n_{m_1}}$ is coincidental with node $\phi_{n_{f_1}}$. For this scenario $\alpha_1 = 1$ and $\alpha_2 = 0$.
- In the state after a movement see fig.(5.4b) the projection of node $\phi_{n_{m_1}}$ is somewhere between nodes $\phi_{n_{f_1}}$ and $\phi_{n_{f_2}}$. For this scenario $\alpha_1 = \alpha$ and $\alpha_2 = 1 - \alpha$, where, α ranges between $[0, 1]$.

In the next sub-section, we will extend this idea to 3D problem. Where, we will have surface mesh along the interface Γ_{fm} sliding over each other.

5.2. NODAL INTERPOLATION METHOD

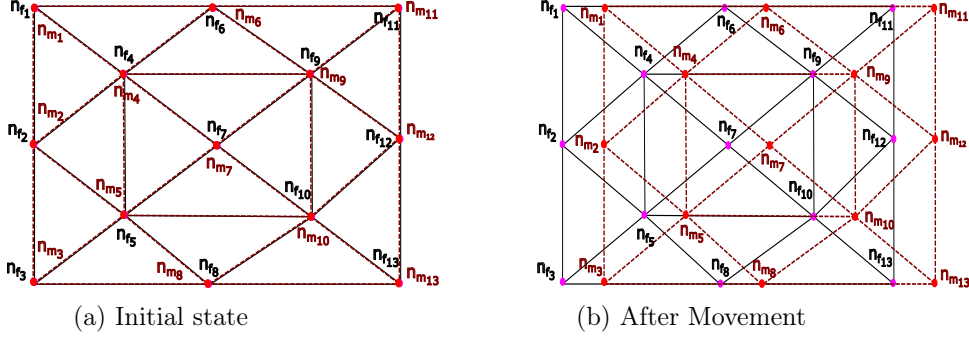


Figure 5.5 – Initial and after a step movement positioning of mesh element belongs to interfaces Γ_{m-fm} and Γ_{f-fm} .

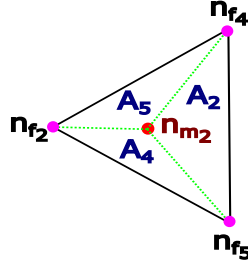


Figure 5.6 – 2D projection of node n_{m1} belongs to interface Γ_{m-fm} on interface Γ_{f-fm} .

5.2.2 Computation of the interpolation coefficient

In the case of conformed mesh as shown in fig.(5.5a), the nodes belongs to the moving side are exactly coincidental with nodes belonging to the fixed side. However, after movement the nodes n_{m_i} belonging to the moving side of sliding interface are no longer coincidental with nodes n_{f_i} from the fixed side interface as shown in fig.(5.5b). Here 'i' is ranging between 1 to 13. In this case to impose the continuity, the nodal unknowns ϕ_{m_i} are approximated as a function of nodal unknowns ϕ_{f_i} on nodes n_{f_i} .

Lets approximate nodal unknown ϕ_{m_2} belongs to node n_{m_2} . To do that first we need to project node n_{m_2} belongs to surface Γ_{m-fm} on surface Γ_{f-fm} and search on which face element node n_{m_2} has been projected. In our case as shown in fig.(5.6) node n_{m_2} is projected on face element composed of nodes n_{f_2} , n_{f_4} and n_{f_5} . Secondly, we approximate ϕ_{m_2} as a function of nodal unknowns ϕ_{f_2} , ϕ_{f_4} and ϕ_{f_5} on nodes n_{f_2} , n_{f_4} and n_{f_5} respectively.

We assume 'A' be the area of triangle composed of nodes n_{f_2} , n_{f_4} and n_{f_5} , 'A₅' be the area of triangle composed of nodes n_{f_2} , n_{f_4} and the projection of node n_{m_2} . Similarly this definition is extended for area 'A₂' and 'A₅'. Then $\phi_{n_{m_2}}$ is approximated as:

$$\phi_{n_{m_2}} = \alpha_2 \phi_{n_{f_2}} + \alpha_4 \phi_{n_{f_4}} + \alpha_5 \phi_{n_{f_5}} \quad (5.3)$$

In 2D case following conclusion are drawn,

- $\alpha_2 + \alpha_4 + \alpha_5 = 1$

- In the initial state see fig.(5.5a) the node $\phi_{n_{m_2}}$ is coincidental with node $\phi_{n_{f_2}}$. For this scenario $\alpha_2 = 1$, α_4 and α_5 are equal to 0.
- In the state after a movement see fig.(5.5b) and fig.(5.6) the projection of node $\phi_{n_{m_1}}$ is inside the triangle composed of nodes n_{f_2} , n_{f_4} and n_{f_5} . Using first order 2D nodal shape function principle. For this scenario $\alpha_1 = \frac{A_1}{A}$, $\alpha_2 = \frac{A_4}{A}$ and $\alpha_3 = \frac{A_5}{A}$, where α_2 , α_4 and α_5 ranges between $[0, 1]$. In the case of second order nodal finite elements, Lagrange polynomials are used to calculate interpolation coefficient.

5.3 Edge interpolation method

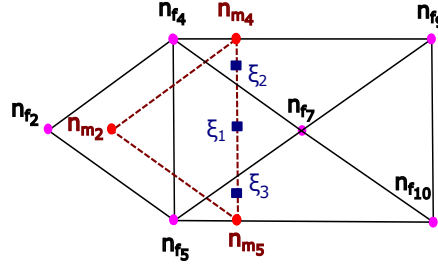


Figure 5.7 – 2D projection of face element f_{m1} belongs to interface Γ_{m-fm} on interface Γ_{f-fm} .

A generalized approach is proposed here refer as "Continuous type" which can be applied to non conforming tetrahedral meshes. The approach is an extension of [45]-[66].

5.3.1 Extending the idea to first order incomplete edge finite element framework

Let \mathbf{A} be the magnetic vector potential unknown approximated on surface element. Let $A_{a_{m_{ij}}}$ be an unknown approximated over edge $a_{m_{ij}}$ belonging to the interface Γ_{m-fm} and $\mathbf{w}_{a_{m_{ij}}}$ be its edge shape function. Let us assume $n_{A_{\Gamma_{f-fm}}}$ and $n_{A_{\Gamma_{m-fm}}}$ be the total number of edges on the interfaces belongs to fixed side and moving side respectively. Using (2.28), we approximate magnetic vector potential unknown \mathbf{A} on surface element belongs to interface Γ_{m-fm} as:

$$\mathbf{A} = \sum_{ij=1}^{n_{A_{\Gamma_{m-fm}}}} A_{a_{m_{ij}}} \mathbf{w}_{a_{m_{ij}}} \quad (5.4)$$

Let \mathbf{e}_{ij} be a unit vector for an arbitrary edge \mathbf{a}_{ij} define as:

$$\mathbf{e}_{ij} = \frac{\mathbf{a}_{ij}}{\|\mathbf{a}_{ij}\|}, \quad (5.5)$$

$$\mathbf{e}_{ij} = \frac{1}{l_{a_{ij}}} \int_{l_{a_{ij}}} d\mathbf{l}. \quad (5.6)$$

5.3. EDGE INTERPOLATION METHOD

Here $l_{a_{ij}}$ is the length of an edge \mathbf{a}_{ij} .

\mathbf{A}_m and \mathbf{A}_f are the magnetic vector potential belonging to elements of moving side and fixed side respectively. Using (5.4), (5.5) and (5.6) we can approximate unknown $A_{a_{m45}}$ imposed on edge \mathbf{a}_{m45} belonging to Γ_{m-fm} as shown in fig.(5.7) as:

$$\begin{aligned}
 A_{a_{m45}} &= \mathbf{A}_m \cdot \mathbf{e}_{m45} \\
 &= \frac{1}{l_{a_{m45}}} \int_{l_{a_{m45}}} \mathbf{A}_m \cdot d\mathbf{l} = \frac{1}{l_{a_{m45}}} \int_{l_{a_{m45}}} \mathbf{A}_f \cdot d\mathbf{l} \\
 &= \sum_{lm=1}^{n_{A\Gamma_{f-fm}}} A_{a_{f_{lm}}} \left(\frac{1}{l_{a_{m45}}} \int_{l_{a_{m45}}} \mathbf{w}_{a_{f_{lm}}} \cdot d\mathbf{l} \right) \\
 &= \sum_{lm=1}^{n_{A\Gamma_{f-fm}}} A_{a_{f_{lm}}} \alpha_{a_{f_{lm}}} \quad (5.7)
 \end{aligned}$$

Here $\alpha_{a_{f_{lm}}}$ is an interpolation coefficient calculated using 1D Gauss quadrature integration.

5.3.2 Computation of the interpolation coefficient

Here we will show the computation of interpolation coefficient $\alpha_{a_{f_{lm}}}$ using Gauss quadrature for edge a_{m45} belonging to the interface Γ_{m-fm} as shown in fig.(5.7). Under generalized case, i.e., for any number of Gauss points eqn.(5.7) can be written as:

$$A_{a_{m45}} = \frac{l_{a_{m45}}}{2} \sum_{lm=1}^{n_{A\Gamma_{f-fm}}} A_{a_{f_{lm}}} \int_{-1}^1 \mathbf{w}_{a_{f_{lm}}}(\xi) \cdot \mathbf{e}_{m45} d\xi \quad (5.8)$$

where,

$$\alpha_{a_{f_{lm}}} = \frac{l_{a_{m45}}}{2} \int_{-1}^1 \mathbf{w}_{a_{f_{lm}}}(\xi) \cdot \mathbf{e}_{m45} d\xi \quad (5.9)$$

ξ is 1-D local coordinate. Now the integration part shown in (5.9) is calculated using Gauss quadrature as mentioned earlier. Depending on the number of Gauss points used for the integration of (5.9), two types of interpolation methods can be distinguished:

- Continuous type:- Gauss quadrature is computed using two or more number of Gauss points. Under this we take into account edges $a_{f_{74}}$, $a_{f_{45}}$, $a_{f_{57}}$, $a_{f_{49}}$, $a_{f_{97}}$, $a_{f_{710}}$ and $a_{f_{105}}$ of fixed side for replacing the edge unknown for edge a_{m45} of moving side see fig.(5.7).
- Discontinuous type:- Gauss quadrature is computed using just one Gauss point. Under this we just take into account edges $a_{f_{74}}$, $a_{f_{45}}$ and $a_{f_{57}}$ of fixed side for replacing the edge unknown for edge a_{m45} of moving side see fig.(5.7).

Continuous type:-

Let ξ_1, ξ_2 and ξ_3 be the orthogonal projection of 1D Gauss points on surface element belonging to Γ_{f-fm} . The projection is made from edge $\mathbf{a}_{m_{45}}$ of interface Γ_{m-fm} . The corresponding weights can be named as ω_1, ω_2 and ω_3 . Now by applying three Gauss point quadrature integration (5.9) can be computed as:

$$\begin{aligned}
 A_{a_{m_{45}}} &= \frac{l_{a_{m_{45}}}}{2} \left[A_{a_{f_{74}}} \left[\left(\mathbf{w}_{a_{f_{74}}}(\xi_1) \cdot \mathbf{e}_{m_{45}} \right) (\omega_1) + \left(\mathbf{w}_{a_{f_{74}}}(\xi_2) \cdot \mathbf{e}_{m_{45}} \right) (\omega_2) \right] \right. \\
 &+ A_{a_{f_{57}}} \left[\left(\mathbf{w}_{a_{f_{57}}}(\xi_1) \cdot \mathbf{e}_{m_{45}} \right) (\omega_1) + \left(\mathbf{w}_{a_{f_{57}}}(\xi_3) \cdot \mathbf{e}_{m_{45}} \right) (\omega_3) \right] \\
 &+ A_{a_{f_{45}}} \left[\left(\mathbf{w}_{a_{f_{45}}}(\xi_1) \cdot \mathbf{e}_{m_{45}} \right) (\omega_1) \right] + A_{a_{f_{710}}} \left[\left(\mathbf{w}_{a_{f_{710}}}(\xi_3) \cdot \mathbf{e}_{m_{45}} \right) (\omega_3) \right] \\
 &+ A_{a_{f_{105}}} \left[\left(\mathbf{w}_{a_{f_{105}}}(\xi_3) \cdot \mathbf{e}_{m_{45}} \right) (\omega_3) \right] + A_{a_{f_{49}}} \left[\left(\mathbf{w}_{a_{f_{49}}}(\xi_2) \cdot \mathbf{e}_{m_{45}} \right) (\omega_2) \right] \\
 &\left. + A_{a_{f_{97}}} \left[\left(\mathbf{w}_{a_{f_{97}}}(\xi_2) \cdot \mathbf{e}_{m_{45}} \right) (\omega_2) \right] \right] \quad (5.10)
 \end{aligned}$$

Discontinuous type:-

Let ξ_1 be the orthogonal projection of 1D Gauss points on surface element belonging to Γ_{f-fm} . The projection is made from edge $\mathbf{a}_{m_{45}}$ of interface Γ_{m-fm} . The corresponding weights can be named as ω_1 . Now by applying one Gauss point quadrature integration (5.9) can be computed as:

$$\begin{aligned}
 A_{a_{m_{45}}} &= \frac{l_{a_{m_{45}}}}{2} \left[A_{a_{f_{74}}} \left(\mathbf{w}_{a_{f_{74}}}(\xi_1) \cdot \mathbf{e}_{m_{45}} \right) (\omega_1) + A_{a_{f_{45}}} \left(\mathbf{w}_{a_{f_{45}}}(\xi_1) \cdot \mathbf{e}_{m_{45}} \right) (\omega_1) \right. \\
 &\left. + A_{a_{f_{57}}} \left(\mathbf{w}_{a_{f_{57}}}(\xi_1) \cdot \mathbf{e}_{m_{45}} \right) (\omega_1) \right] \quad (5.11)
 \end{aligned}$$

General type (for "n" number of Gauss points):-

For "n", any number of Gauss points, where "n" can be equal to 1 or greater than one, (5.10) and (5.11) are reformulated as:

$$A_{a_{m_{45}}} = \frac{l_{a_{m_{45}}}}{2} \left[\sum_{lm=1}^{n_{A_{\Gamma_{f-fm}}}} A_{a_{f_{lm}}} \sum_{k=i}^j \left[\left(\mathbf{w}_{a_{f_{lm}}}(\xi_k) \cdot \mathbf{e}_{m_{45}} \right) (\omega_k) \right] \right] \quad (5.12)$$

Here " $\sum_{lm=1}^{n_{A_{\Gamma_{f-fm}}}}$ " represents the summation of edges " $a_{f_{lm}}$ " belonging to interface Γ_{f-fm} . " $\sum_{k=i}^j$ " represents the summation of Gauss points with respect to each $a_{f_{lm}}$.

To compute interpolation coefficients under continuous type rectangular integration can also be used.

5.4 Performing Linear combination

To show linear combination, we will be using the element belong to the moving side composed of nodes n_{m_2}, n_{m_4} and n_{m_5} as shown in fig.(5.7). For simplicity and better understanding, we make some assumptions in notation representation.

5.4. PERFORMING LINEAR COMBINATION

- $A_{a_{m_{45}}} = A_{m_2}$, $A_{a_{m_{52}}} = A_{m_4}$, $A_{a_{m_{24}}} = A_{m_5}$.

Now, lets perform the linear combination for edge unknown ' A_{m_2} ' for discontinuous type interpolation. Let the system of equation for face element composed of edges A_{m_2} , A_{m_4} and A_{m_5} is expressed as:

$$\begin{bmatrix} \vdots & \vdots & \vdots \\ \vdots & \begin{pmatrix} R_{22} & R_{24} & R_{25} \\ R_{42} & R_{44} & R_{45} \\ R_{52} & R_{54} & R_{55} \end{pmatrix} & \vdots \\ \vdots & \vdots & \vdots \end{bmatrix} \begin{bmatrix} \vdots \\ \begin{pmatrix} A_{m_2} \\ A_{m_4} \\ A_{m_5} \end{pmatrix} \\ \vdots \end{bmatrix} = \begin{bmatrix} \vdots \\ \begin{pmatrix} M_2 \\ M_4 \\ M_5 \end{pmatrix} \\ \vdots \end{bmatrix} \quad (5.13)$$

Here ' R_{ij} ' and ' M_i ' in eqn.(5.13) represents the stiffness matrix and the source vector to the corresponding face element. Only the entries related to one face element is shown for simplicity and better understanding.

Using eqn.(5.11) A_{m_2} is replaced by $A_{a_{f_{74}}}$, $A_{a_{f_{45}}}$ and $A_{a_{f_{57}}}$. Now, the transformation relationship is expressed as:

$$\begin{bmatrix} A_{m_2} \\ A_{m_4} \\ A_{m_5} \end{bmatrix} = \begin{bmatrix} \alpha_{a_{f_{74}}} & \alpha_{a_{f_{45}}} & \alpha_{a_{f_{57}}} & 0 & 0 \\ 0 & 0 & 0 & 1 & 0 \\ 0 & 0 & 0 & 0 & 1 \end{bmatrix} \begin{bmatrix} A_{a_{f_{74}}} \\ A_{a_{f_{45}}} \\ A_{a_{f_{57}}} \\ \phi_{m_4} \\ \phi_{m_5} \end{bmatrix} \quad (5.14)$$

$$= |\alpha| \begin{bmatrix} A_{a_{f_{74}}} \\ A_{a_{f_{45}}} \\ A_{a_{f_{57}}} \\ A_{m_4} \\ A_{m_5} \end{bmatrix} \quad (5.15)$$

here $|\alpha|$ is the transformation matrix. Substituting eqn.(5.14) in eqn.(5.13). In order to respect the property of Galerkin method, we multiply the matrix representing face element by $|\alpha|^T$ as well. Which leads to following relation:

$$\begin{bmatrix} \vdots & \vdots & \vdots \\ \vdots & |\alpha|^T \begin{pmatrix} R_{22} & R_{24} & R_{25} \\ R_{42} & R_{44} & R_{45} \\ R_{52} & R_{54} & R_{55} \end{pmatrix} |\alpha| & \vdots \\ \vdots & \vdots & \vdots \end{bmatrix} \begin{bmatrix} \vdots \\ \begin{pmatrix} A_{m_2} \\ A_{m_4} \\ A_{m_5} \end{pmatrix} \\ \vdots \end{bmatrix} = \begin{bmatrix} \vdots \\ |\alpha|^T \begin{pmatrix} M_2 \\ M_4 \\ M_5 \end{pmatrix} \\ \vdots \end{bmatrix} \quad (5.16)$$

The eqn.(5.16) can be further expanded as:

$$\begin{bmatrix} \vdots & & \vdots & & \vdots \\ \vdots & \begin{pmatrix} \alpha_{af_{74}} & 0 & 0 \\ \alpha_{af_{45}} & 0 & 0 \\ \alpha_{af_{57}} & 0 & 0 \\ 0 & 1 & 0 \\ 0 & 0 & 1 \end{pmatrix} & \begin{pmatrix} R_{22} & R_{24} & R_{25} \\ R_{42} & R_{44} & R_{45} \\ R_{52} & R_{54} & R_{55} \end{pmatrix} & \begin{pmatrix} \alpha_{af_{74}} & \alpha_{af_{45}} & \alpha_{af_{57}} & 0 & 0 \\ 0 & 0 & 0 & 1 & 0 \\ 0 & 0 & 0 & 0 & 1 \end{pmatrix} & \vdots \\ \vdots & & \vdots & & \vdots \end{bmatrix} = \begin{bmatrix} \vdots \\ \begin{pmatrix} A_{af_{74}} \\ A_{af_{45}} \\ A_{af_{57}} \\ A_{m_4} \\ A_{m_5} \end{pmatrix} \\ \vdots \end{bmatrix} = \begin{bmatrix} \vdots \\ \begin{pmatrix} \alpha_{af_{74}} & 0 & 0 \\ \alpha_{af_{45}} & 0 & 0 \\ \alpha_{af_{57}} & 0 & 0 \\ 0 & 1 & 0 \\ 0 & 0 & 1 \end{pmatrix} \begin{pmatrix} M_2 \\ M_4 \\ M_5 \end{pmatrix} \\ \vdots \end{bmatrix} \quad (5.17)$$

$$\begin{bmatrix} \vdots & & \vdots & & \vdots \\ \vdots & \begin{pmatrix} \alpha_{af_{74}} R_{22} \alpha_{af_{74}} & \alpha_{af_{74}} R_{22} \alpha_{af_{45}} & \alpha_{af_{74}} R_{22} \alpha_{af_{57}} & \alpha_{af_{74}} R_{24} & \alpha_{af_{74}} R_{25} \\ \alpha_{af_{45}} R_{22} \alpha_{af_{74}} & \alpha_{af_{45}} R_{22} \alpha_{af_{45}} & \alpha_{af_{45}} R_{22} \alpha_{af_{57}} & \alpha_{af_{45}} R_{24} & \alpha_{af_{45}} R_{25} \\ \alpha_{af_{57}} R_{22} \alpha_{af_{74}} & \alpha_{af_{57}} R_{22} \alpha_{af_{45}} & \alpha_{af_{57}} R_{22} \alpha_{af_{57}} & \alpha_{af_{57}} R_{24} & \alpha_{af_{57}} R_{25} \\ \alpha_{af_{74}} R_{42} & \alpha_{af_{45}} R_{42} & \alpha_{af_{57}} R_{42} & R_{44} & R_{45} \\ \alpha_{af_{74}} R_{52} & \alpha_{af_{45}} R_{52} & \alpha_{af_{57}} R_{52} & R_{54} & R_{55} \end{pmatrix} & \vdots \\ \vdots & & \vdots & & \vdots \end{bmatrix} = \begin{bmatrix} \vdots \\ \begin{pmatrix} A_{af_{74}} \\ A_{af_{45}} \\ A_{af_{57}} \\ A_{m_4} \\ A_{m_5} \end{pmatrix} \\ \vdots \end{bmatrix} = \begin{bmatrix} \vdots \\ \begin{pmatrix} \alpha_{af_{74}} M_2 \\ \alpha_{af_{45}} M_2 \\ \alpha_{af_{57}} M_2 \\ M_4 \\ M_5 \end{pmatrix} \\ \vdots \end{bmatrix} \quad (5.18)$$

From eqn.(5.18) it becomes evident that symmetry of matrix representing system of equation is retained. Although, the band width of matrix gets increased but the number unknowns in the global system remains unchanged.

5.5 Conclusion

In this chapter, we have studied interpolation method. The method imposed continuity along the sliding interface by approximating unknowns belonging to the interface Γ_{m-fm} as a function of unknowns belonging to the interface Γ_{f-fm} .

To execute interpolation with magnetic vector potential formulation, we proposed two strategies. The first strategy was to implement \mathbf{A} - ϕ coupling and then perform nodal interpolation in air region by approximating air region with magnetic

5.5. CONCLUSION

scalar formulation. The second strategy was to carry out direct interpolation on edge elements. In the validation and results part, we would be testing the second strategy because the first strategy is bit complicated from user perspective.

To express unknowns belonging to moving interface Γ_{m-fm} as a function of unknowns belonging to interface Γ_{f-fm} , computation of interpolation coefficient is required. We have provided an explanation for computing interpolation coefficient in the case of nodal elements as well as edge elements. In section (5.4) we have provided in depth explanation regarding linear combination. While carrying out the linear combination, we have also shown the symmetry of matrix system is retained.

In the next part, we will validate interpolation and mortar methods on academic test case to compare the methods on the basis of accuracy, robustness and performance.

Part III

Validation and Results

Chapter 6

Magneto-static 3D academic test case

Contents

6.1	Description of magneto-static 3D academic test case . .	67
6.1.1	Mesh Scenarios	67
6.1.2	Error Computation	68
6.1.3	Intermediate mortar mesh	68
6.2	Validation and results	69
6.2.1	Isovalues of magnetic flux density	69
6.2.2	Convergence Analysis (Accuracy)	70
6.2.3	Performance	71
6.3	Robustness analysis based on mesh regularity	72
6.4	Validation and results of source terms computed on reduced domain under the application of movement (Non - Meshed coils)	73
6.4.1	Isovalues of magnetic flux density	73
6.4.2	Magnetic Energy	74
6.4.3	Magnetic Flux	75
6.5	Conclusions	75

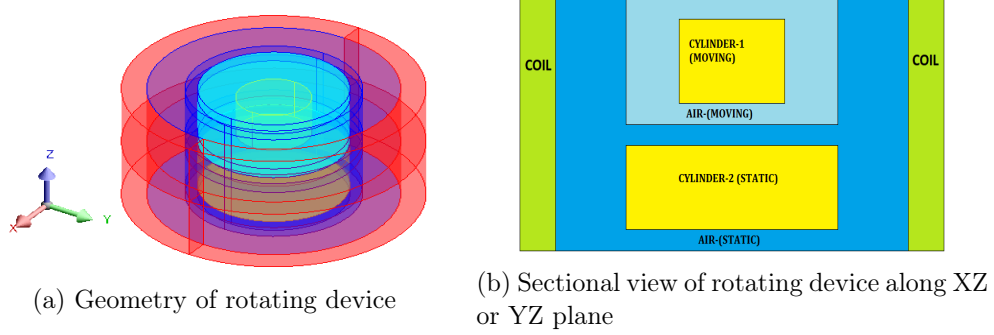


Figure 6.1 – Detail representation of a 3D rotating machine

6.1 Description of magneto-static 3D academic test case

We consider an academic test case symmetrical around Z-axis. As shown in fig.(6.1), the test case is built using two cylinders surrounded by a cylindrical coil conductor. The moving cylinder is built at the top of a static cylinder separated by a thin air-gap of thickness 1 unit. The diameter of the moving cylinder is 3 units and of the static cylinder is 6 units. The thickness of the coil conductor is 1 unit. The difference in the radius between the coil conductor and the static cylinder is 2 units and 3.5 units with the moving cylinder. The total height of the coil conductor is 6 units. The test case is designed so that the computed field value should remain constant at each step.

The physical property of both cylinders is linear isotropic with a relative magnetic permeability (μ_r) of 2000. The number of turns in the coil winding applied to the coil conductor is 350. The source current applied in the coil is 5 A.

6.1.1 Mesh Scenarios

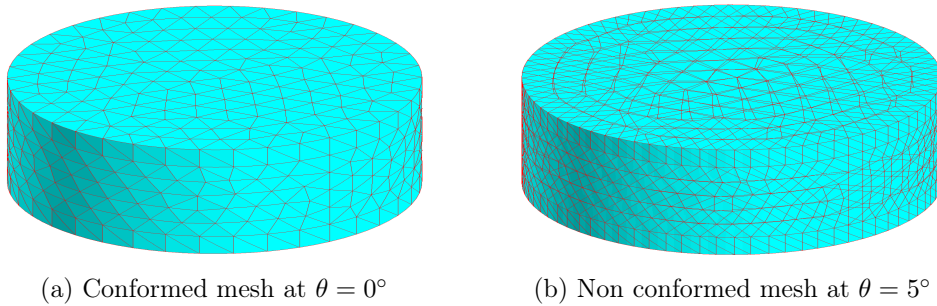


Figure 6.2 – 3D view of conforming and non conforming mesh around sliding interface

6.1. DESCRIPTION OF MAGNETO-STATIC 3D ACADEMIC TEST CASE

Table 6.1 – Mesh scenarios selection.

Mesh Scenario	Degrees of freedom	Mesh around sliding surface (Approx. length of an edge)
1	87,000	0.6 mm
2	129,000	0.5 mm
3	204,757	0.4 mm
4	591,710	0.2 mm

The surface mesh around sliding surface under conformed mesh and non conformed mesh are depicted in fig.(6.2a) and fig.(6.2b) respectively. In this chapter, we are going to test the mortar method and the edge interpolation on four different uniform mesh scenarios, as detailed in table.6.1. The size of an edge belonging to the triangular element around the sliding surface decreases from mesh scenario 1 to mesh scenario 4, as shown in the third column of table.6.1.

6.1.2 Error Computation

$$Error(\epsilon) = \frac{\|u_{approach} - u_{reference}\|_2}{\|u_{reference}\|_2} \times 100 \quad (6.1)$$

In order to quantify the difference between the results of the different meshes and methods, we can calculate the L2-norm of the error. Here "u" represents the quantity such as magnetic energy or flux, $\|\cdot\|_2$ represents L2-norm. Results computed under conformed mesh with 1 million degrees of freedom is taken as reference. MUMPS [3] has been utilized for linear solving with an auto-gauging technique [61]. The simulation is made on a CPU configured with an Intel-i7(6820HQ) processor (4 Cores, RAM = 5 GB). The approaches are developed and tested on a development version of commercial software Altair FluxTM [4].

6.1.3 Intermediate mortar mesh

To select the order of refinement for mortar mesh (Γ_{fm_h}), we compare error in computing magnetic energy around sliding surface (Air-moving region) between mortar mesh scenarios approximately 4 times and 2 times finer than mesh around sliding surface (Γ_{m-fm_h}). The details regarding the mortar mesh are provided in table.6.2. Here total number of face element belonging to surface mesh Γ_{m-fm_h} is equal to Γ_{f-fm_h} .

Table 6.2 – Mortar mesh details.

Mesh Scenario	Face element around sliding surface (Γ_{m-fm_h})	Mesh - A ($4 \times \Gamma_{m-fm_h}$)	Mesh - B ($2 \times \Gamma_{m-fm_h}$)
1	616	2,860	1,508
2	1,118	3,904	1,976
3	1,772	6,808	4,536
4	7,224	29,000	16,254

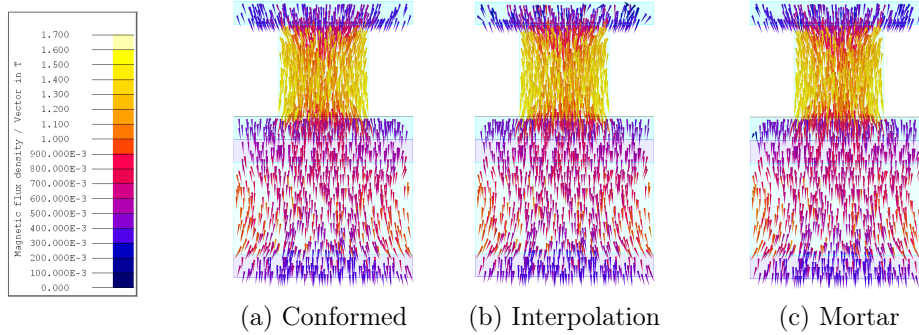
Table 6.3 – Error analysis of magnetic energy computation along sliding surface (Air-moving region).

Mesh Scenario	Mortar Mesh - A ($4 \times \Gamma_{m-fm_h}$)	Mortar Mesh - B ($2 \times \Gamma_{m-fm_h}$)
1	2.177 %	9.623 %
2	1.24 %	10.324 %
3	0.513 %	23.379 %
4	0.435 %	23.874 %

From a comparison provided in the table.6.3 regarding the accuracy of results computed using mortar mesh 4 times and 2 times finer than the mesh around sliding surface (Γ_{m-fm_h}), a constant convergence is observed for mortar mesh - A over mortar mesh - B while moving from mesh scenario 1 to 4. The convergence failure for mortar mesh - B could be due to an inaccurate Gauss quadrature integration while computing coupling matrix D, as the mortar mesh is generated independently, i.e. without performing the mesh-mesh intersection around sliding surface. Therefore, we choose the mortar mesh approximately 4 times finer than mesh belonging to the sliding surface (Γ_{m-fm_h}).

6.2 Validation and results

6.2.1 Isovalues of magnetic flux density


 Figure 6.3 – Representation of flux arrows from cylinder-1 (Moving) to cylinder-2(Static) at $\theta = 5^\circ$

In order to validate the described herein approaches, we tested it on the magneto-static test case see fig.(6.1). Fig.(6.3) shows continuous magnetic flux arrows moving from cylinder-1 (moving) to cylinder-2 (static) through the air gap. No visible difference can be seen between conformed mesh and, non conformed mesh using edge interpolation and mortar method see Figure.6.3.

We also computed the magnetic energy around the sliding interface at different rotor position, as shown in fig.(6.4). One point should be noticed in fig.(6.4), i.e., the energy computations are almost constant at each step of rotation. Since the

6.2. VALIDATION AND RESULTS

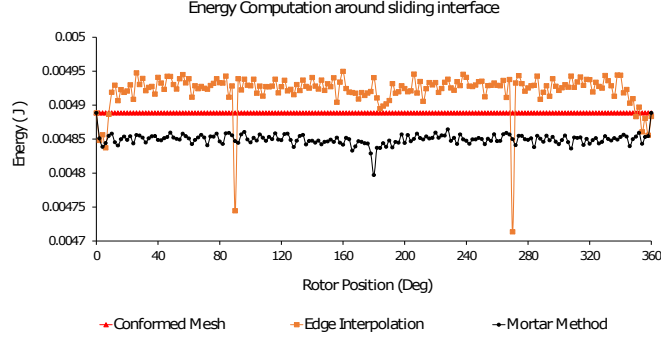


Figure 6.4 – Depiction of energy computed around sliding interface (Air moving) shown in Figure.6.1 at different rotor position.

test case is symmetrical around Z-axis, we have constant value at each step. The average difference in magnetic energy between interpolation and conformed mesh is 0.87% also between mortar and conformed mesh the difference is 0.81%.

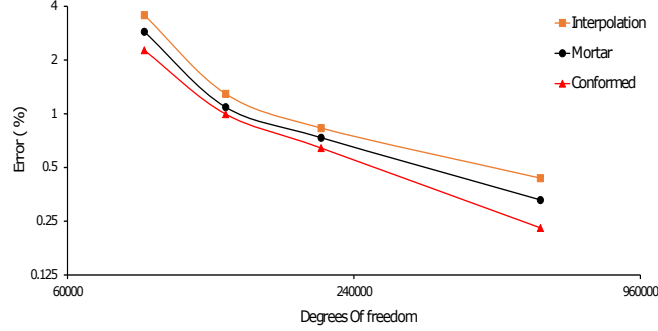


Figure 6.5 – Convergence analysis for the magnetic energy.

6.2.2 Convergence Analysis (Accuracy)

Now that we have validated both approaches here, we will quantify the convergence rate for magnetic energy. We will evaluate error according to (6.1). The reference case for the convergence analysis is the computation of magnetic energy under the conformed mesh for around 1.5 million unknowns.

The evolution of error in magnetic energy computation is depicted on the log-log scale in fig.(6.5). The slope of this represents the convergence rate. Despite the same convergence rate for the mortar method and the edge interpolation, the mortar method accuracy is better than the edge interpolation.

In the next sub-section, we will study the mortar method and the edge interpolation performance; based on computation time and computational memory, tested on different mesh scenarios.

6.2.3 Performance

Table 6.4 – Computation time per step.

Mesh Scenario	Conformed mesh	Edge Interpolation	Mortar Method
1	19 s	19 s	41 s
2	23 s	23 s	57 s
3	40 s	44 s	127 s
4	126 s	141 s	2,862 s

Table 6.5 – Number of non zero terms in matrix.

Mesh Scenario	Conformed mesh	Edge Interpolation	Mortar Method
1	1,713,786	1,745,178	5,280,970
2	2,011,643	2,049,480	6,437,257
3	2,956,097	3,008,769	9,361,955
4	8,357,734	8,582,596	39,003,229

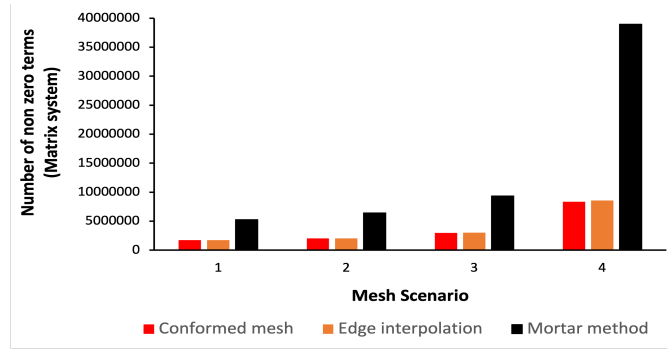


Figure 6.6 – Number of non zero terms in a matrix system at different mesh scenarios.

On analyzing table.6.4, it is shown from the simulation that edge interpolation is twice as fast as mortar method in scenario-1 and this gap is increasing, as difference in computation time almost surge by twenty times in the case of scenario-4. One more important thing should be noticed in table.6.5 and fig.(6.6) that the number of non zero terms in the case of mortar method increases exponentially in contrast to edge interpolation while moving from scenario-1 to scenario-4. The reason behind the increase in the number of non zero terms is the size of mortar mesh. This exponential increase in the number of non zero terms in the case of mortar method also leads to the utilization of a large amount of computational memory.

One can notice edge interpolation is bit less accurate than mortar method but the computation time and computation memory related to edge interpolation is very close to the conformed edge FEM.

6.3 Robustness analysis based on mesh regularity

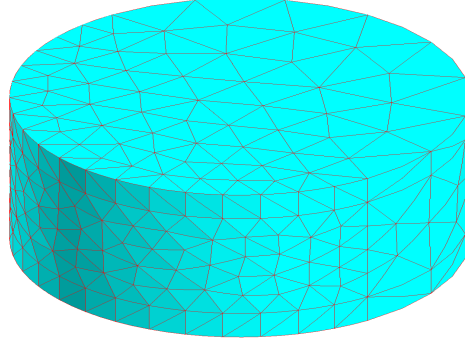


Figure 6.7 – 3D view of surface mesh around sliding surface.

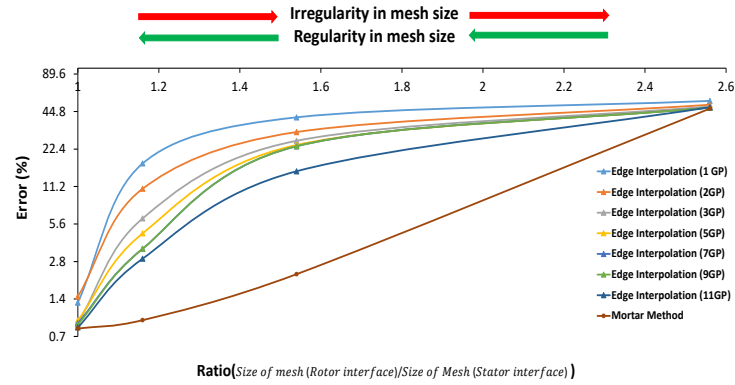


Figure 6.8 – Error computation for the magnetic energy at different scale of mesh regularity around sliding surface.

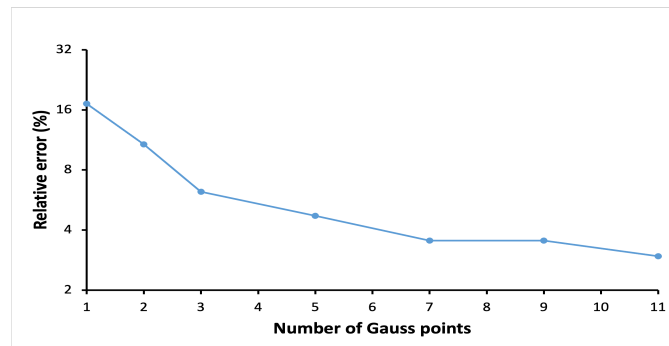


Figure 6.9 – Error computation for the magnetic energy as a function of number of Gauss points (Ratio = 1.16).

To check the proposed methods' robustness, we tested the edge interpolation and the mortar method at a different scale of mesh regularity varying between 2.6 to 1. Here the scale 2.6 and 1 means the ratio of the size of an edge element belonging

to the mesh Γ_{m-fm} to the size of an edge element belonging to mesh Γ_{f-fm} . The quality of mesh regularity is best when the scale is 1 and worst at the scale 2.6.

In fig.(6.7), we represents the mesh along sliding surface for Γ_{m-fm} in such a way that at $\theta = 180^\circ$ of rotation the mesh regularity will be close to 2.6. Using the similar proposition for mesh along sliding surface for Γ_{m-fm} depicted in fig.(6.2a) gives mesh regularity close to 1.

In fig.(6.8), we present the error computation for magnetic energy, using edge interpolation and mortar method. The results computed using edge interpolation without any intermediate mesh is susceptible to mesh regularity. On analysing fig.(6.8) and fig.(6.9) together, we can see a minimum 3 integration points (Gauss points) are needed in the edge interpolation performed over triangle surface elements. The mortar method is less sensitive to mesh regularity on comparing it with edge interpolation.

6.4 Validation and results of source terms computed on reduced domain under the application of movement (Non - Meshed coils)

In the Altair FluxTM, there exist two types of coils: non-meshed coils and meshed coils. The calculation of source in Altair FluxTM is carried out in three forms: source magnetic vector potential \mathbf{A}_s , source magnetic field \mathbf{H}_s and source current density \mathbf{J}_s . For the meshed coil, the source is \mathbf{J}_s , as the coil's geometry corresponds to mesh perfectly. In non-meshed coils, the source is \mathbf{A}_s or \mathbf{H}_s calculated analytically using Biot and Savart law, as the mesh does not corresponds to the geometry of the coil. After analytical calculation, the source is projected as \mathbf{A}_j on the edges of the edge finite element space. For a more detailed review, please refer [25]

This section will validate source term computation on a reduced domain studied under the movement for a non-meshed coil. To validate, we will compare academic test-case results for a non-meshed coil with a meshed coil under the reduced domain. The source computation under the reduced domain for meshed coil has already been validated in the past on Altair FluxTM see [25] and under the application of movement in the previous section. Therefore, we will be using the results of the meshed coil as a reference in our study.

6.4.1 Isovalues of magnetic flux density

As a qualitative comparison the isovalues of the magnetic flux density \mathbf{B} computed using \mathbf{A} formulation are presented in fig.(6.10) and fig.(6.11). In the fig.(6.10) and fig.(6.11), we compared the isovalues computed on cylinder-1 moving and cylinder-2 static at $\theta = 12^\circ$ between meshed coil and non-meshed coil.

The source term for meshed coil under reduced domain is \mathbf{H}_j for detail refer chapter 6 of [25]. The source term for non-meshed coil under reduced domain is \mathbf{A}_j is described in section 2.3. The isovalues of \mathbf{B} calculated for non-meshed coil are respectively identical to isovalues of \mathbf{B} calculated for meshed coil as shown in (6.10) and fig.(6.11).

In the next sub-sections, we will present the results for magnetic energy and magnetic flux computed for the test case shown in fig.(6.1) using a non-meshed coil,

6.4. VALIDATION AND RESULTS OF SOURCE TERMS COMPUTED ON REDUCED DOMAIN UNDER THE APPLICATION OF MOVEMENT (NON - MESHED COILS)

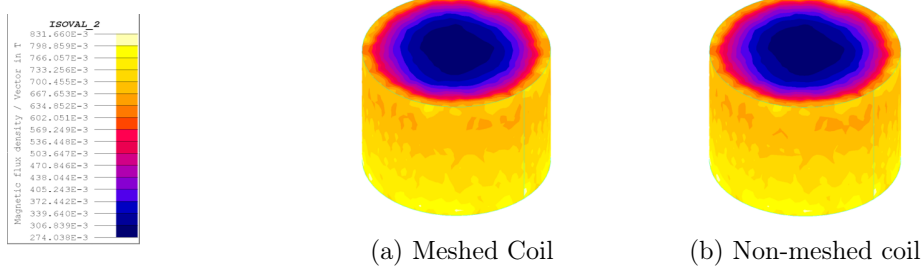


Figure 6.10 – Representation of isovalues of magnetic flux density computed on cylinder-1 (Moving) at $\theta = 12^\circ$

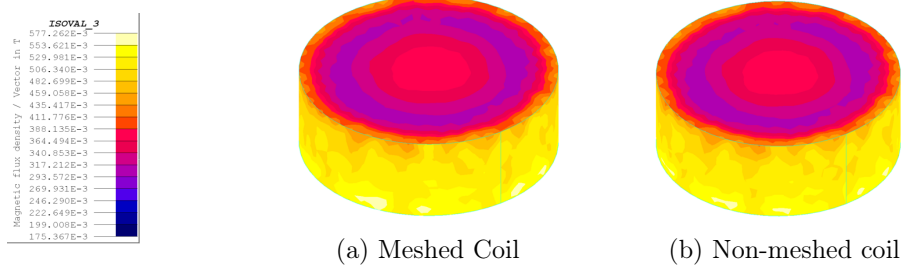


Figure 6.11 – Representation of isovalues of magnetic flux density computed on cylinder-2 (fixed) at $\theta = 12^\circ$

and we will compare the results with the meshed coil.

6.4.2 Magnetic Energy

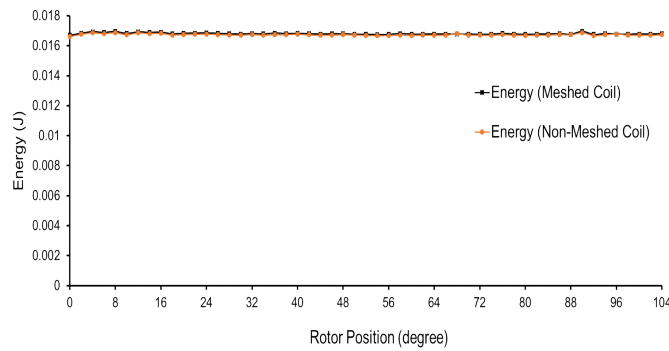


Figure 6.12 – Magnetic energy computed at a different rotor position.

The magnetic energy is computed over the whole domain. In fig.(6.12), we shown the magnetic energy computation at every 2° of rotation from 0° to 104° under magneto-static scenario. As the test case is axis-symmetric around the z-axis and rotation is around the z-axis; therefore, the magnetic energy value is constant for each rotation step. The average difference for magnetic energy between meshed coil and the non-meshed coil is less than 0.4%. Since the mesh around the sliding surface is a bit coarse, small oscillations are observed.

6.4.3 Magnetic Flux

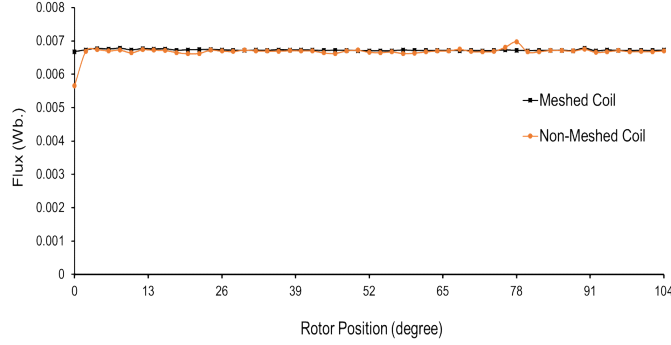


Figure 6.13 – Magnetic flux computed on a coil at a different rotor position.

In this sub-section, we show the magnetic flux computation for coil defined under reduced domain $(\Omega_f \setminus \Gamma_{f-fm})$ in the fig.(6.13). Few spurious oscillations are observed at few positions of computations for non-meshed coils. The average difference for magnetic energy between meshed coil and the non-meshed coil is less than 1%; however, at $\theta = 0^\circ$ and 78° numerical error greater than 10% and 2.5% are observed, respectively.

6.5 Conclusions

This chapter has validated two approaches to model a rotating motion for the magneto-static problem and compared them based on accuracy and performance. From the analysis presented in section 6.2 to 6.4, the following conclusions are drawn:-

- Both the methods yield the same convergence rate for energy computation under regular mesh scenario.
- The accuracy of the mortar method proven to be bit more accurate in contrast to edge interpolation.
- To have a good convergence with the mortar method, the mortar mesh should be at least 4 times finer than the mesh around the sliding surface.
- The mortar method is costlier than edge interpolation in terms of computational time and computational memory.
- The edge interpolation is more sensitive to mesh regularity than the mortar method.
- We also validated the source computation using \mathbf{A}_J source term computed over reduced domain under the application of movement.

In the next chapter, we will test mortar method, the edge interpolation and the source computation over reduced domain for transient and static FEA of TEAM WORKSHOP Problem 24 [2].

Chapter 7

TEAM workshop problem 24

Contents

7.1	Magneto-static problem	77
7.1.1	Test case description	77
7.1.2	Linear problem	77
7.1.3	Non-linear problem	81
7.1.4	Summary	84
7.2	Source term computed on reduced domain for non-meshed coils under magneto-static and magneto transient scenario	84
7.2.1	Magneto-static problem	84
7.2.2	Magneto transient problem	86
7.2.3	Summary	86
7.3	Conclusion	86

7.1 Magneto-static problem

This chapter will study the application of mortar method, and edge interpolation on TEAM Workshop Problem 24 [2]. This chapter aims to test the mortar method and the edge interpolation on a complex test case. By complex test case, we mean the magnetic field behaviour varies as a function of the rotor position.

7.1.1 Test case description

The components of Problem 24 consist of a rotor and a stator with two coil windings on it, as shown in fig.(7.1). The rotor, coil, shaft and air regions are meshed with the tetrahedron elements, and the stator region is meshed with the prismatic elements. During the application of movement, we have a triangle - triangle intersections along the sliding surface. The material property for both rotor and stator is linear isotropic with relative permeability (μ_r) of 500. The total number of turns of coil windings applied to the coil conductor is 350. The source current applied in the coil is 5 A. The simulation is made on a CPU configured with an Intel-i7(6820HQ) processor (4 Cores, RAM = 9 GB).

7.1.2 Linear problem

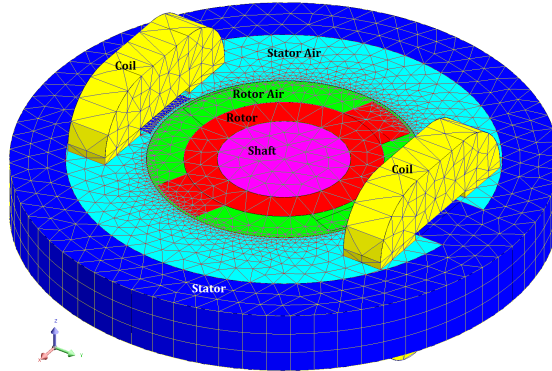


Figure 7.1 – 3D view of test case TEAM workshop Problem-24.

In this sub-section, we will test the methods under the magneto-static scenario. The behaviour of the material used in defining the stator and rotor core is linear. We have tested the problem under three case studies based on the quality of mesh used. In the first case, the total number of unknowns used is closed to 120,000. The size of an edge element along the sliding surface is equal to 6 mm. In the second case, the total number of unknowns increased to 266,632; the size of an element's edge along the sliding surface equal to 1.5 mm. In the third case, the total number of unknowns is around 800,000; the edge element's size along the sliding surface is equal to 1 mm. The mortar method is tested only on case study 1 because the source code for building the mortar method topological matrix is not optimal. In the first section, we test the methods under the magneto-static scenario. After that, we will test the application of edge interpolation for a non-linear problem. In the last section, we will test edge interpolation under the influence of source \mathbf{A}_J computed under the reduced domain for the non-meshed coil.

7.1. MAGNETO-STATIC PROBLEM

Case study - 1 (120,000 unknowns)

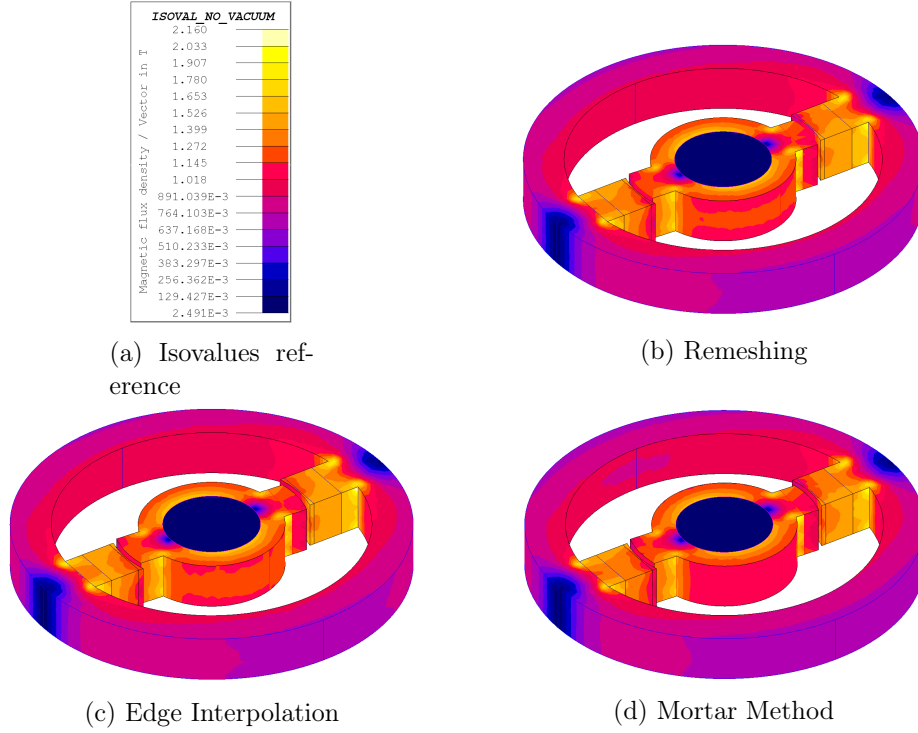


Figure 7.2 – Representation of magnetic flux density isovalue at $\theta = 18^\circ$

Fig.(7.2) shows the magnetic flux density iso-value plots for remeshing, mortar method and edge interpolation computed at 18° of rotation. The isovalues computed using all the three approaches are similar and varying between values 0 to 2.160 T. However, a small variation in the isovalues pattern is observed.

The computation time for edge interpolation is almost 4 times lower than remeshing, as shown in table.7.1. The computation time for the mortar method is 4 times higher than the edge interpolation. This difference in computation times between edge interpolation and mortar method is due to the creation of mortar mesh and computation of D matrix over mortar mesh. The increase in computation time for the mortar method is directly proportional to the mortar mesh size. In this case, mortar mesh is 4 times finer than surface mesh around the interface.

Table 7.1 – Computation time per step (Linear problem).

Solver	Unknowns	Remeshing	Edge Interpolation	Mortar Method
MUMPS	120,000	75 s	19 s	82 s
MUMPS	266,632	96 s	41 s	-
MUMPS	800,000	663 s	206 s	-

Fig.(7.3) depicts torque computation for 90 steps, where shaft and rotor rotate 2° anticlockwise against stator at each step. The simulation is made on a mesh with

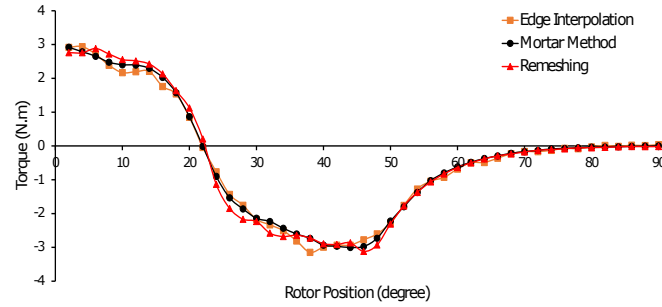


Figure 7.3 – Torque computed at different rotor position for Team workshop problem-24.

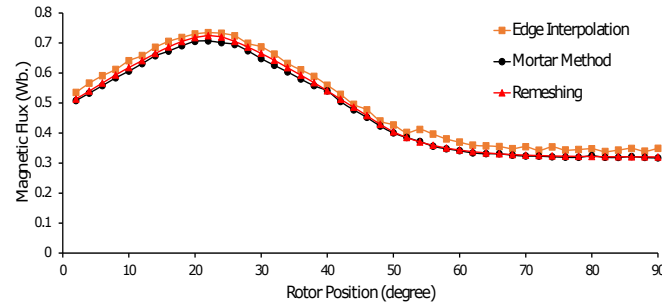


Figure 7.4 – Magnetic flux computed for coil conductor at different rotor position for Team workshop problem-24.

120,000 degrees of freedoms. Since the mesh around the sliding surface is coarse numerical oscillations are observed for all the approaches, including remeshing. The numerical oscillations are low for the mortar method in contrast with the edge interpolation. The next case study shows that these numerical oscillations for edge interpolation decrease with finer mesh around the sliding surface. Like torque, similar observation is made for magnetic flux computation, as shown in fig.(7.4). In the next sub-section, we will present the edge interpolation result when tested for the non-linear problem.

Case study - 2 (266,632 unknowns)

Fig.(7.5) and fig.(7.6) depicts torque and magnetic flux computation for the simulation made on a mesh with 266,632 degree of freedoms. Since the mesh around the sliding surface is finer than case study -1, minimal numerical oscillations are observed for edge interpolation compared to case study - 1. The average variation between remeshing and edge interpolation for torque and magnetic flux computation is less than 2%. The computation time for edge interpolation is almost 2.34 times lower than remeshing, as shown in table.7.1.

7.1. MAGNETO-STATIC PROBLEM

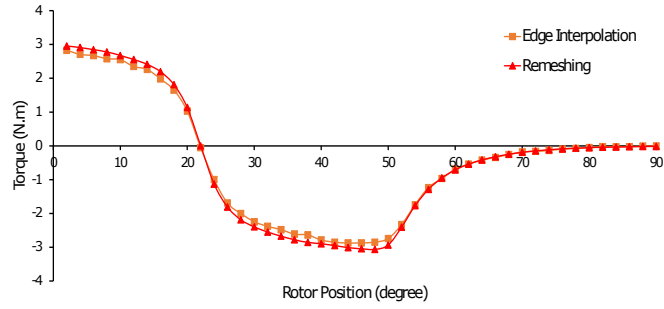


Figure 7.5 – Torque computed at different rotor position for Team workshop problem-24.

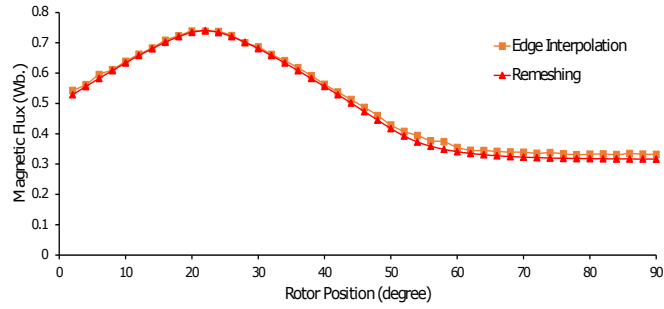


Figure 7.6 – Torque computed at different rotor position for Team workshop problem-24.

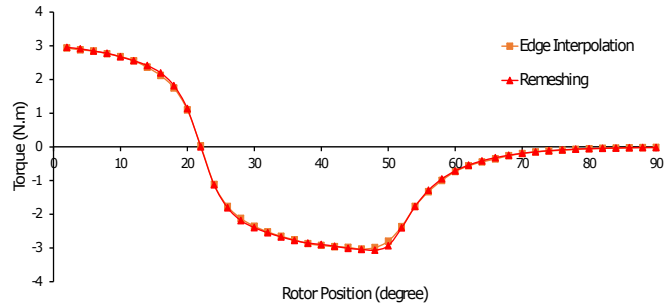


Figure 7.7 – Torque computed at different rotor position for Team workshop problem-24.

Case study - 3 (800,000 unknowns)

Fig.(7.7) and fig.(7.8) depicts torque and magnetic flux computation for the simulation made on a mesh with 800,000 degree of freedoms. Since the mesh around the sliding surface is much finer, the retrieved solutions using edge interpolation have almost converged to retrieved solutions using remeshing. The variation between remeshing and edge interpolation for torque and magnetic flux computation is less than 1%. The computation time for edge interpolation is almost 3.21 times lower

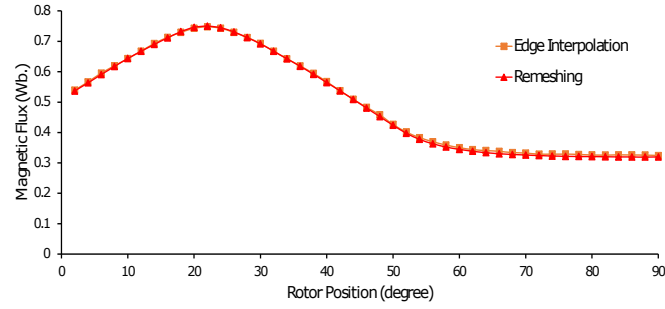


Figure 7.8 – Torque computed at different rotor position for Team workshop problem-24.

than remeshing, as shown in table.7.1.

7.1.3 Non-linear problem

Table 7.2 – Material property (Non-linear problem).

Material	Carbon Steel
Magnetic Property	Initial relative permeability:- 17.037E3
	Mean evaluated permeability:- 6.065E3
	Saturation magnetization Js (T):- 1.99

In this sub-section, the methods are tested under non-linear behaviour material. For the non-linear test, the chosen material possesses the isotropic spline saturation behaviour in terms of magnetic property, as detailed in table.7.2. The simulation takes 2 to 3 non-linear iterations to solve for all the three methods.

Case study - 1 (120,000 unknowns)

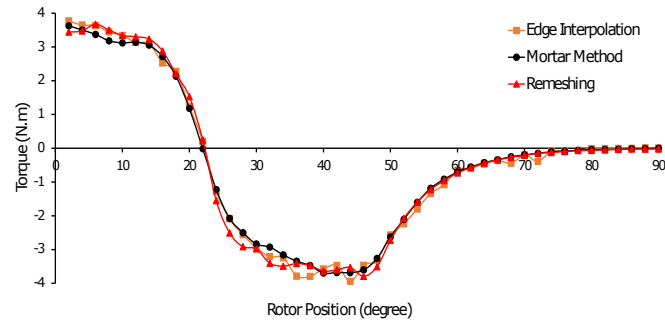


Figure 7.9 – Torque computed at different rotor position on Team workshop problem-24. (Case Study - 1 Non-linear)

7.1. MAGNETO-STATIC PROBLEM

Table 7.3 – Computation time per step (Non-linear problem).

Solver	Unknowns	Remeshing	Edge Interpolation	Mortar method
MUMPS	120,000	83 s	25 s	93 s
MUMPS	266,632	122 s	67 s	-
MUMPS	800,000	831 s	381 s	-

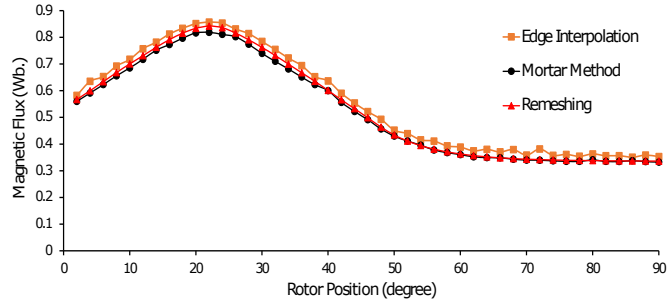


Figure 7.10 – Magnetic flux computed at different rotor position on Team workshop problem-24. (Case Study - 1 Non-linear)

Fig.(7.9) and fig.(7.10) display torque and magnetic flux computations for case study - 1 under non-linear scenario. Similar to the linear test case, we observe numerical oscillations both in torque and flux computations for all the listed methods. Computation time for edge interpolation is around 3 times lower than the mortar method, and remeshing for more detail see table.7.3.

Case study - 2 (266,632 unknowns)

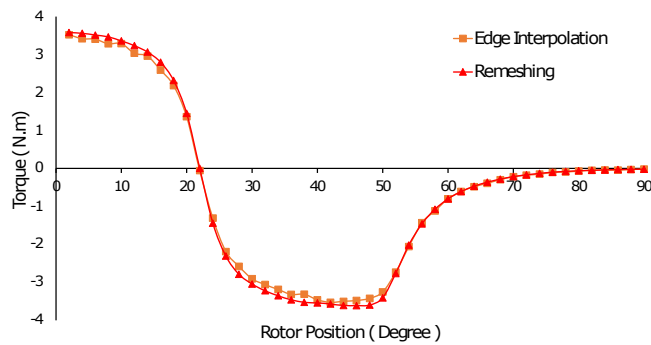


Figure 7.11 – Torque computed at different rotor position on Team workshop problem-24. (Case Study - 2 Non-linear)

Here the edge interpolation is nearly 2 times faster than the remeshing, as detailed in table.7.3. As it was observed in the linear test case (case study - 2), numerical oscillations have been reduced to minimal with the decrease in length of an edge element from 6 mm to 1.5 mm around the sliding surface see fig.(7.20) and fig.(7.12). The average variation between the edge interpolation and the remeshing for torque and magnetic flux computations is below 2%.

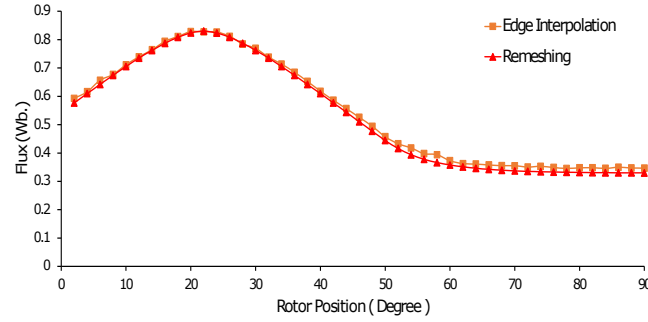


Figure 7.12 – Magnetic flux computed at different rotor position on Team workshop problem-24. (Case Study - 2 Non-linear)

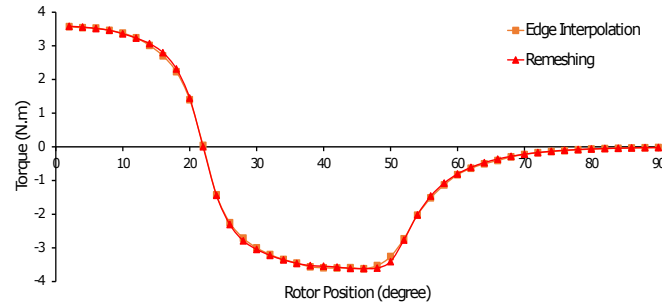


Figure 7.13 – Torque computed at different rotor position on Team workshop problem-24. (Case Study - 3 Non-linear)

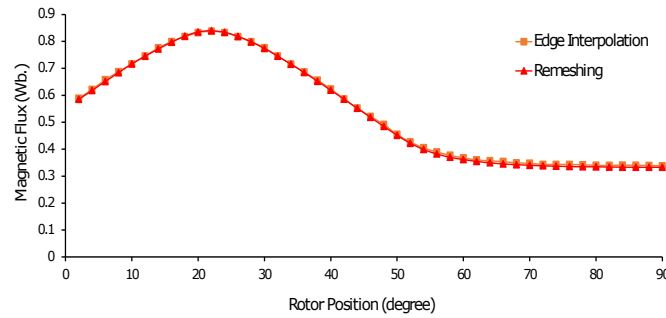


Figure 7.14 – Magnetic flux computed at different rotor position on Team workshop problem-24. (Case Study - 3 Non-linear)

Case study - 3 (800,000 unknowns)

Similar to the retrieved results for torque, and magnetic flux computations under case study - 3 (Linear problem), the average difference between the edge interpolation and the remeshing for torque and magnetic flux computations fall below 1% see fig.(7.13) and fig.(7.14). Again, the edge interpolation is nearly 2 times faster than remeshing.

7.2. SOURCE TERM COMPUTED ON REDUCED DOMAIN FOR NON-MESHED COILS UNDER MAGNETO-STATIC AND MAGNETO TRANSIENT SCENARIO

7.1.4 Summary

This section validated the application of the mortar method and the edge interpolation for TEAM workshop problem 24. Here again, the computation time taken by the edge interpolation is less than the mortar method. Less numerical oscillations are observed in the case of the mortar method on comparing with edge interpolation. We have also shown the application of edge interpolation for non-linear problems. In this section, meshed coils are utilized in the simulations. Similar results are obtained for the magneto transient problem to avoid repetition; results are presented in an upcoming section. In the next section, we will validate the computation of source term \mathbf{A}_J on the reduced domain under the application of movement for non-meshed coils.

7.2 Source term computed on reduced domain for non-meshed coils under magneto-static and magneto transient scenario

Now we are going to validate the computation of source term \mathbf{A}_J on a reduced domain studied in section 2.3 for TEAM workshop problem 24. The source computation under the reduced domain for meshed coil has already been validated on AltairTM. The regions considered under the reduced domain are stator, stator air and coil. We will be using computation results of meshed coils as a reference in our study. The total number of unknowns used in this simulation is around 266,632, and edge interpolation is used to apply the movement. For magneto transient scenario, a constant speed of 2000 rpm is imposed on the rotor and the shaft in the anticlockwise direction; and the initial position of the rotor is 2° .

7.2.1 Magneto-static problem

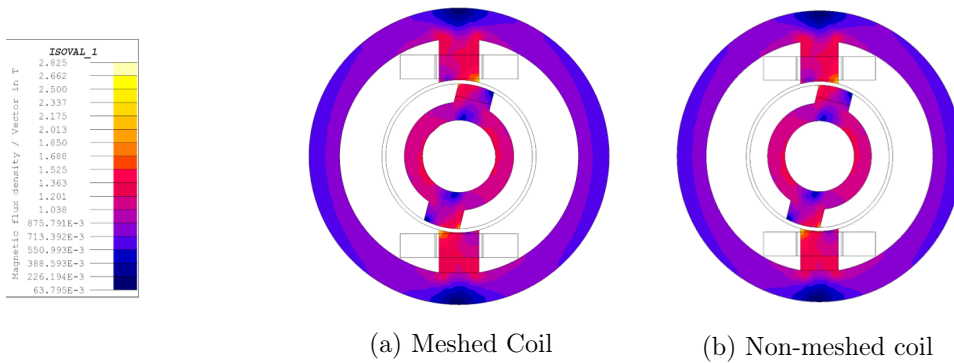


Figure 7.15 – Representation of magnetic flux density isovalue at $\theta = 8^\circ$ under magnetostatic scenario

In fig.(7.15), we present the isovalues of magnetic flux density \mathbf{B} computed using \mathbf{A} formulation. The isovalues pattern are exactly identical between meshed coil and non-meshed coil. In the fig.(7.16) and fig.(7.17), we present the comparison

of torque and magnetic flux computations between meshed and non-meshed coils under magneto-static scenario. The average variation in torque and magnetic flux computation between meshed and non-meshed coils is below 0.4%.

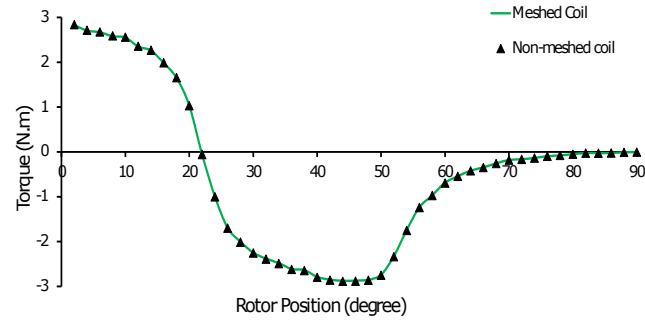


Figure 7.16 – Torque computed at different rotor position on Team workshop problem-24.

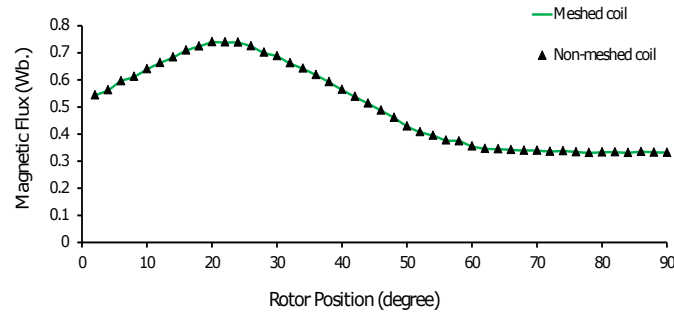


Figure 7.17 – Magnetic flux computed at different rotor position on Team workshop problem-24.

In the next sub-section we will present results retrieve under magneto-transient scenario for TEAM workshop problem 24 using non-meshed coils.

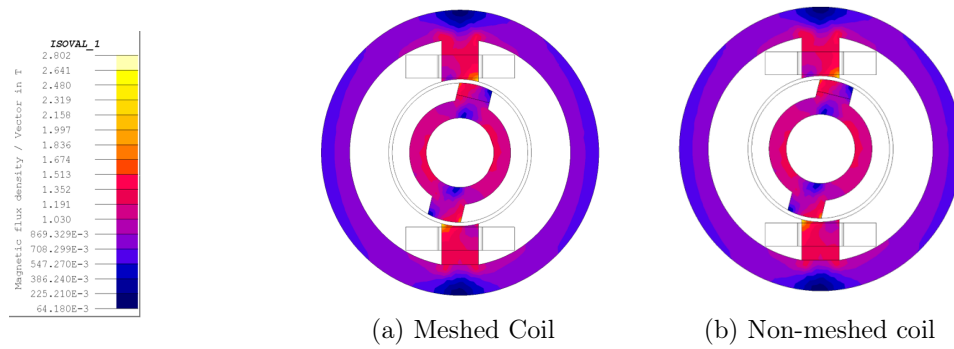


Figure 7.18 – Representation of magnetic flux density isovalue at $\theta = 8^\circ$ under magneto transient scenario

7.2.2 Magneto transient problem

Fig.(7.18) depicts the iso values of magnetic flux density \mathbf{B} computed at a position $\theta = 8^\circ$. No variation is observed in iso values pattern between meshed and non-meshed coils. Fig.(7.19) and fig.(7.20) presents torque and magnetic flux computation under magneto transient scenario. The average variation for torque and magnetic flux between the meshed coil and non-meshed is less than 0.4%.

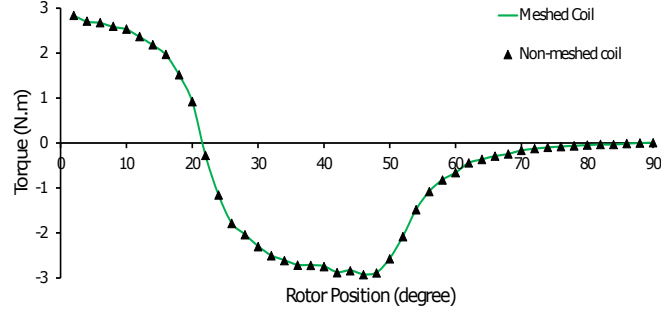


Figure 7.19 – Torque computed at different rotor position on Team workshop problem-24. (Magneto transient scenario)

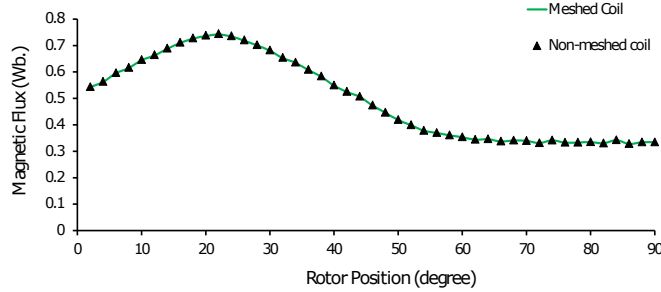


Figure 7.20 – Magnetic flux computed at different rotor position on Team workshop problem-24. (Magneto transient scenario)

7.2.3 Summary

In this section, we have validated the source term \mathbf{A}_J computed on the reduced domain under the application of movement for non-meshed coil conductor. We have tested it under both magneto-static and magneto transient scenarios. The average difference that is noticed between the meshed coil and non-meshed coil computation is around 0.4%. In the next section, we are going to present holistic observations of this chapter.

7.3 Conclusion

In this chapter, we have tested the mortar method and edge interpolation on TEAM Workshop Problem 24. We also tested the computation of source term \mathbf{A}_J on the

reduced domain for non-meshed coil under the application of movement. From the analysis presented in section 7.1 and section 7.2 following conclusion can be drawn:-

- The increase in computation time for the mortar method is proportional to the mortar mesh size.
- The scale of numerical oscillations under coarse mesh is less in the mortar method when comparing it with the edge interpolation.
- Edge interpolation has the capability to solve non-linear problems.
- Accurate results were retrieved when a non-meshed coil conductor was utilized in simulating the movement under magneto-static and magneto transient scenarios.

Now that we have validated and tested the application of the edge interpolation and the mortar method on a test case, where the magnetic field varies as a function of rotor position. The next step is to test the method on an industrial problem like the induction machine. Since the edge interpolation is computationally cheaper than the mortar method, we choose edge interpolation for the industrial problem analysis. In the next chapter, we will test the application of edge interpolation in the induction machine's transient FEA.

Chapter 8

Transient FEA of Induction Machine using Edge Interpolation

Contents

8.1	Description of induction machine	89
8.2	Results	90
8.2.1	Isovalues of magnetic flux density	90
8.2.2	Torque and Magnetic flux	90
8.2.3	Eddy current Losses	92
8.2.4	Computational performance	92
8.3	Conclusion	93

8.1 Description of induction machine

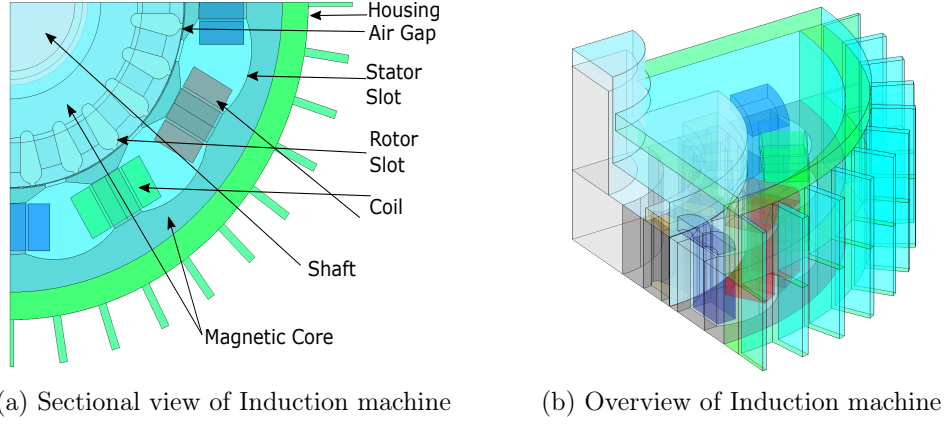


Figure 8.1 – Detail representation of 3-phase rotating Induction machine

Table 8.1 – Geometric parameters of the induction machine under study.

Stator armature	3 slots
Rotor armature	6 slots
Outer diameter	210 mm
Stator magnetic core	135 mm
Inner diameter	134.5 mm
Stator magnetic core	70 mm
Outer diameter	0.25 mm
Rotor magnetic core	
Inner diameter	
Rotor magnetic core	
Air gap thickness	

Table 8.2 – Material property of the induction machine under study.

Shaft	Magnetic property:- 2000 (μ_r) Electrical property:- 0.5E-06 $\Omega.m$ (ρ)
Magnetic Core	Magnetic property:- 5000 (μ_r)
Squirrel cage	Magnetic property:- 1 (μ_r) Electrical property:- 0.156E-07 $\Omega.m$ (ρ)
Housing	Electrical property:- 0.256E-07 $\Omega.m$ (ρ)

In this chapter, we present the magneto transient analysis of the induction machine using edge interpolation. Fig.(8.1a) and fig.(8.1b) presents the cross-sectional view and overview of the induction machine respectively. The main geometric parameters of the induction machine are provided in the table.8.1.

In table.8.2, we present the material properties of different parts of the induction machine. Here the magnetic core has the relative permeability of 5000; housing has the isotropic resistivity of $2.65 \times 10^{-08} \Omega.m$, squirrel cage defined on rotor slot is with the isotropic resistivity of $1.56 \times 10^{-08} \Omega.m$. The shaft has the relative permeability

8.2. RESULTS

of 2000 and isotropic resistivity of $5 \times 10^{-07} \Omega.m$. The speed imposed on the rotor is 1485 rpm. The details regarding the workstation are Intel core i7-6820 HQ CPU @ 2.70GHz, 4 cores. Linear solver utilized is MUMPS (edge interpolation).

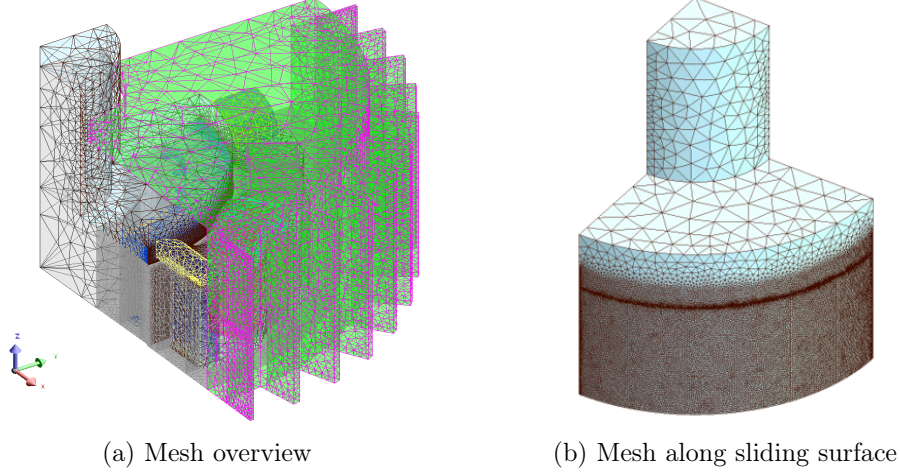


Figure 8.2 – 3D view of mesh utilized to study induction machine.

The induction machine is meshed with tetrahedron elements, as shown in fig.(8.2a). The induction machine has been approximated with about 1.5 million number of unknowns (edge interpolation). The mesh along the sliding surface is kept very fine because of the high concentration of magnetic flux around the sliding surface see fig.(8.2b). **A-V** formulation is used in the case of edge interpolation and in the case of a commercial version of Altair FluxTM **T- ϕ** formulation is used with nodal interpolation. Currently, only T- ϕ formulation can be used for transient FEA of induction on the commercial version of Altair FluxTM. Nevertheless, this formulation requires artificial cuts when the domain is multiply connected. Artificial cuts can be avoided by using **A-V** formulation see [7]. In the next section, we will study the results retrieved using the method edge interpolation and compare it with the commercial version (2020.1) of Altair FluxTM for validation.

8.2 Results

8.2.1 Isovalues of magnetic flux density

In this sub-section, we validate the application of edge interpolation in transient finite element analysis of the induction machine. Fig.(8.3) shows the isovalues of magnetic flux density computed on induction machine at $\theta = 1^\circ$. The results shown in fig.(8.3a) for edge interpolation are quite close to the results shown in fig.(8.3b) for Altair FluxTM. In the next sub-section, we will study the torque computation on the induction machine using edge interpolation.

8.2.2 Torque and Magnetic flux

As no load is applied on the induction machine, net torque for both edge interpolation and Altair FluxTM is zero as shown in fig.(8.4). A small variation in the peak

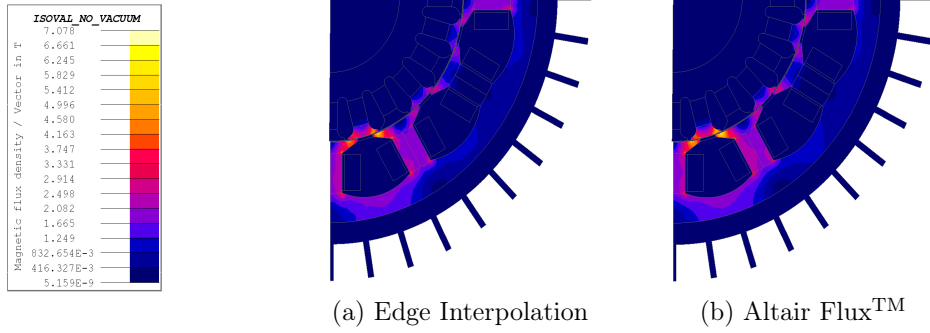


Figure 8.3 – Representation of isovals of magnetic flux density computation at $\theta = 1^\circ$ of rotation.

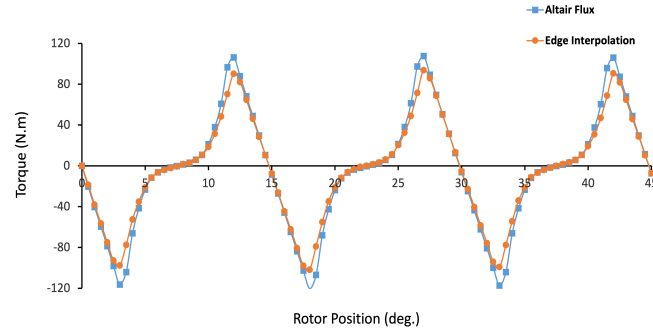


Figure 8.4 – Torque computed using edge interpolation and Altair FluxTM.

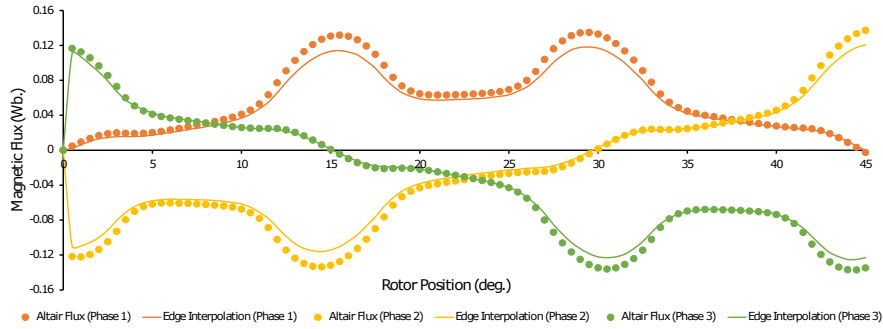


Figure 8.5 – Comparison of magnetic flux computed over coil conductor.

of the torque is observed between edge interpolation and Altair FluxTM is because edge interpolation is computed using \mathbf{A} - \mathbf{V} formulation whereas Altair FluxTM has utilized \mathbf{T} - ϕ formulation. Here, \mathbf{A} - \mathbf{V} formulation has been approximated using first order incomplete edge elements and first order nodal elements, whereas \mathbf{T} - ϕ formulation is approximated using first order complete edge elements and second order nodal elements.

Flux computed by edge interpolation are well closed to that obtain by Altair FluxTM for all the three phases, as shown in fig.(8.5). A small variation in peak values of magnetic flux is observed; this variation arrives because ϕ unknowns are approximated over second order nodal elements, and \mathbf{A} unknowns are approximated

8.2. RESULTS

on a first order incomplete edge elements. In the following sub-section, we will present the results for eddy current losses.

8.2.3 Eddy current Losses

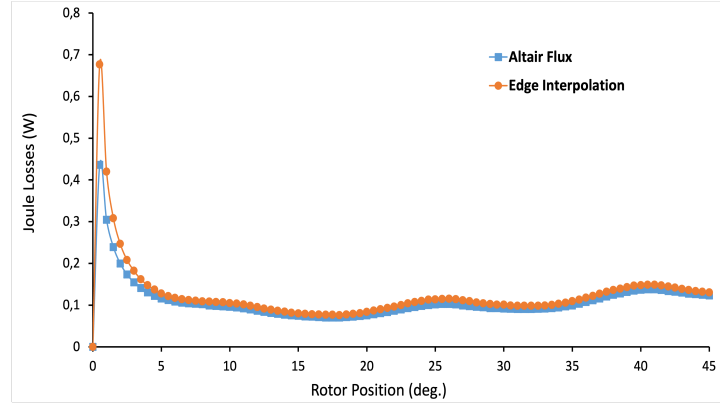


Figure 8.6 – Comparison of eddy current losses in housing.

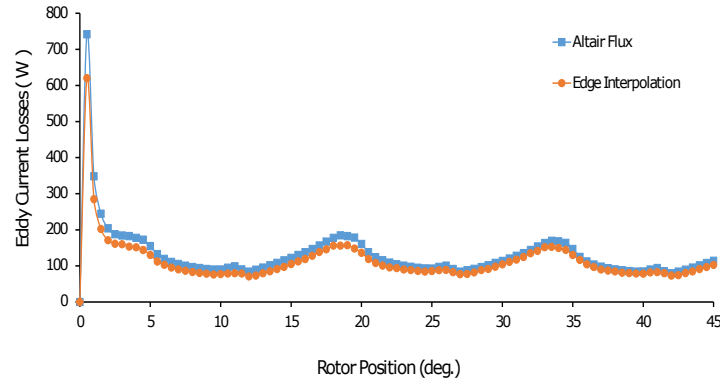


Figure 8.7 – Comparison of eddy current losses in squirrel cage.

The eddy current losses are computed over housing and squirrel cage for edge interpolation and Altair FluxTM are presented in fig.(8.6) and fig.(8.7). The eddy current losses computed are quite diminutive for both the methods as no load is applied over the induction machine.

8.2.4 Computational performance

Table 8.3 – Numerical approximation.

	Formulation	Nodal approx	Edge approx.
Edge Interpolation	A-V	1 st order	1 st order
Altair Flux	T-ϕ	2 nd order	1 st order

Table 8.4 – Computation detail per step.

	Solution memory (per step)	Linear solver	Computation time (per step)
Edge Interpolation	177 MB	MUMPS	240 s
Altair Flux	872 MB	ICCG	420 s

Table.8.3 represents the numerical settings for the edge interpolation and Altair FluxTM. Since nodal unknowns, ϕ is approximated over second order finite element, the numerical memory utilized by Altair FluxTM is higher than edge interpolation as shown in table.8.4. Due to this, the computational time for Altair FluxTM is almost 1.75 times higher than the edge interpolation.

8.3 Conclusion

In this chapter, we have tested the application of edge interpolation in transient finite element analysis of induction machine. After observing the results shown by edge interpolation following conclusion can be drawn:

- The edge interpolation has the ability to accurately solve industrial test cases such as 3D induction machine.
- Small difference in results between edge interpolation and Altair FluxTM are observed. The difference maybe arriving due to difference in the formulation and different order of finite element spaces as discussed earlier.

General Conclusion

The context of the thesis is to numerically model a three dimensional rotating electrical machine, like an induction machine. To optimize the design process of an electrical machine, accurate characterization of eddy current losses in solid conductor region using CAE tool plays an important role. Currently, Altair FluxTM model this problem in three dimension based on magnetic scalar potential and electric vector potential [37]. However, when the domain is multiply connected (geometry with a hole), to enforce continuity equation (Maxwell-Gauss and Maxwell-Thomson equations) over the domain requires artificial mathematical cuts. Algorithm to generate cuts automatically is already implemented in FluxTM [48]. Sometimes, the algorithm fails to generate artificial cuts and these cuts are difficult to implement by the user.

To avoid creating artificial cuts, while modeling a three-dimensional rotating electrical machine, magnetic vector potential \mathbf{A} is approximated on edge finite elements. When the movement is applied on an electrical machine, the two surface meshes between the rotor region and the stator region slides over each other. Therefore, the tangential component of the magnetic field \mathbf{H} and the normal component of the magnetic flux density \mathbf{B} becomes discontinuous around the sliding surface between a rotor region and a stator region. Under nodal finite elements, the continuity is imposed using direct nodal interpolation, which is relatively simple to implement [46]. Under the edge finite elements imposing continuity is a bit complex. Several methods are studied for taking the movement into account under edge elements; remeshing, macro-element, boundary element method, overlapping method, Lagrange multiplier, mortar method, and edge interpolation.

After a detailed bibliographic study, the criteria of choice of methods are: the method has to be generic in three dimensions i.e. independent of step size and mesh type constraint. The method should also deliver accurate results. These criteria made it possible to choose two methods from bibliography, the edge interpolation and the mortar method [53]. Under edge interpolation, we presented the extension of edge interpolation method proposed by [66]. In this thesis, we take into account all the edges belonging to surface elements of stator side intersected by the edge of a surface element belong to rotor side in the calculation of interpolation coefficient.

The mortar method and the edge interpolation shown same rate of convergence on a edge finite element of first order incomplete. However, the accuracy of the mortar method is better than the edge interpolation. In terms of computation time, the edge interpolation performed better than the mortar method, as a third mesh was required in the case of mortar method for the calculation of coupling matrix \mathbf{D} . The accuracy of the edge interpolation (continuous type) is better than the edge interpolation (discontinuous type) on an irregular mesh.

The source of the non-meshed coils are calculated from the source magnetic field

\mathbf{H}_s and source magnetic vector potential \mathbf{A}_j deduced from Biot and Savart law [25]. So to avoid the computation of source at each rotation step they are projected and stored as magnetic vector potential \mathbf{A}_j on the edge element of the mesh. When the movement is applied the quantity $\mathbf{curl} \mathbf{A}_j$ is not continuous around the sliding surface. So to ensure the continuity of $\mathbf{curl} \mathbf{A}_j$ around the interface, the source is computed on a reduced domain (i.e. the region without coil is excluded from source computation). Finally, good results are obtained for a three dimension problem with non-meshed coils under the application of movement. After the detailed observations, we can choose edge interpolation over mortar method for simulating 3D industrial problems.

This thesis's first perspective is to extend the continuous method proposed by [43] on hexahedral elements to tetrahedron elements. The first step is to perform an overlapping of the edge elements around the sliding surface and retrieving the intersection coordinates. However, computing intersecting coordinates on a 3D curved surface would be a challenging task. Once the intersecting coordinates are retrieved, we can calculate the interpolation coefficients. The significant difference in the method presented in this thesis, and the proposed method is the accuracy in calculating the interpolation coefficient, which will be higher in the proposed method. This thesis's second perspective is to extend edge interpolation on first order complete and second order edge elements (tetrahedron meshes). In the last chapter, the difference between the first and second order finite element approximation could be noticed. The second order edge interpolation would make it possible to obtain better results for the problem in \mathbf{A} -V formulation.

The third perspective is to do a detailed analysis on a linear solving of non-linear industrial problems, as bad convergence in linear solving was observed after the first non-linear iteration.

The fourth perspective is to develop other methods for taking movement into account under edge finite elements, such as overlapping method and compare with each other; so as to define the best method for taking movement into account under edge elements.

Bibliography

- [1] Abdel-Razek A, Coulomb J-L, Feliachi M and Sabonnadière J-C. Conception of an air-gap element for the dynamic analysis of the electromagnetic field in electric machines. *IEEE Trans. on Magn.* 1982; 18(2):655-659.
- [2] N. Allen and D. Rodger, "*Description of TEAM Workshop Problem 24: Non-linear Time-Transient Rotational Test Rig*," School of Electrical Engineering, University of Bath, U.K.
- [3] Amestoy P, Buttari A, Guermouche A, L'Excellent J-Y and Ucar B. *Multiforntal Massively Parallel Solver (MUMPS 5.0.0) Users' guide* 2015.
- [4] Altair "Flux," <https://altairhyperworks.com/product/flux>.
- [5] Antunes O J, Bastos J P A, Sadowski N, Razek A, Santandrea L, Bouillault F and Rapetti F. Using hierarchic interpolation with mortar element method for electrical machines analysis. *IEEE Trans. Magn.* 2005; 41(5):1472-1475.
- [6] Atkinson K and Han W. *Sobolev Spaces, Theoretical Numerical Analysis* (2009).
- [7] Biro O, Preis K, Richter K. On the use of the magnetic vector potential in the nodal and edge finite element analysis of 3d magnetostatic problems. *IEEE Trans. Magn.* 1996; 32(3):651-654.
- [8] Boldea I, Tutelea L N, Parsa L and Dorrell D. Automotive electric propulsion systems with reduced or no permanent magnets: an overview, *IEEE Trans. on Industrial Electronics*, vol. 61, no. 10, pp. 5696-5711, Oct 2014.
- [9] Bossavit A. Whitney forms: a class of finite elements for three-dimensional computations in electromagnetism. *IEE Proc.* 1988; 135(8):493-500.
- [10] Bossavit A. *Computational Electromagnetism: Variational Formulations, Complementary, Edge Elements* 1997. Academic Press:Boston.
- [11] Botelho D P, Marechal Y and Ramdane B, "Vector interpolation on natural element method: Mesh sensitivity analysis," 2016 IEEE Conference on Electromagnetic Field Computation (CEFC), Miami, FL, 2016, pp. 1-1, doi: 10.1109/CEFC.2016.7816353.
- [12] Boualem B and Piriou F. Numerical models for rotor cage induction machines using finite element method. *IEEE Trans. Magn.* 1998; 34(5):3202-3205.
- [13] Bouillault F, Ren Z and Razek A. Modélisation tridimensionnelle des courants de foucault à l'aide de méthodes mixtes avec différentes formulations, *Revue de Physique Appliquée* 1990; 25(7):583-592.

- [14] Bouillaud F, Buffa A, Maday Y and Rapetti F. The mortar edge element method in three dimensions : application to magnetostatics. *SIAM Journal on Scientific Computing* 2003; 24(4):1303-1327.
- [15] Boukari N, Lefevre Y and Spiteri P. Modeling the movement of electrostatic motors in a 3d finite element code. *IEEE Trans. Magn.* 2000; 36(4):722-727.
- [16] Buffa A, Maday Y and Rapetti F. Calculation of eddy currents in moving structures by a sliding mesh finite element method. *IEEE Trans. Magn.* 2000 36(4):1356-1359.
- [17] Buffa A, Maday Y and Rapetti F. A sliding mesh-mortar method for a two dimensional eddy currents model of electric engines. *Mathematical Modelling and Numerical Analysis* 2001; 35(2):191-228.
- [18] Chan C, Bouscayrol A, and Chen K. Electric, hybrid, and fuel-cell vehicles: architectures and modeling. *IEEE Trans. Vehicular Technology*, vol. 59, no. 2, pp. 589-598, Feb 2010.
- [19] Davat B, Ren Z and Lajoie-Mazenc M. The movement in field modeling. *IEEE Trans. on Magn.* 1985; 21(6):2296-2298.
- [20] Dreher T, Perrin-Bit R, Meunier G and Coulomb J-L. A three dimensional finite element modelling of rotating machines involving movement and external circuit. *IEEE Trans. Magn.* 1996; 32(3):1070-1073.
- [21] Dular P, Hody J.Y, Nicolet A, Genon A and Legros, W. Mixed finite elements associated with a collection of tetrahedra, hexaedra and prisms. *IEEE Trans. Magn.* 1994; 30(5).
- [22] Ehsani M, Rahman K and Toliyat H. Propulsion system design of electric and hybrid vehicles, *IEEE Trans. Industrial Electronics*, vol. 44, no. 1, pp. 19-27, Feb 1997.
- [23] Emson C, Riley C, Walsh D, Ueda K and Kumano T. Modelling eddy currents induced by rotating systems. *IEEE Trans. Magn.* 1998; 34(5):2593-2596.
- [24] Feliachi M, Coulomb J-L and Mansir H. Second order airgap element for the dynamic finite-element analysis of the electromagnetic field in electric machines. *IEEE Trans. on Magn.* 1983; 19(6):2300-2303.
- [25] Ferrouillat P. Développement de formulations éléments finis 3D en potentiel vector magnétique : application aux machines asynchrones en mouvement. *Energie électrique. Université Grenoble Alpes* 2015; Français.
- [26] Golovanov C, Coulomb J-L, Maréchal Y and Meunier G. 3D mesh connection techniques applied to movement simulation. *IEEE Trans. Magn.* 1998; 34(5):3359-3362.
- [27] Illoul L, Le-Menach Y, Clénet S, Chinesta F. A mixed finite element/meshless natural element method for simulating rotative electromagnetic machines. *European Physical Journal: Applied Physics, EDP Sciences* 2008; 43:197-208.

BIBLIOGRAPHY

- [28] Jianming J. *The Finite Element Method in Electromagnetics* 2014. Wiley-IEEE Press.
- [29] Kometani H, Sakabe S, Kameari A. 3-D Analysis of Induction Motor with Skewed Slots Using Regular Coupling Mesh. *IEEE Trans. Magn.* 2000; 36(4):1769-1773.
- [30] Krebs G, Clénet S, Abakar A, Locment F and Piriou F. Method to connect nonconforming mesh in 3-d with the overlapping method. *IEEE Trans. Magn.* 2009; 45(3):1420-1423.
- [31] Krebs G, Clénet S and Tsukerman I A. Overlapping finite elements for arbitrary surfaces in 3-d, *IEEE Trans. Magn.* 2010;46(8):3473-3476.
- [32] Krebs G, Henneron T, Clénet S and Le Bihan Y. Overlapping finite elements used to connect non-conforming meshes in 3-d with a vector potential formulation. *IEEE Trans. Magn.* 2011; 47(5):1218-1221.
- [33] Kurz S, Fetzer J, Lehner G and Rucker W M. A novel formulation for 3d eddy current problems with moving bodies using a lagrangian description and bem-fem coupling. *IEEE Trans. on Magn.* 1998; 34(5):3068-3073.
- [34] Lai H, Rodger D and Leonard P. Coupling meshes in 3d problems involving movements. *IEEE Trans. Magn.* 1992; 28(2):1732-1734.
- [35] Lee K-S, DeBortoli M J, Lee M J and Salon S J. Coupling finite elements and analytical solution in the airgap of electric machines. *IEEE Trans. on Magn.* 1991; 27(5):3955-3957.
- [36] Lepaul S and Sykulski J K. Coupling of motion and circuits with electromagnetics analysis, *IEEE Trans. Magn.* 1999; 35(3):1602-1605.
- [37] Le Floch Y. Développement de formulations 3D éléments finis T pour la prise en compte de conducteurs massifs et bobinés avec un couplage circuit. *Institut National Polytechnique de Grenoble - Ecole Doctorale Electrotechnique Automatique Télécommunications Signal* 2002; Français.
- [38] Maréchal Y, Meunier G, Coulomb J-L and Magnin H. A general purpose tool for restoring inter-element continuity. *IEEE Trans. Magn.* 1992; 28(2):1728-1731.
- [39] Maréchal Y. Modélisation des phénomènes magnétostatiques avec terme de transport. Application aux ralentisseurs électromagnétiques. *Institut National Polytechnique de Grenoble* 1991; Française.
- [40] Meunier G. *The finite element method for electromagnetic modeling* 2008. ISTE Ltd.
- [41] Meunier G, Coulomb J-L, Salon S and Kräenbühl L. Hybrid finite element boundary element solutions for three dimensional scalar potential problems, *IEEE Trans. on Magn.* 1986; 22(5):1040-1042.

-
- [42] K. Muramatsu, C. Tsukishima, T. Matsuda, T. Nakagawa, T. Takeuchi, "Method for Analyzing 3-D Magnetic Field in Linear Actuator Using Nonconforming Mesh With Edge Elements," *IEEE Trans. Magn.*, vol. 41, no. 5, pp. 1988-1991, May 2005.
 - [43] Muramatsu K, Yokoyama Y, Takahashi N. 3-D magnetic field analysis using nonconforming mesh with edge elements. *IEEE Trans. Magn.* 2002; 38(2):433-436.
 - [44] Nedelec J.C. Mixed finite elements in R^3 . *Numer. Math.* 1980; 35: 315-341.
 - [45] Okamoto Y, Himeno R, Ushida K, Ahagon A, Fujiwara K. A Dielectric Heating Analysis Method With Accurate Rotational Motion of Stirrer Fan Using Nonconforming Mesh Connection. *IEEE Trans. Magn.* 2008; 44(6):806-809.
 - [46] Perrin-Bit R and Coulomb J-L. A three dimensional finite element mesh connection for problems involving movement. *IEEE Trans. Magn.* 1995; 31(3):1920-1923.
 - [47] Phung A. T. Développement de formulations électromagnétiques éléments finis 3D pour la modélisation des dispositifs en fréquence élevée. *Institut National Polytechnique de Grenoble* 2006; Français.
 - [48] A.T. Phung , O. Chadebec, P. Labie, Y.L. Floch, "Automatic Cuts for Magnetic Scalar Potential Formulations," *IEEE Trans. Magn.*, vol. 41, no. 5, pp. 1668-1671, May 2005.
 - [49] Preston, T W, Reece A B J and Sangha P S. Induction motor analysis by time-stepping techniques. *IEEE Trans. Magn.* 1988; 24(1):471-474.
 - [50] Rapetti F, Santandrea L, Bouillault F and Razek A. Calculation of eddy currents in moving structures using a finite element method on nonmatching grids. *International Journal for Computation and Mathematics in Electrical and Electronic Engineering* 2000; 19(1):10-29.
 - [51] Rapetti F. The mortar edge element method on non-matching grids for eddy current calculations in moving structures. *International Journal of Numerical Modelling : Electronic Networks, Devices and Fields* 2001; 14(6):457-477.
 - [52] Rapetti F, Bouillault F, Santandrea L, Buffa A, Maday Y and Razek A. Calculation of eddy currents with edge elements on non-matching grids in moving structures. *IEEE Trans. Magn.* 2000; 36(4):1351-1355.
 - [53] Rapetti F, Maday Y, Bouillault F and Razek A. Eddycurrent calculations in three-dimensional moving structures. *IEEE Trans. Magn.* 2002; 38(2):613-616.
 - [54] Ratnajeevan S and Hoole H. Rotor motion in the dynamic finite element analysis of rotating electrical machinery. *IEEE Trans. on Magn.* 1985; 21(6):2292-2295.
 - [55] Rodger D, Lai H and Leonard P. Coupled elements for problems involving movement. *IEEE Trans. Magn.* 1990; 26(2):548-550.

BIBLIOGRAPHY

- [56] Roppert K, Schoder S, Toth F, Kaltenbacher M. Non-conforming Finite Elements. *International Compumag Society Newsletter - Technical Article* 2018; 25(3):1026-0854.
- [57] Sadowski N, Lefèvre Y, Lajoie-Mazenc M and Cros J. Finite element torque calculation in electrical machines while considering the movement. *IEEE Trans. on Magn.* 1992; 28(2):1410-1413.
- [58] Salon S J, Schneider J M. A Finite Element Boundary Integral Formulation of Poisson's Equation, *IEEE Trans. on Magn.*; 17(6):2574-2576.
- [59] Salon S J, The Hybrid Finite Element Boundary Element Method in Electromagnetics, *IEEE Trans. on Magn.* 1985; 21(5):1829-1834.
- [60] Shi X, Le Menach Y, Ducreux J P and Piriou F. Comparison between the mortar element method and the polynomial interpolation method to model movement in the finite element method. *IEEE Trans. Magn.* 2008; 44(6):1314-1317.
- [61] Tang Z, Zhao Y, Ren Z. Auto-Gauging of Vector Potential by Parallel Sparse Direct Solvers-Numerical Observations. *IEEE Trans. Magn.* 2019; 55(6).
- [62] Tsukerman I A. Overlapping finite element elements for problems with movement, *IEEE Trans. Magn.* 1992; 28(5):2247-2249.
- [63] Vassallo C. *Electromagnétisme classique dans la matière* 1980. Dunod, Paris.
- [64] Yvonnet J, Ryckelynck D, Lorong P, Chinesta F. *Int. J. Numer. Meth. Eng.* 2004; 60:1451.
- [65] Yvonnet J, Chinesta F, Lorong P, Ryckelynck D. *Int. J. Numer. Meth. Eng.* 2005; 44:559. (2005).
- [66] Zhao Y, Xiao X, Xu W. Accelerating the Optimal Shape Design of Linear Machines by Transient Simulation Using Mesh Deformation and Mesh Connection Techniques. *IEEE Trans. Ind. Electron.* 2018; 65(12):9825-9833.

Appendix A

Definitions

This chapter covers some important definitions utilized in the source computation with non-meshed coils. For more detailed study of these definitions, please see [25]

A.1 Inner product form

$$(\mathbf{u}, \mathbf{v})_{\mathbf{L}^2(\Omega)} = \int_{\Omega} \mathbf{u} \cdot \mathbf{v} d\Omega, \quad \forall \mathbf{u}, \mathbf{v} \in \mathbf{L}^2(\Omega), \quad (\text{A.1})$$

$$(\mathbf{u}, \mathbf{v})_{\mathbf{H}(\text{curl}, \Omega)} = (\mathbf{u}, \mathbf{v})_{\mathbf{L}^2(\Omega)} + (\text{curl } \mathbf{u}, \text{curl } \mathbf{v})_{\mathbf{L}^2(\Omega)}, \quad \forall \mathbf{u}, \mathbf{v} \in \mathbf{H}^1(\Omega). \quad (\text{A.2})$$

A.2 Norm of $\mathbf{L}^2(\Omega)$ and $\mathbf{H}(\text{curl}, \Omega)$

$$\|\mathbf{u}\|_{\mathbf{L}^2(\Omega)} = \sqrt{(\mathbf{u}, \mathbf{u})_{\mathbf{L}^2(\Omega)}}, \quad \forall \mathbf{u} \in \mathbf{L}^2(\Omega), \quad (\text{A.3})$$

$$\|\mathbf{u}\|_{\mathbf{H}(\text{curl}, \Omega)} = \sqrt{\|\mathbf{u}\|_{\mathbf{L}^2(\Omega)}^2 + \|\text{curl } \mathbf{u}\|_{\mathbf{L}^2(\Omega)}^2}, \quad \forall \mathbf{u} \in \mathbf{H}^1(\Omega). \quad (\text{A.4})$$

A.3 \mathbf{H}_j be the $\mathbf{L}^2(\Omega)$ projection of \mathbf{H}_s

Let $\mathbf{H}_j \in \mathbf{E}_u^1(\Omega)$ defined on the edges of finite element mesh (Ω_h) . Such that $\mathbf{L}^2(\Omega)$ projection of \mathbf{H}_s gives:

$$\mathbf{H}_j = \frac{1}{2} \arg \min \|\mathbf{X} - \mathbf{H}_s\|_{\mathbf{L}^2(\Omega)}^2 \quad \forall \mathbf{X} \in \mathbf{L}^2(\Omega) \quad (\text{A.5})$$

A.4 \mathbf{A}_j be the $\mathbf{H}(\text{curl}, \Omega)$ projection of \mathbf{H}_s

Let $\mathbf{A}_j \in \mathbf{E}_u^1(\Omega)$ defined on the edges of finite element mesh (Ω_h) . Such that $\mathbf{H}(\text{curl}, \Omega)$ projection of \mathbf{H}_s gives:

$$\mathbf{A}_j = \frac{1}{2} \arg \min \|\mathbf{X} - \mathbf{A}_s\|_{\mathbf{H}(\text{curl}, \Omega)}^2 \quad \forall \mathbf{X} \in \mathbf{H}(\text{curl}, \Omega) \quad (\text{A.6})$$

$$= \frac{1}{2} \arg \min \|\text{curl } \mathbf{X} - \mu_0 \mathbf{H}_s\|_{\mathbf{L}^2(\Omega)}^2 \quad \forall \mathbf{X} \in \mathbf{H}(\text{curl}, \Omega) \quad (\text{A.7})$$

For more detailed study, concerning the implementation of pre-computation using edge finite element approximation see [25].

Appendix B

A- ϕ nodal interpolation

B.1 A- ϕ formulation

The coupling of \mathbf{A} and ϕ formulations approximates \mathbf{H} using \mathbf{A} in regions with coils and ferromagnetic materials, reduced scalar potential ϕ in the air around sliding interface respectively refer fig.(B.1). It gives freedom to utilize the well-known nodal interpolation for ensuring continuity of potentials at the interface instead of edge-based interpolation. The ϕ formulation is expressed as:

$$\mathbf{H} = \mathbf{H}_s - \nabla\phi. \quad (\text{B.1})$$

Here \mathbf{H}_s is the magnetic source field defined as

$$\mathbf{curl} \mathbf{H}_s = \mathbf{J}_s \text{ with } \mathbf{H}_s \times \mathbf{n} = 0 \text{ on } \Gamma_H. \quad (\text{B.2})$$

The conditions on the interface $\Gamma_{\mathbf{A}\phi}$ of the \mathbf{A} and ϕ formulations coupling are expressed as:

$$\mu_{\mathbf{A}}^{-1}(\mathbf{curl}\mathbf{A}) \times \mathbf{n}_{\mathbf{A}} + (\mathbf{H}_s - \nabla\phi) \times \mathbf{n}_{\phi} = 0 \text{ on } \Gamma_{\mathbf{A}\phi}, \quad (\text{B.3})$$

$$(\mathbf{curl}\mathbf{A}) \cdot \mathbf{n}_{\mathbf{A}} + \mu_{\phi}(\mathbf{H}_s - \nabla\phi) \cdot \mathbf{n}_{\phi} = 0 \text{ on } \Gamma_{\mathbf{A}\phi}. \quad (\text{B.4})$$

where $\mu_{\mathbf{A}}$ and μ_{ϕ} are the relative permeability of ferromagnetic material and air respectively. $\mathbf{n}_{\mathbf{A}}$ and \mathbf{n}_{ϕ} are the normal outward for the regions \mathbf{A} and ϕ respectively at the interface.

B.2 Results

B.2.1 Sensor

To analyse the A- ϕ nodal interpolation a simple three dimensional (3D) test case a sensor is chosen. The components of sensor consist of wheel (rotor) with steel as a constituent material and permanent magnets (stator) with coil winding on it.

Magnetostatic (multistatic case) computation has been made for 30 steps, where wheel rotates 1° away from magnet at each step. In order to validate the computation made using A- ϕ nodal interpolation and edge mortar, magnetic torque on the wheel have been computed and a comparison is carried out with remeshing technique as shown in fig.(B.2).

The comparison on the basis of computation time at each step has been made between techniques such as nodal interpolation, edge mortar and remeshing, as shown in table.B.1.

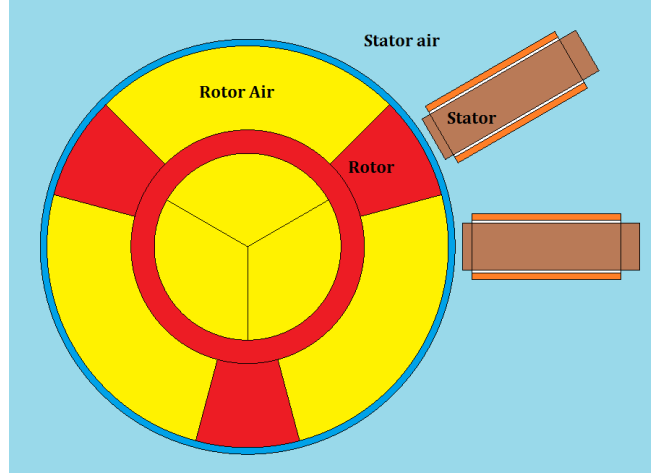


Figure B.1 – Top view representation of test case sensor.

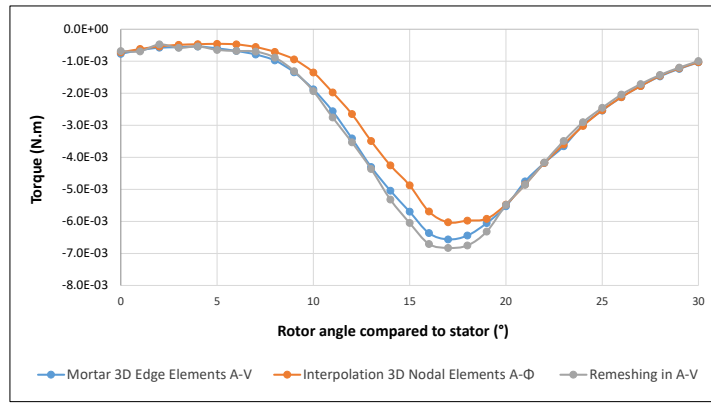


Figure B.2 – Torque computed on the wheel of sensor using different approaches

	Nodal Interpolation	Edge Mortar	Remeshing
Number of Nodes	1,096,849	1,096,849	1,205,689
Number of non zero terms	11,927,418	15,517,191	16,094,458
Total Computation time per step (s)	115	840	366
Solver	MUMPS(Cores = 1)	ICCG	ICCG

Table B.1 – Computation Performance of different Approaches

The total computation time for edge mortar is 7.3 times higher than nodal interpolation and almost 2.5 times higher than remeshing because of exponential increase in the number of state variables \mathbf{A} at interface due to fine Mortar mesh. Torque computation on the wheel for edge mortar is in quite good agreement with remeshing as compared to \mathbf{A} - ϕ nodal interpolation. As torque is sensitive towards mesh around corner of a rotor, a large variation in torque is observed from rotor angle 11° to 19° in \mathbf{A} - ϕ nodal interpolation on comparing with remeshing.

B.2. RESULTS

B.2.2 TEAM workshop problem 24 (Non linear problem)

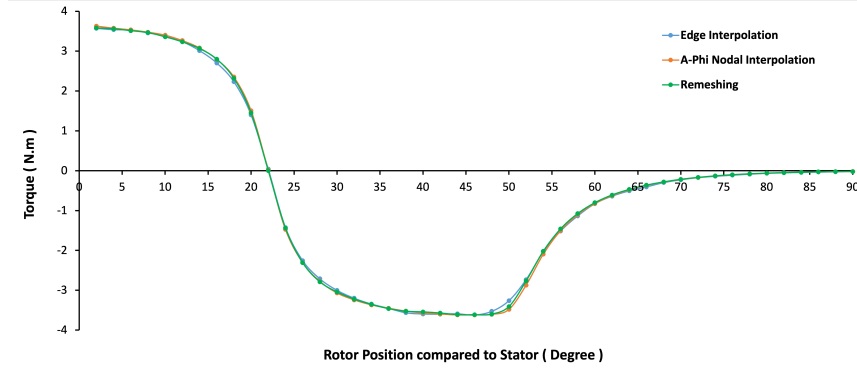


Figure B.3 – Torque computed on the rotor

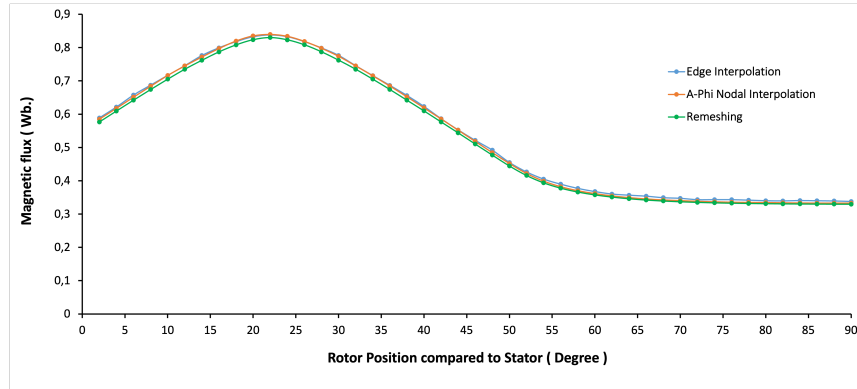


Figure B.4 – Magnetic flux computed on the coil

The torque and magnetic flux computations for the $\mathbf{A}\text{-}\phi$ nodal interpolation is in quite good agreement with remeshing and edge interpolation, as shown in fig.(B.3) and fig.(B.4).

Résumé

Une machine électrique est divisée en deux domaines: le stator (partie fixe) et le rotor (partie mobile) séparés par un mince entrefer. Cet entrefer prend également en compte le transfert de flux entre les deux régions. L'application du mouvement conduit aux maillages glissants non conformes autour de l'interface. Ainsi, assurer la continuité des composants de champ magnétique tangentiel et normal et de densité de flux magnétique est essentiel à l'interface (région de glissement).

Dans le logiciel Altair FluxTM, des formulations basées sur le potentiel scalaire magnétique ont été développées avec la méthode des éléments finis nodaux et sont utilisées avec succès depuis de nombreuses années pour modéliser des machines électriques tournantes 3D. Un inconvénient important de cette méthode est la nécessité de gérer les problèmes de connectivité multiple induits par le potentiel scalaire magnétique. Une solution consiste à introduire des coupes artificielles, ce qui est difficile à mettre en œuvre par l'utilisateur.

Afin d'éviter d'introduire des coupures artificielles dans le domaine étudié, des formulations en potentiel vecteur magnétique sont utilisées. Les enjeux techniques et scientifiques de cette thèse sont de développer et de comparer les méthodes de prise en compte du mouvement, en particulier, la méthode des éléments avec joints et l'interpolation d'arête dans le cadre d'une formulation éléments finis d'arêtes basée sur le potentiel vecteur magnétique.

Mots clés: Méthode des éléments finis d'arête (Edge FEM), Machine électrique, Interpolation d'arête, Méthode des éléments avec joints, Mouvement de rotation.

Abstract

An electrical machine is divided into two domains: the stator (S) (fixed part) and rotor (R) (mobile part) separated by a thin air-gap. This air-gap also takes into account the transfer of flux between two regions. Application of movement leads to the nonconforming sliding meshes around the interface. Thus, ensuring the continuity of tangential and normal magnetic field (**H**) and magnetic flux density (**B**) components are essential at the interface (sliding region).

In the Altair FluxTM software, formulations based on the magnetic scalar potential have been developed with the nodal finite element method and have been used successfully for many years to model 3D rotating electrical machines. A significant disadvantage of this method is the need to manage the multiply connectivity problems induced by the magnetic scalar potential. One solution is to introduce artificial cuts in the mesh, which is difficult to implement by the user.

In order to avoid introducing artificial cuts in the studied domain, magnetic vector potential formulations are used. This thesis's technical and scientific challenges are to develop and compare the mortar method and edge interpolation to take movement into account.

Keywords: Edge finite-element method (Edge FEM), Electrical machine, Edge interpolation, Mortar method, Rotation movement.